Neutron Studies of Multi-Component Polymer Thin Films:

Stratification and Interfacial Structure

A Dissertation Presented for the

Doctor of Philosophy

Degree

The University of Tennessee, Knoxville

Samantha Jae Rinehart

May 2019

Copyright © 2019 by Samantha J. Rinehart

All rights reserved.

DEDICATION

This work is dedicated to my family: my mother, Nancy; my father, Brian; my stepmother, Carrie; and my brother, Alex. Without their endless love, unwavering support, and guidance throughout my life journey and more specifically, my academic career, I would not have maintained the courage and confidence to complete my Ph.D.

ACKNOWLEDGEMENTS

"O Lord my God, When I in awesome wonder,
Consider all the worlds Thy Hands have made"
-"How Great Thou Art," Carl Boberg, 1885

First and foremost, I want to give thanks to God for providing me with the strength, opportunity, and knowledge to complete this research and dissertation. I have been blessed with a supportive arena filled with family, friends, and mentors that have provided encouragement and guidance during the completion of my Ph.D. and if not listed here, I value their contributions in my heart. I am specifically thankful for Dr. Mark Dadmun for his continued mentorship and for providing the opportunities to engage in many intellectually challenging projects. I extend thanks to my committee members, Dr. Alexei Sokolov, Dr. Mike Sepaniak, and Dr. Joshua Sangoro for their time and commitment to my scientific career. I am grateful to my research group colleagues and more specifically, Dr. Brian Morgan, Dr. Halie Martin, and Neiko Levenhagen for scientifically challenging my results and conclusions. The numerous on- and off-campus therapy sessions with Dr. Halie Martin were essential in my personal growth and focusing my efforts towards the completion of this research. I am grateful for Jordan Kaiser's friendship that facilitated the decision to pursue the University of Tennessee for graduate school and the prolonged dinners that provided me with the perseverance to complete my dissertation. Finally, I am particularly appreciative of two influential mentors in my life who have remained supportive beyond my time at Lewis University: Dr. Jason Keleher and Dr. Chuck Crowder.

ABSTRACT

This dissertation presents the impact fabrication conditions have upon layer composition, purity, and interfacial clarity of multi-component thin films on both rigid and flexible substrates. The performance of the multi-functional thin films is directly linked to the macroscopic assembly in a thin film. Prior to production of a novel thin film systems, the suitable fabrication methods required for optimum performance must be determined. Oftentimes, this is pursued on a tedious trial and error basis. Thus, guidelines established upon the thermodynamic and kinetic properties of the thin film are essential for improving processing efficiency and enhancing overall product performance.

Chapter Two of this dissertation outlines the procedure for a novel method of quantifying the stratification of polymer blend thin films. Application of this technique revealed definitive control over the final film depth profile simply by altering the processing conditions. Instead of simply stating the effect of processing condition upon the final film depth profile and the extent of stratification, each processing condition was reported as the thermodynamic and kinetic properties of fabrication. Chapter Three expands upon the thermodynamic driving forces responsible for stratification outlined in Chapter Two and describes a hierarchy of thermodynamic properties responsible for stratification. Both Chapter Two and Three investigate the vertical stratification of a polymer blend. Chapter Four considers the lateral phase separation of the blend under the same thermodynamic and kinetic parameters. Chapter Five investigates the extent of

control substrate rigidity has upon the order of the thin film and the order at each interface of sputtered multi-layer thin films.

Ultimately, this work provides strong evidence that each processing parameter influences the entire structure of thin films. Control of polymer processing (either as a blend or as substrates) is crucial for product and thin film fabrication. The lack of control during processing will result in inconsistent final film structures, a film feature known to impact product performance. With the knowledge of stratification control and substrate influence upon final film structure, this information can be tailored to a diverse collection of polymer blended systems and endless multi-component applications.

TABLE OF CONTENTS

Chapter One Introduction 1
Surface Coatings 2
Multi-Layer Polymer Coatings 7
Single Step Processing of Multi-Component Systems 9
Driving Forces of Phase Separation 10
Practical Applications of Stratification 14
Current Technology Advances 16
Impact of Processing Parameters on Interfacial Width 17
Summary 19
Chapter Two Elucidating the Kinetic and Thermodynamic Driving Forces in Polymer Blend Film Self-Stratification 21
Abstract 22
Introduction 23
Experimental 26
Results 27
Discussion 43
Conclusion 50
Acknowledgements 51
Appendix 53
Chapter Three The Interplay of Thermodynamics and Kinetics: Imparting Hierarchical Control Over Film Formation of Self-Stratified Blends 63
Abstract 64
Introduction 65
Experimental 68
Results 69
Discussion 83
Conclusion 106
Acknowledgements 108
Appendix 109
Chapter Four A 3-Dimensional Assessment of The Lateral and Vertical Phase Separation of Immiscible Polymer Blend Thin Films 113
Abstract 114
Introduction 115
Experimental 118
Results 119
Discussion 131
Conclusion 142
Acknowledgements 143
Chapter Five Impact of Substrate Rigidity on the Composition and Density of Functional Multilayer Films 145

Abstract 146
Introduction 147
Experimental 149
Results 152
Discussion 172
Conclusion 181
Acknowledgements 182
Appendix 184
Chapter Six Conclusions and Future Work 189
Conclusions 190
Future Work 196
List of References 200
Vita 216

LIST OF TABLES

Table 2.1 Contact angles and calculated surface energies and measurements of the polymers studied. 44
Table 2.2 Solubility parameters at room temperature for P3HT and PMMA. 47
Table 3.1 Critical interaction parameters based on the molecular weight of P3HT and dPMMA in each blend. 89
Table 4.1 Solubility limits of the polymers studied in this chapter. 133
Table 4.2 The radii of gyration for PMMA and P3HT in chlorobenzene obtained via Zimm analysis with SANS. 135
Table 5.1 The scattering length densities for all the materials in this paper. 154
Table 5.2 The experimental neutron and x-ray SLD values of the 25 nm ITO layers as well as the calculated x-ray SLD values based on an ITO composition or density change. Asterisks denote expected density or composition. 157
Table 5.3 The experimental neutron and x-ray SLD values of the 50 nm ITO layers as well as the calculated x-ray SLD values based upon an ITO composition or density change. Asterisks denote expected density or composition. 162
Table 5.4 The experimental neutron and x-ray SLD values for W when deposited on a 25 nm ITO layer as well as the calculated x-ray SLD values based on a W density change. Asterisks denote expected density or composition. 164
Table 5.5 The experimental neutron and x-ray SLD values for W when deposited on a 50 nm ITO layer as well as the calculated x-ray SLD values based upon a W density change. Asterisks denote expected density or composition. 165
Table 5.6 The experimental layer thickness as measured with GISAXS for each sample. 188

LIST OF FIGURES

Figure 2.1 P3HT volume fraction depth profile illustrating the quantitative analysis of percent stratification, where V_{total} measures the sum of the areas of the black and white stripe region and the black and white checkerboard region, V_{sample} measures the area of the black and white checkerboard region, and the black horizontal baseline represents the baseline for V_{sample} which is equivalent to the concentration of P3HT in the sample. 30
Figure 2.2 P3HT volume fraction depth profiles of P3HT:131,500 g/mol dPMMA 5:95 (red), 10:90 (green), 15:85 (blue), 20:80 (black) blends spin cast from chlorobenzene at 104.7 rad/s where 0 is the air interface and 1 is the SiO_2. 32
Figure 2.3 Plot of the extent of stratification as a function of P3HT loading all prepared at 104.7 rad/s and 131,500 g/mol dPMMA. 34
Figure 2.4 Light reflectivity monitoring film formation of a P3HT:dPMMA 20:80 blend spin cast at 52.4 rad/s (top), 104.7 rad/s (middle), and 209.4 rad/s (bottom). 35
Figure 2.5 P3HT volume fraction depth profiles of a P3HT:dPMMA (131,500 g/mol) 20:80 blend spin cast from chlorobenzene at 209.4 rad/s (red), 104.7 rad/s (green), and 52.4 rad/s (blue) where 0 is the air interface and 1 is the SiO_2. Repeats of P3HT:dPMMA (131,500 g/mol) 20:80 samples prepared at 104.7 rad/s and 209.4 rad/s are included in the appendix. 37
Figure 2.6 Plot of extent of stratification as a function of spin speed, and P3HT:dPMMA composition 5:95 (red), 10:90 (green), 15:85 (blue), 20:80 (black). The P3HT volume fraction profiles for P3HT:dPMMA 131,500 g/mol samples of all blend compositions prepared at casting speeds of 52.4 and 209.4 rad/s can be found in the appendix. Additionally, repeats of P3HT:dPMMA (131,500 g/mol) 5:95 samples prepared at 52.4 rad/s and 104.7 rad/s are included in the appendix. 38
Figure 2.7 P3HT volume fraction depth profiles of a P3HT:dPMMA 5:95 blend spin cast from chlorobenzene at 104.7 rad/s with varying dPMMA molecular weights 520,000 g/mol (red), 316,000 g/mol (green), 131,500 g/mol (blue), 20,000 g/mol (black) where 0 is the air interface and 1 is the SiO_2 interface. 40
Figure 2.8 Plot of the extent of stratification as a function of dPMMA molecular weight and P3HT:dPMMA composition 5:95 (red), 10:90 (green), 15:85 (blue), 20:80 (black) all prepared at 104.7 rad/s. The P3HT volume fraction profiles for P3HT:dPMMA 20,000 g/mol, 316,000 g/mol, and 520,000 g/mol samples can be found in the appendix. 42
Figure 2.9 P3HT volume fraction depth profiles of P3HT:20,000 g/mol dPMMA 5:95 (black solid line), 10:90 (grey solid line), 15:85 (black dashed line), 20:80 (grey dashed line) blends spin cast from chlorobenzene at 104.7 rad/s where 0 is the air interface and 1 is the SiO_2. 54
Figure 2.10 P3HT volume fraction depth profiles of P3HT:316,000 g/mol dPMMA 5:95 (black solid line), 10:90 (grey solid line), 15:85 (black dashed line), 20:80 (grey

dashed line) blends spin cast from chlorobenzene at 104.7 rad/s where 0 is the air interface and 1 is the SiO_2..... 55
Figure 2.11 P3HT volume fraction depth profiles of P3HT:520,000 g/mol dPMMA 5:95 (black solid line), 10:90 (grey solid line), 15:85 (black dashed line), 20:80 (grey dashed line) blends spin cast from chlorobenzene at 104.7 rad/s where 0 is the air interface and 1 is the SiO_2..... 56
Figure 2.12 P3HT volume fraction depth profiles of P3HT:131,500 g/mol dPMMA 5:95 (black solid line), 10:90 (grey solid line), 15:85 (black dashed line), 20:80 (grey dashed line) blends spin cast from chlorobenzene at 52.4 rad/s where 0 is the air interface and 1 is the SiO_2..... 57
Figure 2.13 P3HT volume fraction depth profiles of P3HT:131,500 g/mol dPMMA 5:95 (black solid line), 10:90 (grey solid line), 15:85 (black dashed line), 20:80 (grey dashed line) blends spin cast from chlorobenzene at 209.4 rad/s where 0 is the air interface and 1 is the SiO_2..... 58
Figure 2.14 The original (grey solid line) and repeat (black solid line) P3HT volume fraction depth profiles of P3HT:131,500 g/mol dPMMA 20:80 prepared at 104.7 rad/s from chlorobenzene where 0 is the air interface and 1 is the SiO_2. 59
Figure 2.15 The original (grey solid line) and repeat (black solid line) P3HT volume fraction depth profiles of P3HT:131,500 g/mol dPMMA 20:80 prepared at 209.4 rad/s from chlorobenzene where 0 is the air interface and 1 is the SiO2. 60
Figure 2.16 The original (grey solid line) and repeat (black solid line) P3HT volume fraction depth profiles of P3HT:131,500 g/mol dPMMA 5:95 prepared at 52.4 rad/s from chlorobenzene where 0 is the air interface and 1 is the SiO2. 61
Figure 2.17 The original (grey solid line) and repeat (black solid line) P3HT volume fraction depth profiles of P3HT:131,500 g/mol dPMMA 5:95 prepared at 104.7 rad/s from chlorobenzene where 0 is the air interface and 1 is the SiO2. 62
Figure 3.1 A previously reported (Fig. 2.8) plot of extent of stratification as a function of dPMMA molecular weight and blend composition 5:95 (black stars), 10:90 (red stars), 15:85 (blue stars), and 20:80 (green stars) all prepared at 104.7 rad/s. 72
Figure 3.2 Previously reported (Fig. 2.6) plot of extent of stratification as a function of spin cast speed, and blend composition 5:95 (black stars), 10:90 (red stars), 15:85 (blue stars), and 20:80 (green stars) all prepared with 131,500 g/mol dPMMA. 73
Figure 3.3 Plot of extent of stratification as a function of dPMMA molecular weight, and blend composition 5:95 (black stars), 10:90 (red stars), 15:85 (blue stars), and 20:80 (green stars) all prepared at 209.4 rad/s. 74
Figure 3.4 Plot of extent of stratification as a function of dPMMA molecular weight, and blend composition 5:95 (black stars), 10:90 (red stars), 15:85 (blue stars), and 20:80 (green stars) all prepared at 52.4 rad/s. 76
Figure 3.5 Plot of extent of stratification as a function of spin cast speed, and blend composition 5:95 (black stars), 10:90 (red stars), 15:85 (blue stars), and 20:80 (green stars) all prepared with 316,000 g/mol dPMMA. 78

Figure 3.6 Plot of extent of stratification as a function of spin cast speed, and blend composition 5:95 (black stars), 10:90 (red stars), 15:85 (blue stars), and 20:80 (green stars) all prepared with 520,000 g/mol dPMMA. 80
Figure 3.7 Plot of extent of stratification as a function of spin cast speed, and blend 5:95 (black stars), 10:90 (red stars), 15:85 (blue stars), and 20:80 (green stars) all prepared with 20,000 g/mol dPMMA. 81
Figure 3.8 Plot of P3HT Volume Fraction Depth Profile for samples prepared with 20,000 g/mol dPMMA at 209.4 rad/s as a function of blend composition 5:95 (black), 10:90 (red), 15:85 (blue), and 20:80 (green). 86
Figure 3.9 Plot of P3HT Volume Fraction Depth Profile for samples prepared with 316,000 g/mol at 52.4 rad/s as a function of blend composition 5:95 (black), 10:90 (red), 15:85 (blue), and 20:80 (green). 91
Figure 3.10 Solubility of the polymers utilized in this study in chlorobenzene. 94
Figure 3.11 Plot of P3HT Volume Fraction Depth Profile for samples prepared with 520,000 g/mol at 52.4 rad/s as a function of blend composition 5:95 (black), 10:90 (red), 15:85 (blue), and 20:80 (green). 96
Figure 3.12 Plots of P3HT Volume Fraction Depth Profiles for samples prepared with 20,000 g/mol at 52.4 rad/s as a function of blend composition 5:95 (black), 10:90 (red), 15:85 (blue), and 20:80 (green). 101
Figure 3.13 Plots of P3HT Volume Fraction Depth Profiles for samples prepared with 20,000 g/mol at 104.7 rad/s as a function of blend composition 5:95 (black), 10:90 (red), 15:85 (blue), and 20:80 (green). 102
Figure 3.14 Plot of P3HT Volume Fraction Depth Profile for samples prepared with 131,500 g/mol at 52.4 rad/s as a function of blend composition 5:95 (black), 10:90 (red), 15:85 (blue), and 20:80 (green). 105
Figure 3.15 P3HT volume fraction depth profiles of P3HT:131,500 g/mol dPMMA 5:95 (solid black), 10:90 (solid grey), 15:85 (dashed black), 20:80 (dashed grey) blends spin cast from chlorobenzene at 209.4 rad/s where 0 is the air interface and 1 is the SiO2. 110
Figure 3.16 P3HT volume fraction depth profiles of P3HT:316,000 g/mol dPMMA 5:95 (solid black), 10:90 (solid grey), 15:85 (dashed black), 20:80 (dashed grey) blends spin cast from chlorobenzene at 209.4 rad/s where 0 is the air interface and 1 is the SiO2. 111
Figure 3.17 P3HT volume fraction depth profiles of P3HT:520,000 g/mol dPMMA 5:95 (solid black), 10:90 (solid grey), 15:85 (dashed black), 20:80 (dashed grey) blends spin cast from chlorobenzene at 209.4 rad/s where 0 is the air interface and 1 is the SiO2. 112
Figure 4.1 P3HT volume fraction depth profiles for P3HT:dPMMA (a) 5:95 and (b) 20:80 cast from chlorobenzene at 209.4 rad/s (red), 104.7 rad/s (green), and 52.4 rad/s (blue) where 0 is the air interface and 1 is the SiO2 interface. 122
Figure 4.2 Plot of extent of stratification as a function of spin speed, and blend composition, P3HT:dPMMA 5:95 (blue squares) and 20:80 (orange squares). 124

Figure 4.3 Small-angle neutron scattering curves of P3HT:dPMMA 5:95 (blue closed shapes) and 20:80 (orange open shapes) prepared at 209.4 rad/s (triangles), 104.7 rad/s (squares), and 52.4 rad/s (circles). 126
Figure 4.4 DAB model fit (black trace) for a P3HT:dPMMA 5:95 sample prepared at 107.4 rad/s. 127
Figure 4.5 Plot comparing correlation length derived from the model fits for both P3HT:dPMMA compositions 5:95 (blue squares) and 20:80 (orange squares) as a function of spin speed. 129
Figure 4.6 Plot comparing Σ* for both P3HT:dPMMA compositions 5:95 (blue squares) and 20:80 (orange squares) as a function of spin speed. 130
Figure 4.7 Schematic depiction of thin film orientation during both Neutron Reflectivity (a) and Small Angle Neutron Scattering (b) measurements. The orange arrows represent the path neutrons take before and after they hit the sample. 139
Figure 4.8 Schematic depiction of vertical and lateral phase separation. Illustrations are representations of reflectivity (a, b, c) and small angle neutron scattering (d, e, f) samples collected at 209.4 rad/s, 104.7 rad/s, and 52.4 rad/s, respectively. 140
Figure 5.1 An illustration of the thin film orientation where the ITO layers were sputtered directly onto the substrate and W layers were sputtered onto ITO. 150
Figure 5.2 The neutron (a) and x-ray (b) SLD depth profiles for 25 nm ITO (Si/red, PET/dotted dark blue), 25 nm ITO plus 10 nm W (Si/orange, PET/dotted light blue), and 25 nm ITO plus 20 nm W (Si/pink, PET/dotted purple). 155
Figure 5.3 The neutron (a) and x-ray (b) SLD profiles for 50 nm ITO (Si/red, PET/dotted dark blue), 50 nm ITO plus 10 nm W (Si/orange, PET/dotted light blue), and 50 nm ITO plus 20 nm W (Si/pink, PET/ dotted purple). 159
Figure 5.4 Qz line cuts of the GISAXS two-dimensional detector for Si + 25 nm ITO (red), Si + 50 nm ITO (gold), PET + 25 nm ITO (blue), PET + 50 nm ITO (green). 168
Figure 5.5 Qz line cuts of the two-dimensional detector images for 25 nm ITO + 10 nm W (Si/red, PET/light blue), 50 nm ITO +10 nm W (Si/orange, PET/purple) (a) and 25 nm ITO + 20 nm W (Si/red, PET/light blue), 50 nm ITO + 20 nm W (Si/orange, PET/purple) (b). 169
Figure 5.6 Qz line cuts of the two-dimensional detector images for 25 nm ITO + 10 nm W (Si/red, PET/light blue), 25 nm ITO + 20 nm W (Si/orange, PET/purple) (a) and 50 nm ITO + 10 nm W (Si/red, PET/blue), 50 nm ITO + 20 nm W (Si/gold, PET/green) (b). 170
Figure 5.7 Qz line cuts of the two-dimensional detector images for PET + 25 nm ITO (blue), PET + 25 nm ITO + 10 nm W (red), PET + 25 nm ITO + 20 nm W (black) and their repeats (dashed lines). 171
Figure 5.8 The penetration depth of the incident x-ray on each material. The number annotations denote the penetration depth (Å) with an incidence angle of 0.2°. The numbers for each ITO material are density values (g/cm3). 185
Figure 5.9 Two-dimensional detector images for the GISAXS measurements of ITO and W samples on silicon substrates. 186

Figure 5.10 Two-dimensional detector images for the GISAXS measurements of ITO and W samples on PET substrates. 187

CHAPTER ONE INTRODUCTION

Surface Coatings

Surface coatings are used to protect a structure against environmental contaminants or to improve its aesthetic properties. Many of the first coatings were paint based, however many other functional coatings impart surface focused properties such as scratch resistance, anti-reflective properties, corrosion resistance, flame retardance, etc. Metal, ceramic, porcelain, and natural and synthetic polymers have all been applied to surfaces to provide such specific properties. One of the most commonly used metal coatings is zinc, or galvanization, to protect steel from rusting. Porcelain and ceramic coatings are also widely used to improve the appearance of products. Improvement of coating quality is most commonly completed through compositional modifications such as improving purity, including additives, or changing the source of the material. Often the material's source maintains a specific chemical composition of the material—a property shown to impact the overall effectiveness of the coating.[1] The role of polymeric materials as coatings has become increasingly important due to the capability to intelligently design and control the chemistry and functionality of polymers in a cost effective manner.

The idea of polymers and polymerization was introduced in the mid 1830's, however, the chemical understanding of polymer science was not developed until almost a century later.[2] Since then, the capabilities and applications of polymer chemistry continue to broaden. Polymers are now used in cell phones, tires, food packaging, and dentistry. Utilizing polymers for these applications, rather than metallic alloys or ceramic materials, provides the benefit of polymer property customization based upon the chemical

composition and polymer architecture. Careful synthesis can provide various polymeric architectures such as linear polymers, block copolymers, random copolymers, combs, bottlebrushes, and star polymers. Access to these architectures provides additional handles to tune surface sensitive or bulk properties such as viscosity (chain mobility), thermal properties including melting temperature, and mechanical properties such as impact resistance. For example, polyethylene can be synthesized with varying amounts of branching and the degree of polyethylene branching dictates the density, viscosity, and crystallinity.[3,4] This molecular level control translates to alterations of macroscopic properties to provide endless opportunities for new polymer applications, including surface modification and coatings.

Recent efforts in polymer chemistry have focused on preparing multi-component, multi-functional polymer systems. These polymer systems range from nanocomposites, polymer blends, or dual-functional block copolymers. Polymer nanocomposites are defined as a polymer matrix containing a dispersed phase of particles with at least one dimension on the nanoscale.[5] The inherent properties (mechanical, thermal, optical) of the nanoparticles are provided to the composite and a new material with enhanced versatility is obtained. For example, carbon nanotubes provide remarkable strength to composite materials without adding significant mass to the material, an issue with traditional metal additives.[6] Nanocomposites containing carbon reinforcement are ideal materials for aerospace technologies to reduce fuel consumption and aircraft drag.[7] However, the added small molecules or nanoparticles pose a threat of leaching over time.[8] Nanoparticle or small

molecule leaching reduces the observed properties of the composite, leading to material failure and reducing the composite lifetime. One method to circumvent small molecule leaching is to use larger polymer additives to create polymer blends or to connect two polymers as block copolymers. Polymer blends are mixtures of two or more polymeric materials, while block co-polymers are defined as linear blocks of two (or more) polymeric materials covalently bonded at a single location.[9,10] The blending or bonding of two or more materials leads to new or a larger arsenal of material properties, without the implications of small molecule leaching. However, mixing polymers does not always elicit a homogenous system. In fact, polymer mixing is generally unfavorable and leads to macroscopic phase separation while the physical connection between incompatible polymers leads to an abrupt transition of chemical and/or physical properties dependent upon the interactions and properties of the polymeric materials in the copolymer.[10–12] Compatibility between the polymers in the system is essential for the development of homogenous, processable, functionable polymer blend or block copolymer systems. Thus, rather than combining specific polymers, incorporating multiple structural functionalities responsible for the desired properties into a single polymer can improve the versatility of the coating and permits the optimized protection of a surface.

Many applications utilize multi-functional polymers, such as random copolymers, as protective coatings.[13–15] A random copolymer is a polymer consisting of two or more monomeric constituents connected in a random order.[16] Random copolymers allow for simplistic modification of the chemical composition through the ordering or the relative

ratio of monomers present in the polymer backbone. Chemical modifications also impact the macroscopic properties of random copolymers such as the surface energy, mechanical strength, and thermal properties of the polymer.[17–19] As an example, random copolymers are often used in anti-fouling applications to tailor the hydrophilicity of the polymer by controlling the ratio of hydrophobic to hydrophilic functional segments.[18] The hydrophilicity of an anti-fouling material is important because bacterium and other foulants have specific environments that foster population growth. To combat the fouling, the polymeric surfaces are engineered to maintain a specific chemistry to ward off and discourage bacterial attachment and growth.[20] Foulants are classified as either hydrophobic or hydrophilic based upon the environment that promotes their survival.[21] Altering the overall hydrophilicity and hydrophobicity of a polymer allows for the development of a material aimed towards reducing both hydrophobic and hydrophilic interactions.[22] This controlled manipulation of the coating hydrophilicity to deter foulant growth is defined as passive protection.[23] Active protection of a surface for anti-fouling is defined as chemically modifying a polymer to contain functionalities responsible for foulant proliferation or death.[18] The proliferation of bacterium is typically controlled via specific bacteria protein expression and interaction of the bacteria with the surrounding environment.[24] Once the proteins on the surface of a bacterium responsible for lysis are activated, the bacterium proliferates.[25] Another hypothesized method to cause bacterial death is to interrupt the message from surface proteins communicating a safe environment to adjacent bacteria.[18] The specific enzymes known to deactivate the environmental-based communication are

known to be quaternary ammonium salts, graphene oxide, antibiotics, or silver nanoparticles.[18] The research regarding bacterial death has been applied to polymer science to develop materials with an active defense system against fouling.[26,27]

Advanced polymer synthesis such as atom-transfer radical-polymerization (ATRP) has been recognized as a versatile technique to engineer the required chemical functionalities and specific architectures necessary for effective anti-fouling surfaces.[18] ATRP is a controlled living polymerization method meaning it is relatively insensitive to slight changes in the polymerization conditions and tolerates a wide range of monomer compositions and functionalities.[28,29] Additionally, ATRP surface bound initiators generate polymerization directly from the surface—ideal for tunable, active foulant protection.[27] ATRP has been utilized to develop surface bound polymer brush architectures with an optimized ratio of poly(ethylene glycol) and poly(methyl methacrylate) block functionalities.[30] The copolymers used in this study were further optimized to contain covalently bonded enzymes to facilitate the proliferation of specific classes of bacteria. The ability to functionalize and combine various polymers based on their chemical composition, functionalities, and overall architectures leads to endless opportunities to develop novel materials that contain a broad range of properties not only to limit fouling, but for applications ranging from anti-scratch to water resistance.

Nevertheless, the seemingly simplistic combination of functional properties from specific monomers, segments, and polymers into a multifunctional polymer system does not always elicit a material with the desired properties from each component. It is not

uncommon that two polymers/components interact unfavorably. These incompatible interactions lead to aggregation and phase separation, and as a result can inhibit the performance of multi-functional homogenous systems.[31,32] Contrarily, the two structurally different components may interact favorably, which may provide an effective dual-functional coating.[33] However, the dynamics and behaviors present in the neat component can merge into a single property that is the average of all components, rather than multiple distinct responses that are dominate by the response of individual components. This phenomenon is realized in many block copolymer systems, where the individual glass transition temperatures (T_g) of the homopolymers merge into a single broad T_g.[34–37] Because of the unpredictability of blending or combining functional materials into a single coating, maintaining the purity of individual single layer coatings is highly desirable. Unfortunately, there is a lack of control of mixing, layering, and organization in multi-component thin films, which clearly demonstrates the need for further evaluation and understanding of the assembly and formation of multi-layer coatings.

Multi-Layer Polymer Coatings

Not surprisingly, multi-component coatings have many advantages over the single component systems. Utilizing highly characterized materials with desirable properties bypasses the need for the development of new materials and exploration of the required processing protocols to fabricate thin films of a new material. Traditional fabrication of multi-functional coatings requires the layering of each individual layer sequentially onto the surface where each individual layer provides a specific and unique function. This

alternating deposition of pure materials evades the potential unfavorable interactions that lead to a decrease in the desirable properties of the pure material. The unfavorable interactions are often observed when blending or covalently bonding two polymeric materials (block copolymers). However, each of the deposited layers must adhere strongly to not only the substrate, but also to one another. Intelligent design of the order of deposition of the layers must also be considered. The exterior layers provide surface durability and the most protection against corrosion while the internal layers provide additional functionality and are responsible for adhering sequential layers together.[38] The interactions between layers must also be considered where a poor interaction between materials can lead to delamination, bubbling, peeling, and eventual overall coating failure. Additionally, increasing the number of layers in the coating increases the quantity of interfaces present as well as the total thickness of the film. Multiple layers and interfaces between incompatible materials requires additional adhesive layers to prevent peeling and overall film failure.[39] Adhesive layers further increase the overall thickness of the film which has shown to decrease overall film stability and reliability, and in certain cases, decreases the ability for each layer to maintain peak performance.[40–42] Including cross-linkable groups in adjacent layers has proven effective to avoid the need for excessive adhesive binders between layers.[43,44] The chemical crosslinks are designed to remain at the interface to the proceeding layer and during deposition, the cross-linkable groups react to form covalent bonds at the interface. Rather than solely relying on the adhesive behavior of a binder or the mixing of two incompatible materials, a physical bond is formed and

strengthens the interface between adjacent layers. The most widely used crosslinking reactions for covalently bonding adjacent layers are quick, stable, and uncatalyzed reactions such as polycondensation reactions or click chemistry.[45,46] Even with the ability to chemically alter and strengthen polymeric surfaces by incorporating cross-linkable groups, the layer by layer assembly of multi-functional multi-layer thin films is time consuming, labor intensive, and economically inefficient especially when the specification profile for technological component and layer is vastly different. Therefore, an alternate route of fabricating multi-component coatings is required.

Single Step Processing of Multi-Component Systems

Self-stratification is a term used to define the self-assembled layering of two or more materials deposited from a single solution.[31] Utilizing self-stratification allows for one step processing which can lead to lower production costs because it eradicates any necessary post-modification of the material.[47] A second advantage of using single solution deposition for surface coatings is improved inter-layer adhesion which increases product service life and eliminates the need for an adhesive binder between layers. Because of the economic benefits of self-stratification, it has been employed in a wide array of applications from all-in-one paints and primers to thin films used for organic field effect transistors.[43]

In 1976, Funke and his collaborators were the first to introduce the concept of self-stratification with powdered polymers on a metal substrate.[48] Once at a temperature above the melting temperature, the polymers rearranged to minimize the free interfacial energy

and formed layered morphologies.[38] They attributed the spontaneous rearrangement during heating to the solubility parameters, and relative viscosities and surface tensions of the two polymeric powders. Further research by Verkholantsev applied self-stratification to solvent-based systems.[49] This research investigated the liquid phase separation of paints and coatings diluted in a common solvent. These experiments identified that the organized phase separation of liquids occurred during solvent evaporation and specific driving forces for self-stratification were recognized.[49] Some of the specifications, or driving forces documented to initiate self-stratification were the incompatibility of the two materials as well as the selective wetting of the substrate by one component during solvent evaporation. Verkholantsev also suggested potential parameters that change the vertical structures obtained from self-stratification include varying the polymer/polymer ratio, choice of solvent, and introducing small molecule additives to initiate and catalyze phase separation.[49]

Driving Forces of Phase Separation

The concept of controlling self-stratification for application specific systems has developed into an interesting avenue of research. Many researchers have developed theoretical requirements for controlled self-stratification and have concluded that balanced interactions among polymer blend, solvent, and substrate lead to polymer self-assembly.[38,49–52] The polymers selected for self-stratification must have a certain degree of incompatibility. The incompatibility of polymers in a blend is best described by the propensity of the polymers to mix defined by the Flory Huggins theory (Equation 1.1).

$$\Delta G_m = RT[\frac{\phi_1}{N_1}\ln\phi_1 + \frac{\phi_2}{N_2}\ln\phi_2 + \phi_1\phi_2\chi_{12}] \quad \text{Equation 1.1}$$

Mixing of a polymer blend will occur when the balance of enthalpic and entropic terms provide a negative net change of ΔG_m. The first two terms within the brackets of Equation 1.1 represent the entropic component of the blend while the last term in the bracket represents the enthalpic mixing contribution. Inside of these terms, $N_{1\ or\ 2}$ and $\phi_{1\ or\ 2}$ represent the degree of polymerization and the volume fraction of polymer 1 or polymer 2, respectively. The entropic contribution in Equation 1.1 clearly shows that simply by altering the molecular weight of either polymer or changing the compositional ratio of the blend impacts the entropic contribution to mixing and the ability for the polymer to mix. The χ_{12} term is defined as the enthalpic interaction parameter of the polymer blend. The interaction parameter can be estimated for each polymer blend using Hildebrand solubility parameters ($\delta_{1\ or\ 2}$) as shown in Equation 1.2.

$$\chi = \frac{V_1}{RT}(\delta_1 - \delta_2)^2 \quad \text{Equation 1.2}$$

The Hildebrand solubility parameters are roughly estimated by the enthalpic contribution as a function of total volume of the polymer. By employing these two equations, the compositional range for theoretical miscibility of a polymer blend can be estimated.[53]

The miscibility of the polymer blend is a crucial driving force for phase separation, yet the surface energy differences at the substrate and air interface biases directional phase separation. The substrate must be compatible with one of the polymers in the blend. To determine the compatibility of polymers and substrates, the surface energy of each component must be considered. Surface energy of substrates is calculated with Owen and

Wendt's equation (Equation 1.3) where each radical term represents the polar component and the dispersion component of surface energy. To determine the surface energy of the substrate ($\gamma_s^{p,d}$), the contact angle of at least two liquids (*li*) with known dispersive and polar surface energy components are monitored on the surface of interest to set up a system of equations.[54]

$$(1 + \cos\theta_i)\,\gamma_{li} = 2\left(\sqrt{\gamma_s^d \gamma_{li}^d} + \sqrt{\gamma_s^p \gamma_{li}^p}\right) \qquad \text{Equation 1.3}$$

The preferential wetting of one polymer onto the substrate will occur when the surface energies between the polymers in the blend are different and the polymer with the smallest surface energy will approach the air interface during film fabrication to decrease the overall free energy in the film.[55] The substrate surface energy controls the total degree of bias and the total driving force for vertical stratification based upon the differences in polymer surface energy.

The one step processing of a polymer blend is only possible when both polymers can be dissolved in a common solvent. The common solvent may not be ideal for either polymer in the blend and thus the choice of solvent can influence the morphology and stratification of the final film. Solvent properties to consider are the viscosity, vapor pressure, and solubility of each polymer all of which greatly influence the kinetics and dynamics of film formation.[56,57] The understanding of the solvent's role in self-stratification is vague and not well understood. One study by Heriot and Jones utilizes light reflectivity and scattering to determine the onset of phase separation and the film formation time.[58] They then correlate this information to the surface structure of the fabricated thin

films. Their results prove that the evaporation rate of solvent dictates the ability for a polymer blend film to stratify vertically or simply phase separate laterally. The hypothesis generated from this work is that the thin film morphology changes throughout film formation and is kinetically frozen when solvent diffusion is reduced, or when the solvent completely evaporates. The results indicate the initial depth profile structure obtained is a vertically stratified structure and further instability at this interface drives lateral phase separation, but it is unclear the role the polymer blend interactions or substrate interactions play in the final film morphologies. Moreover, the solvent-polymer interactions are not addressed.

A second study conducted by Brigham and coworkers investigated the crystallization patterns of block copolymers in various solvents.[59] This work proved that favorable solvent interactions with a single block facilitated its organization while the other block failed to crystallize. Additionally, the block that failed to crystallize precipitated from solution prematurely. The precipitation inhibited the ability of the blocks to organize into a thermodynamically stable crystalline state. These two studies indicate and emphasize that the solvent selection is important when designing a self-stratifying system.

Polymer blend self-stratification is a widely accepted method of thin film fabrication and has been incorporated in many dual-functionality applications. Thermodynamically stable coatings with vastly different final film morphologies from self-stratification can be fine-tuned by simply altering the processing conditions. Complete stratification is commonly defined as two pure layers with a sharp interface, but the pure

layers could also appear at opposite substrate and air interfaces with a gradient compositional transition throughout the film. The vast differences in depth profiles obtained via self-stratification is largely beneficial as various applications often require specific thin film vertical morphologies and by altering the processing conditions of self-stratification many thin film depth profiles are possible.

Practical Applications of Stratification

Many of the first practical applications of self-stratification were resins due to their promising properties relevant for various applications such as adhesives, reinforcement, and various surface finishes/protection.[60] Resins are classified as low-molecular weight macromolecules containing reactive functional groups. As a resin is introduced to a curing agent, a crosslinking reaction is initiated and depending on the chemical composition and chemical nature of the macromolecule and curing agent, thermoplastic or thermoset materials with varying hardness, strength, and durability are generated.[61] Prior to utilizing stratification as the fabrication method for coating, the adhesive layer and protective top coat were applied individually. This process is labor intensive, requires substantial drying time for each layer, and coating failure often resulted due to peeling between layers. Stratification occurs as the solvent evaporates thus creating a compositional gradient throughout the drying film.[38] The compositional gradient reduces the potential peeling between adjacent functional layers.[38] Additionally, the substrate surface energy dictates the compositional arrangement throughout the depth of the film, creating distinct hydrophobic, durable, top coat and polar, adhesive, undercoat layers. Self-stratification not only reduces

the cost and processing time of multi-component resins, the lifespan of the coating improves by eliminating interlayer failure, and all the advantages of utilizing self-stratification are obtained without compromising the application specific properties. The promise for control of final film morphology without reducing overall film properties and function through a one step, self-stratification fabrication method is desirable for a wide array of applications and has been applied to many other systems.[43,51,62,63]

Due to the push for organic materials in electronic devices and the requirement of a well-defined interface between transport layers and insulators in organic transistors, solution processing methods of conjugated polymers was especially desirable. One of the main challenges for the solution processing of organic electronics was the layer-by-layer fabrication where underlying insulating polymer layers experienced damage during deposition of the surface-most conjugated polymer layer. Therefore, single step processing of the insulating and conjugated polymer blends became an attractive avenue to pursue.[64] The fundamental goal of utilizing self-stratification for organic electronics was to optimize the electronic properties and efficiency to increase the feasibility of transitioning traditional metal-based electronics to include organic components. Even with the well-established understanding of the required morphology, layer purity, and breadth of the insulating and conjugated polymer interface, the overall depth profile of the film is oftentimes overlooked. More commonly, the depth profile of the film as a function of processing conditions was acknowledged to prove vertical stratification occurred, but the wholistic understanding of the interfacial morphology and its impact upon electronic properties is rarely discussed.[65]

Additionally, because the combined goal of the field of organic electronics and single step processing is to push and expand the limits of electronic properties, thermal annealing was used to improve the morphology to obtain increased levels of electronic efficiency.[66] The discussion of the impact of thermal annealing on the polymer blend greatly overlooks the rearrangement of polymer into a desired morphology which resulted in the increased electronic efficiency. Moreover, utilizing an additional post-modification step further increases the production time of organic electronics, which is one of the critical reasons traditional layer by layer processing was replaced.

Current Technology Advances

Current technology advances are also interested in using flexible substrates for electronic devices. The development of non-rigid devices would make smart clothing and plastic, flexible electronics a reality.[67] To begin to recognize the possibility of flexible electronics, studies have applied the single-step solution processing of electronic, polymeric materials to flexible substrates. Although the single-step process has shown promising electron mobility and high device efficiency on rigid substrates, these properties do not translate to flexible substrates.[65] One of the major drawbacks of exchanging the substrate for one-step processing is a change in the surface energy because the substrate surface energy plays a large role in polymer rearrangement during stratification.[68] This translates to mean that the same processing conditions used for a rigid substrate cannot be applied to the flexible substrate strictly because of the change in surface energy.

Additionally, changing the mechanical properties of the substrate may also influence the stratification of a polymer blend and the durability of the overall device. One of the biggest advantages to using a rigid substrate is the inherent ability to absorb external force.[69] When external force such as vibration or bending is applied to a rigid substrate, it can absorb a certain extent of external forces prior to failure. By absorbing this force, the substrate provides protection the functional materials in the device. On the other hand, when a flexible substrate is utilized, the desirable flexible property no longer provides the same protection as a rigid substrate.[70,71] The lack of protection present in flexible substrates may translate to layer and interfacial roughness in thin films that were not present in films with rigid substrates.

The understanding of the impact of the flexible substrate on self-stratification is described as the difference in substrate rigidity, surface energy, and interfacial width. To combat these differences in substrate qualities and to obtain similar electronic efficiencies, thicker insulating and conjugated polymer self-stratified films are necessary. However, the impact of the differences in substrate surface energy, roughness, and rigidity on the structures in the thin film depth profile were not discussed.

Impact of Processing Parameters on Interfacial Width

Many of the current studies of self-stratification focus on the processing parameters and their impact of application specific properties.[65,72–74] The presence of two distinct layers produced from single-step processing of self-stratification is acknowledged by recent studies, but the details of the self-stratified thin film depth profile (purity of layers,

interfacial breadth, layer thickness) are vague. The most common methods to determine the stratified final film depth profile are x-ray photoelectron spectroscopy, transmission electron microscopy, and atomic force microscopy. X-ray photoelectron spectroscopy provides valuable information of atomic concentration as a function of depth within the film. However, this method has limited resolution (resolves ~3 nm), is destructive and once this characterization is complete, no further characterization can proceed.[75] Transmission electron microscopy is a useful method in proving the stratification of the polymer blend thin film, however, the characterization is qualitative, and the composition of each layer and the breadths of the interfaces are unclear given the instrument resolution. Atomic force microscopy provides the roughness of the surface, and possibly the interface between the layers, however, to determine the roughness at the interface, the surface most polymer must be selectively extracted with solvent, destroying the film for further analysis. Additionally, solvent extraction can damage the interface of interest by removing or dislodging any mixed polymer at the interface, making any analysis unreliable. The complete understanding of the structural information present in the final film includes the ability to quantitatively define the composition as a function of depth, compare interfacial width between stratified layers, and define independent layer thickness or lateral domain size. With the knowledge that structure of the thin film impacts the application properties, it is inherent that understanding the impact of processing parameters on the final film depth profile and interfacial quality be the focus of this dissertation. In this dissertation, we investigate the final film structures utilizing neutron scattering and neutron reflectivity

because of their non-destructive nature and utilizing these characterization methods afford the ability to determine thin film depth profiles with resolution of half a nanometer.

The current brevity of understanding of the morphologies and depth profiles obtained through self-stratification requires further scientific exploration. With the wealth of knowledge of the thermodynamics of polymer blends combined with precise control of the processing of these complex systems, the ability to correlate the structure and properties of polymer blends to the final film morphologies can be generated. Once this correlation is made, the final film morphologies can be described as a function of thermodynamic and kinetic driving forces, rather than system specific processing parameters. A better grasp of the thermodynamic and kinetic driving forces affords an improved and more complete understanding of self-stratification. This knowledge can then be applied to diverse polymer blends and a multitude of applications where the required final film structure is well understood.

Summary

Surface coatings are imperative for effective performance and longevity of a product. The coating properties are often dictated by the functional groups present in the polymeric material and the final film morphology. New polymeric materials are constantly developed to provide increased coating performance. However, each new material requires specific and unique processing for the optimized longevity of the coating. The current approach to optimize the coating properties is on a system by system basis which is time consuming and economically inefficient. Therefore, the goal of this dissertation is to

develop thermodynamic and kinetic guidelines which obtain specific thin film morphologies, interfacial width, and domain purity.

The qualitative nature of describing morphology inhibits direct assessment and comparison of two structurally different films. Chapter 2 of this dissertation outlines a novel quantitative method to systematically describe the extent of stratification of a polymer blend thin film. This quantitative method allows for direct evaluation of processing conditions and the final films produced. Chapter 3 further elaborates on the results described in Chapter 2. Chapter 3 determines that there is an apparent hierarchy of thermodynamic driving forces which control the final film morphologies. Both Chapters 2 and 3 investigate the vertical stratification of a polymer blend while Chapter 4 considers the holistic polymer blend phase separation by including the phase separation parallel to the substrate. Finally, the impact of substrate flexibility on interfacial width and layer composition is monitored in Chapter 5. Investigating the thin film self-stratification of polymer blends as a function of thermodynamic and kinetic parameters is a necessary next step to further implement one-step solution processing into the fabrication of endless applications. Additionally, expanding thin film fabrication onto flexible substrates and understanding the substrate influence upon the overall quality of the thin film is fundamental in realizing the feasibility of flexible electronics.

CHAPTER TWO ELUCIDATING THE KINETIC AND THERMODYNAMIC DRIVING FORCES IN POLYMER BLEND FILM SELF-STRATIFICATION

Abstract

Self-assembly of immiscible polymer blend films during deposition presents an attractive avenue to fabricate structured multi-component thin films. Depth profiles formed by self-stratification during spin casting can be varied simply by modifying processing conditions, even on short time scales. However, the current practice of self-stratification utilizes polymer blends that are specific for optimizing properties of a desired application and provides little insight into the underlying driving forces that guide the process of stratification. Our research seeks to fill this gap by using neutron reflectivity to monitor the stratification of blends consisting of poly(3-hexylthiophene-2,5-diyl (P3HT) and poly(methyl methacrylate) (PMMA) as a function of sample and processing condition: spin casting speed, polymer blend composition, and polymer molecular weight. Each of these parameters were varied individually, and each parameter provided orthogonal control of the extent of stratification. An increase in the concentration of P3HT in the blend composition increased the immiscibility between the two polymers which leads to an increase in stratification. A reduction in the similarity of polymer molecular weights in the blend reduced the entropic driving force of stratification. Additionally, when casting speed was decreased, and all thermodynamic conditions were left unchanged, we observed a longer film formation time and an increase in extent of stratification. Longer film formation times allow more time for the thermodynamic driving forces to dictate the rearrangement of polymer towards equilibrium. Furthermore, by changing the relative molecular weight of the polymers, the purity of the P3HT layer at the air interface improved, where the largest

molecular weight PMMA resulted in the purest P3HT rich layer. The interfacial width between the P3HT rich layer and the PMMA rich layer was also controlled by changing the composition of the blend, where the blend with the highest concentration of P3HT resulted in the sharpest interface.

We attribute the differences in vertical morphology to the control of the thermodynamic properties of each blend, including total entropy of the system, surface energy, and the χ interaction parameter. Through careful regulation of the processing conditions of P3HT:PMMA thin films, these results provide insight into *both* the kinetic and thermodynamic factors that direct the self-stratification of polymer blend films. This fundamental study of stratification for P3HT:PMMA blends provides the foundation to develop a global understanding of self-stratification and to impact a wide range of technologies by developing cost-efficient protocols for multi-layer film deposition of structured thin films without post-modification processes.

Introduction

Polymer coatings serve a wide array of purposes, where many specific applications require multi component coatings.[44,76–79] These coatings are typically applied in a layer by layer fabrication process. In addition to the deposition of each layer for its desired application, adhesive binders are often required between layers to prevent peeling and improve durability of the entire coating system.[76] This layer by layer assembly is inefficient and in order to combat this, the stratification of multiple materials from a single step solution process may be employed to improve the efficiency of film fabrication.[38,55,80]

Utilizing self-stratification decreases the number of depositions which leads to lower production costs as it eradicates time consuming post-modification processes of the material.[47]

Much of the current investigation of self-stratification of blend films involves altering the processing conditions and correlating these processing conditions to final film properties, for example device performance or durability.[65,74,81–83] To the best of our knowledge, there is limited knowledge of the thermodynamic and kinetic driving forces that guide the self-stratification process, which is needed to more rationally control of final film morphology.[56] For example, in many thin film applications, polymers processed from different casting solvents result in films with contrasting properties.[84] Yet it is unclear whether changing the solvent has a larger impact upon the kinetic drying time of the film, or the thermodynamic interactions of the system, and which of these two properties controls and guides the formation processes that impact the final film structure and properties. Our studies will focus on the common film formation process of spin coating, which is a non-equilibrium process.[85,86] Therefore, in order to identify the driving forces that guide film formation, it is necessary to regulate multiple parameters to derive an understanding of the thermodynamic and kinetic processes that impact the measured film structure and properties.

Typically, stratification is examined via depth profiles derived from optical microscopy, or ion sputtering mass spectroscopy,[66,87,88] both of which provide a qualitative picture of the polymer blend stratification. Our research will utilize neutron reflectivity to

provide a quantitative assessment of the impact of spin casting speed, polymer blend composition, and polymer molecular weight on the stratified sample's depth profile and structure. These processing parameters were selected to provide insight into the effect of surface energy, polymer-polymer interaction parameters, and film drying kinetics on final film formation and polymer blend stratification. To realize this goal, a quantitative method was developed to analyze the final film's extent of stratification, so that the thermodynamic and kinetic driving forces that guide final film structure and total stratification can be more thoroughly investigated.

The focus of this research is a conjugated and insulating polymer blend, poly(3-hexylthiophene-2,5-diyl) (P3HT) and poly(methyl methacrylate) (PMMA), which are used as benchmark polymers for organic field effect transistors. Utilizing these two polymers is advantageous because they phase separate upon deposition into practical morphologies suitable for solution processing of electronic devices.[89,90] Recent studies have documented how specific deposition conditions impact the performance of these devices, but disregard how the thin film structure and thus, in turn, device performance may be *tuned* with control of the final blend film stratification.[91–94] Providing insight into the role of specific thermodynamic and kinetic parameters on the film formation process will greatly impact the ability to control, engineer, and improve these films for desired application performance. [95–98] Thus, the development of a holistic understanding of the driving forces behind polymer blend stratification provides an innovative pathway to control final film morphology simply by changing the polymer blend and processing conditions.

Experimental

Chlorobenzene (Sigma Aldrich), Poly(3-hexylthiophene-2,5-diyl) (P3HT) (Ossila, regioregularity-95%, and number-average molecular weight (M_n) 19,500 g/mol and polydispersity index (PDI) 1.75) and deuterated poly(methyl methacrylate (dPMMA) (Polymer Source Inc., M_n (PDI), 20,000 g/mol (1.6), 131,500 g/mol (1.4), 316,000 g/mol (1.35), 520,000 g/mol (1.4)) were used directly from the supplier and were not further purified. Polymer blends were dissolved at 1 percent by mass in ratios of P3HT:dPMMA 5:95, 10:90, 15:85, 20:80 in chlorobenzene. These polymer blends were dissolved at 55 °C overnight into a homogenous solution. Thin films were prepared by spin coating (209.4 rad/s, 104.7 rad/s, and 52.4 rad/s) the chlorobenzene solutions onto Si wafers. The Si wafers were cleaned in a piranha solution (3:1 ratio of sulfuric acid and hydrogen peroxide), washed with nanopure water, and allowed to sit under UV irradiation and ozone for 30 minutes prior to film deposition.

Neutron reflectivity experiments were conducted at both the National Institute of Standards and Technology's Center for Neutron Research using the NG7 beamline and the Spallation Neutron Source at Oak Ridge National Laboratory with a Q range of 0.008-0.2 A^{-1} where $Q= 4\pi/\lambda \sin(\theta)$; λ is the neutron wavelength, and θ is the angle of incidence. The data for all incident angles was reduced utilizing the NCNR software.[99]

Time-resolved light reflectivity was measured with an in-situ apparatus to monitor film formation during the spin casting process under the same conditions discussed above.

A P3HT:dPMMA (520,000 g/mol) 20:80 solution was spin cast at 209.4, 104.7, and 52.4 rad/s. The procedure is described elsewhere.[86]

The surface energy of protonated poly(methyl methacrylate) (H-PMMA) was determined using contact angle measurements. H-PMMA was obtained from Acros (M_n 15,000 g/mol) and Sigma-Aldrich (weight average molecular weight (M_w) 120,000 g/mol and 350,000 g/mol). M_n 520,000 g/mol dPMMA was obtained from Polymer Source. Contact angle measurements were conducted at the Chemical Sciences Division at Oak Ridge National Laboratory utilizing a Kruss DSA 100 Standard Optical Microscope. Drops of water and diiodomethane were placed on thin films of bare SiO_2, P3HT, and PMMA with M_n of 520,000 g/mol, M_w 350,000 g/mol, M_w 120,000 g/mol, and M_n 15,000 g/mol in these experiments.

Results

In order to study the impact of processing conditions on final film structure, the depth profile of the samples of interest were determined by neutron reflectivity experiments, where parameters of interest include polymer blend composition, spin casting speed, and PMMA molecular weight. Each experiment resulted in a raw neutron reflectivity curve which was fit to a multi-layer model using IGOR and Motofit software packages.[100] The model fit was verified for accuracy by incorporating a mass balance where the average scattering length density (SLD) for the model depth profile is compared to the average SLD of the polymer blend based on the composition of the spin cast solution within 3% agreement. The fitting procedure produces a depth profile of SLD as a function

of thickness. Each SLD is then transformed into a P3HT volume fraction depth profile using Equation 2.1:

$$\frac{SLD_{layer}(z)-SLD_{dPMMA}}{SLD_{dPMMA}-SLD_{P3HT}} = \phi_{P3HT}(z) \qquad \text{Equation (2.1)}$$

where $SLD_{layer}(z)$ is the SLD of the model depth profile at depth z, and ϕ_{P3HT} is the volume fraction of P3HT in the layer. The SLD of P3HT is estimated to be $0.7\text{x}10^{-6}\ A^{-2}$ and a range of $6.7\text{x}10^{-6}A^{-2}$ – $7.1\text{x}10^{-6}A^{-2}$ was used for the range of molecular weights of dPMMA, calculated from the National Institute for Standards and Technology (NIST) Center for Neutron Research (NCNR) SLD calculator. The thickness of each sample was normalized using the measured thicknesses from the neutron fit, where 0 is the air interface and 1 is the SiO_2 interface. The normalized film thickness allows the comparison of all films regardless of processing conditions where film thickness is known to change with polymer molecular weight and spin casting speed.[101]

Each P3HT volume fraction depth profile was further analyzed to quantitatively determine the extent of stratification of each sample. In this analysis, the stratification is quantified by comparing the depth profile of the experimental film to that of a completely stratified sample and a homogenous thin film. A completely stratified sample is defined as two layers of pure P3HT and pure dPMMA and a homogenous thin film is a film with a constant concentration of P3HT throughout the entire depth of the film.

We can compare the stratification of different samples regardless of processing conditions by utilizing a normalized thickness and the percent of P3HT in the samples as a baseline for each calculation. To determine the amount of P3HT in each sample, the total

integral of the volume fraction depth profile (0% to 100% P3HT) as a function of normalized thickness (0 to 1) is determined. This integral value is then used as the baseline in the depth profile for the extent of stratification calculation, because a completely homogenous (i.e. non-stratified) film contains this amount of P3HT, regardless of the probed depth. Equation 2.2 provides the method to calculate the extent of stratification, *S*, of a polymer blend film.

$$S = 100 * \frac{V_{sample}}{(100 - V_{total}) * (\frac{V_{total}}{100})} \quad \text{Equation (2.2)}$$

In Equation 2.2, V_{total} is the integral under a sample's depth profile curve (baseline 0% P3HT) which represents the volume percent of P3HT in the entire deposited film. The value obtained for V_{total} is used for the baseline of the integral denoted as V_{sample}. The value of the volume fraction of the P3HT in the film, V_{total}, is used as the baseline for V_{sample} ensuring that a homogenous, non-stratified sample is quantified as 0 percent stratified. Any area above the theoretical limit of a homogenous, non-stratified sample indicates stratification occurred. The integral denoted as V_{sample} represents a quantitative measure of the stratification of each sample. V_{sample} is the area under the depth profile of the experimental film with the average concentration of P3HT in the deposited film (that can be determined from V_{total}) as the baseline. For further clarification, this method is illustrated in Figure 2.1 for a sample consisting of a blend of P3HT:dPMMA 20:80. The horizontal dashed line at 20% P3HT describes the baseline of the V_{sample} integral, as the P3HT volume fraction of this sample is 20%. The vertical line at 0.2 thickness of the film represents the hypothetical thickness of a P3HT layer in a completely stratified film consisting of 20%

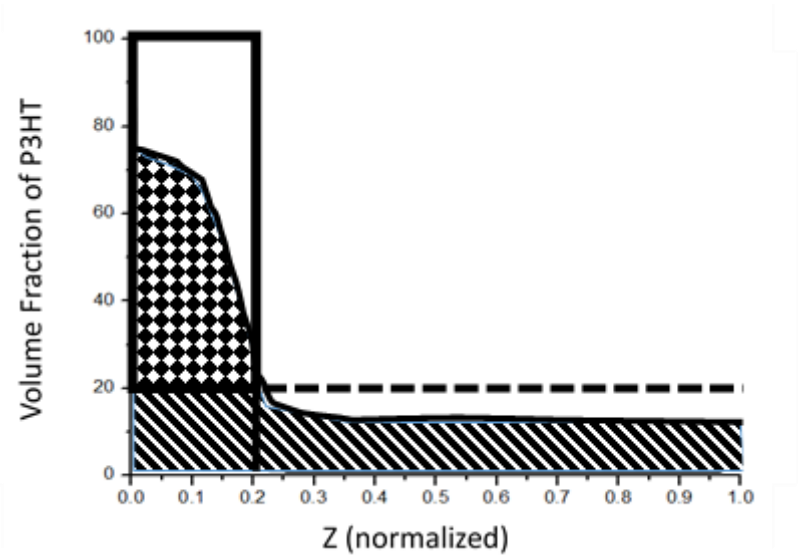


Figure 2.1 P3HT volume fraction depth profile illustrating the quantitative analysis of percent stratification, where V_{total} measures the sum of the areas of the black and white stripe region and the black and white checkerboard region, V_{sample} measures the area of the black and white checkerboard region, and the black horizontal baseline represents the baseline for V_{sample} which is equivalent to the concentration of P3HT in the sample.

P3HT. To calculate the extent of stratification of the sample, V_{sample} is divided by the area of a completely stratified layer with the horizontal baseline of 20 (volume percent of P3HT in the film) and the vertical thickness that is equal to the percent of P3HT in the film (0.2 in this case), as depicted by the vertical outlined rectangle in Figure 1. The area of the vertical rectangle above the horizontal baseline of V_{total} is calculated as the denominator in Equation 2.2 ($(100-V_{total})\bullet(V_{total}/100)$). The vertical and horizontal limits change in the calculation of *S* for each sample to account for changes in the P3HT composition in the film during the spin coating process. The extent of stratification for this sample is defined by the area under the depth profile curve and above the horizontal baseline (checkerboard pattern) (8), divided by the area of the outlined rectangle above the horizontal V_{total} baseline $(100-20)\bullet(20/100)=16$); 8/16= 50% stratified. The error for the extent of stratification is calculated from difference between the experimental volume percent of P3HT in the film (V_{total}) and the theoretical P3HT concentration based on the spin cast solution. The discrepancy between the experimental and theoretical P3HT concentrations is propagated through Equation 2.2.

Using this protocol, the extent of stratification of spin-coated P3HT:dPMMA polymer blends were monitored as a function of spin casting speed, P3HT:dPMMA blend composition and dPMMA molecular weight. First, the impact of P3HT:dPMMA blend composition will be reported. Figure 2.2 shows the resultant P3HT volume fraction depth profiles as a function of nominal blend composition. The compositions analyzed are P3HT:dPMMA blends of 5:95, 10:90, 15:85, 20:80. Altering the blend composition

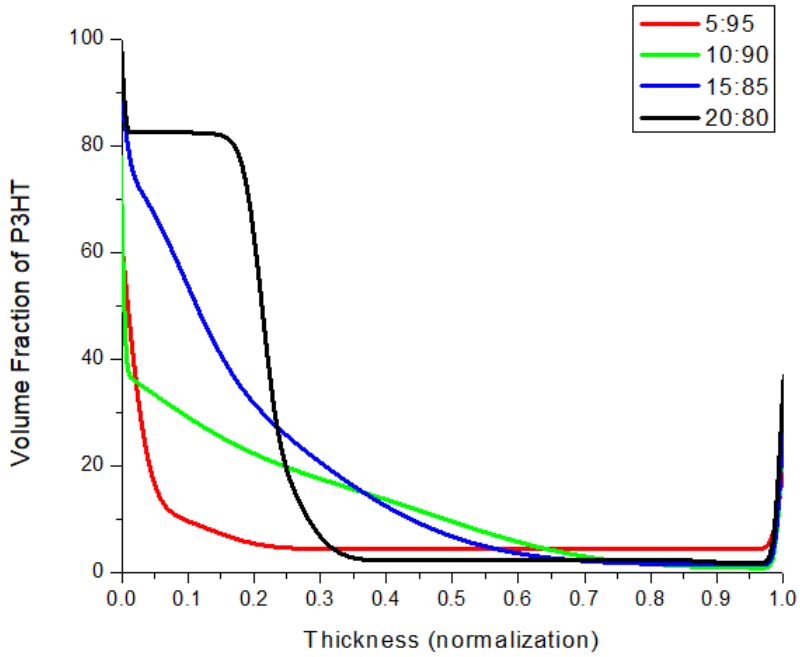


Figure 2.2 P3HT volume fraction depth profiles of P3HT:131,500 g/mol dPMMA 5:95 (red), 10:90 (green), 15:85 (blue), 20:80 (black) blends spin cast from chlorobenzene at 104.7 rad/s where 0 is the air interface and 1 is the SiO_2.

(Figure 2.2) clearly results in different degrees of P3HT found at the air interface, though all samples are stratified to some extent. As the P3HT concentration increases in these samples, the depth of the P3HT layer at the air interface broadens. In addition, the sharpness of the interface between an upper layer dominated by P3HT and the lower layer dominated by dPMMA varies for the blends. The breadth of the interface between these two layers is related in Figure 2 to the slope of the depth profile between layers, where a steep slope is interpreted to be a sharp interface while a gradual slope depicts a broad interface. The 5:95 P3HT:dPMMA sample has a broad interface that becomes sharper as the P3HT loading increases, with a significantly sharp interface observed in the 20:80 blend. Figure 2.3 plots the extent of stratification of the P3HT:131,500 g/mol dPMMA samples for all blend compositions. It is evident that an increase in P3HT loading increases the extent of stratification for each sample.

It has been previously reported that spin casting conditions directly impact film formation time.[97] One method to extend film formation time is to introduce a different spin casting solvent with a higher boiling point.[59] Changing the solvent allows us to investigate the effect of film formation time on the degree of stratification, but additional solvent-polymer interactions must be considered. As an attempt to isolate the effect of film formation time on the extent of stratification without introducing additional polymer-solvent interactions, the impact of spin-casting speed on film formation time, and thus, final film structure was monitored. To quantify the time required for film formation at each spin speed, time resolved light reflectivity experiments were conducted. Figure 2.4 presents

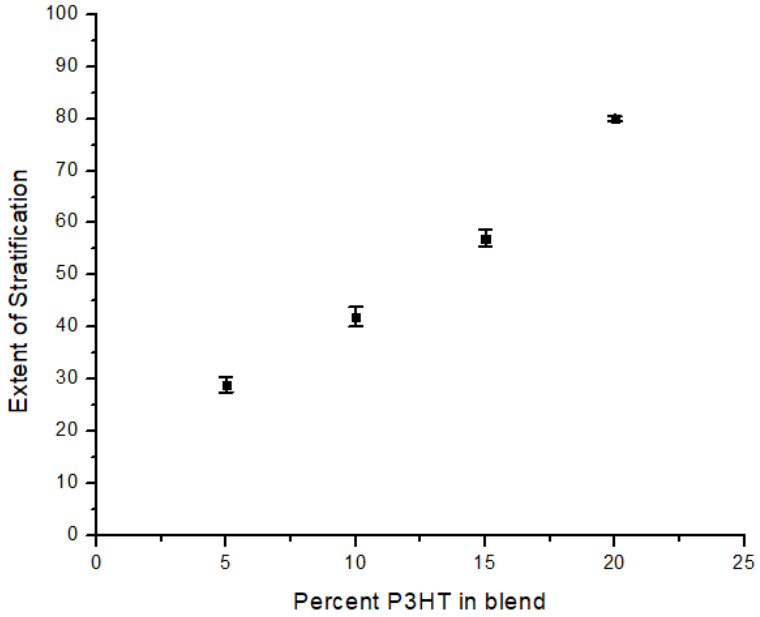


Figure 2.3 Plot of the extent of stratification as a function of P3HT loading all prepared at 104.7 rad/s and 131,500 g/mol dPMMA.

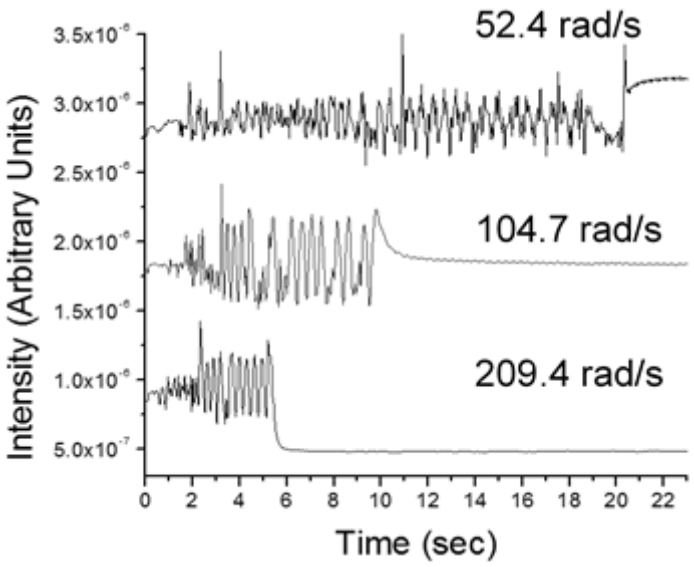


Figure 2.4 Light reflectivity monitoring film formation of a P3HT:dPMMA 20:80 blend spin cast at 52.4 rad/s (top), 104.7 rad/s (middle), and 209.4 rad/s (bottom).

the light reflectivity results for each spin speed (52.4, 104.7, 209.4 rad/s). Interpreting these results provides a film formation time when the constructive and destructive interference fridges no longer appear. This flat line is due to an increase in off specular scattering relative to the light reflectivity fringes in a dry film. These results show that P3HT:dPMMA blend solutions spun at 52.4 rad/s formed films in 21 seconds, solutions spun at 104.7 rad/s formed films in 11 seconds, and solutions spun at 209.4 rad/s formed films in 6 seconds.

The volume fraction depth profiles and extent of stratification for samples prepared with different casting speeds are reported in Figures 2.5 and 2.6, respectively. Figure 2.5 displays the P3HT volume fraction depth profile for the P3HT:dPMMA 20:80 blends containing 131,500 g/mol dPMMA as a function of spin cast speed. It is interesting to note that the sharpness of the interface between the P3HT dominated layer and dPMMA dominated layer does not change with spin cast speed. The change in spin cast speed, and therefore time of film formation, does alter the concentration of P3HT in the top layer, though it does not change the normalized thickness of this layer. In these samples, the 52.4 rad/s sample contains the highest concentration of P3HT in the top layer, while the 209.4 rad/s sample contains the smallest concentration of P3HT in the top layer. It is important to note that although this representation of the data does not show a broadening of the P3HT layer with spin speed, each sample's thickness has been normalized to 1. Therefore, the P3HT rich layer is thicker in the sample cast at 52.4 rad/s (~19 nm) than the sample cast at 209.4 rad/s (~4 nm), but this difference is minimalized when the total thickness of the film is normalized. The total thicknesses of the 52.4 rad/s and 209.4 rad/s films are

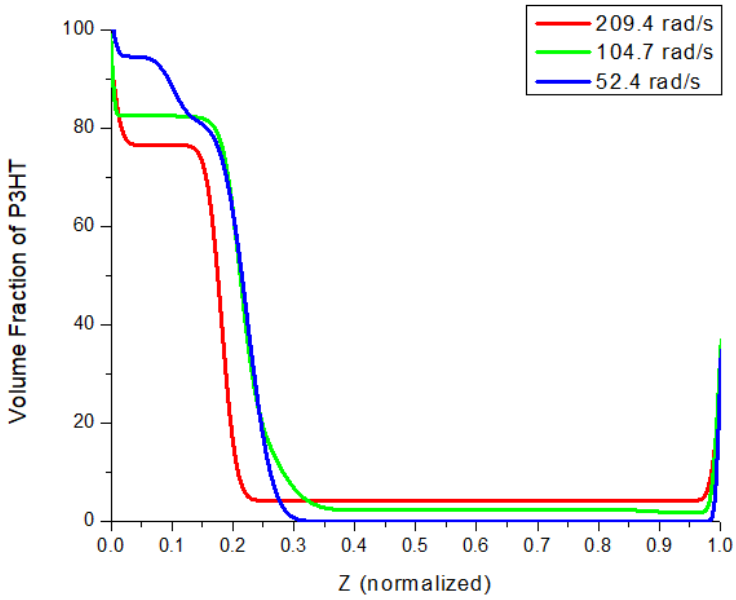


Figure 2.5 P3HT volume fraction depth profiles of a P3HT:dPMMA (131,500 g/mol) 20:80 blend spin cast from chlorobenzene at 209.4 rad/s (red), 104.7 rad/s (green), and 52.4 rad/s (blue) where 0 is the air interface and 1 is the SiO_2. Repeats of P3HT:dPMMA (131,500 g/mol) 20:80 samples prepared at 104.7 rad/s and 209.4 rad/s are included in the appendix.

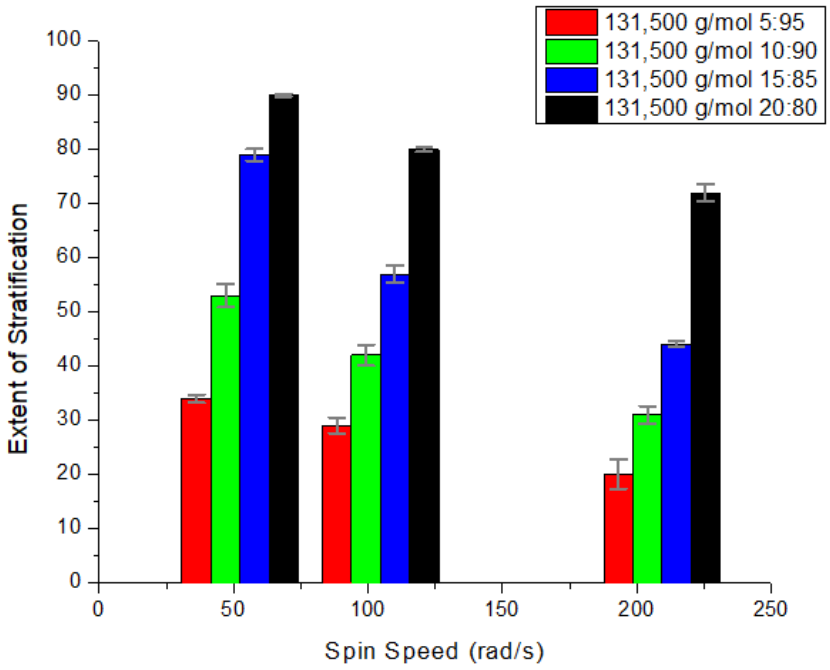


Figure 2.6 Plot of extent of stratification as a function of spin speed, and P3HT:dPMMA composition 5:95 (red), 10:90 (green), 15:85 (blue), 20:80 (black). The P3HT volume fraction profiles for P3HT:dPMMA 131,500 g/mol samples of all blend compositions prepared at casting speeds of 52.4 and 209.4 rad/s can be found in the appendix. Additionally, repeats of P3HT:dPMMA (131,500 g/mol) 5:95 samples prepared at 52.4 rad/s and 104.7 rad/s are included in the appendix.

~65 nm and ~30 nm, respectively.

To quantify the exact changes of the stratification with the change in processing conditions, the P3HT volume fractions were analyzed to quantify the extent of stratification with the method described by Equation 2.2. Figure 2.6 shows the extent of stratification as a function of the composition of the P3HT:dPMMA blend as well as the spin-casting speed for each thin film. Figure 2.6 also shows that at each specific spin speed, an increase in P3HT loading results in a larger percent stratification. In addition, Figure 2.6 also shows that for each P3HT:dPMMA composition, a spin speed of 52.4 rad/s results in the largest extent of stratification. Qualitatively, the stratification of the final film increases with decreasing spin speed and increasing film formation time.

The molecular weight of dPMMA was also varied to observe its effect on the P3HT stratification process. For this set of experiments, four different dPMMA molecular weights were employed (20,000 g/mol, 131,500 g/mol, 316,000 g/mol, and 520,000 g/mol). Films were formed from solutions with P3HT:dPMMA compositions of 5:95, 10:90, 15:85, 20:80, where solutions were spin cast at 104.7 rad/s from chlorobenzene. Figure 2.7 shows the P3HT volume fraction depth profiles for the 5:95 P3HT:dPMMA blends for each molecular weight.

The film formed from the blend containing the largest molecular weight dPMMA 520,000 g/mol has a small layer of highly concentrated P3HT at the air surface, and as the molecular weight of dPMMA decreases, the P3HT concentration at the air interface decreases. The interface between the P3HT dominated region and the dPMMA dominated

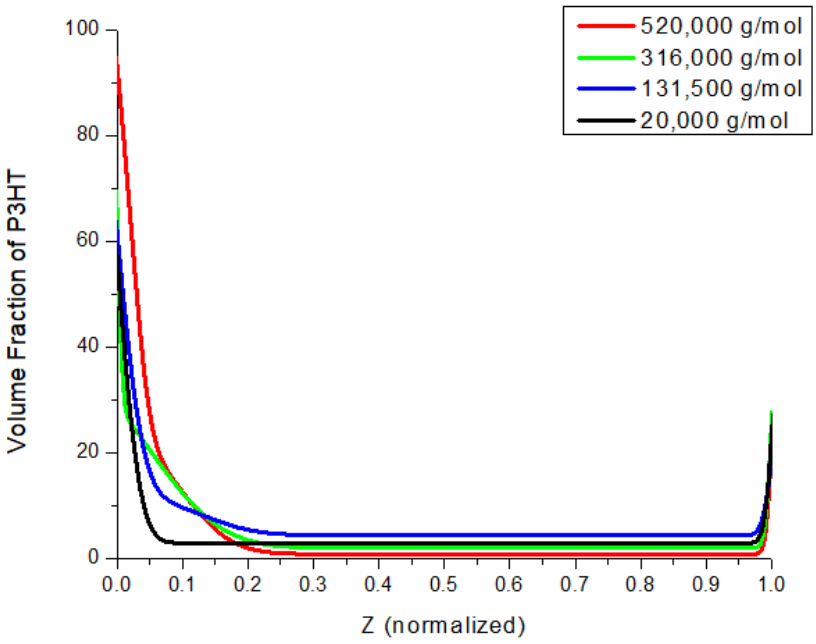


Figure 2.7 P3HT volume fraction depth profiles of a P3HT:dPMMA 5:95 blend spin cast from chlorobenzene at 104.7 rad/s with varying dPMMA molecular weights 520,000 g/mol (red), 316,000 g/mol (green), 131,500 g/mol (blue), 20,000 g/mol (black) where 0 is the air interface and 1 is the SiO_2 interface.

region does not seem to change significantly among the various molecular weight depth profiles. To quantify the effects of dPMMA molecular weight on stratification, each depth profile was analyzed using Equation 2.2, and the resultant extents of stratification are shown in Figure 2.8.

Inspection of Figure 2.8 shows that for each blend composition, the extent of stratification generally decreases as dPMMA molecular weight decreases. It is important to note that the change in extent of stratification with respect to blend composition in these experiments, where an increase in P3HT in the blend leads to an increase in stratification, agrees with the trends observed in the stratification patterns and extent of stratification values shown in Figures 2.2, 2.3, and 2.6. Additionally, the change in extent of stratification with blend composition is significantly reduced in the 520,000 g/mol dPMMA blend relative to the changes in the extent of stratification with blend composition for films that contain 20,000 g/mol dPMMA. The blends containing 520,000 g/mol dPMMA exhibit a variation in extent of stratification that is only *ca*. 15% with blend composition, while the extent of stratification in the 20,000 g/mol dPMMA blends varies from less than 10% to greater than 60% with changes in the blend composition.

To further investigate the driving forces behind stratification differences when varying dPMMA molecular weight, contact angle measurements were conducted using water and di-iodomethane to determine the surface energy of each molecular weight dPMMA, P3HT, and SiO_2. The contact angle measurements as well as their respective surface energies are presented in Table 2.1. Surface energy was calculated using the

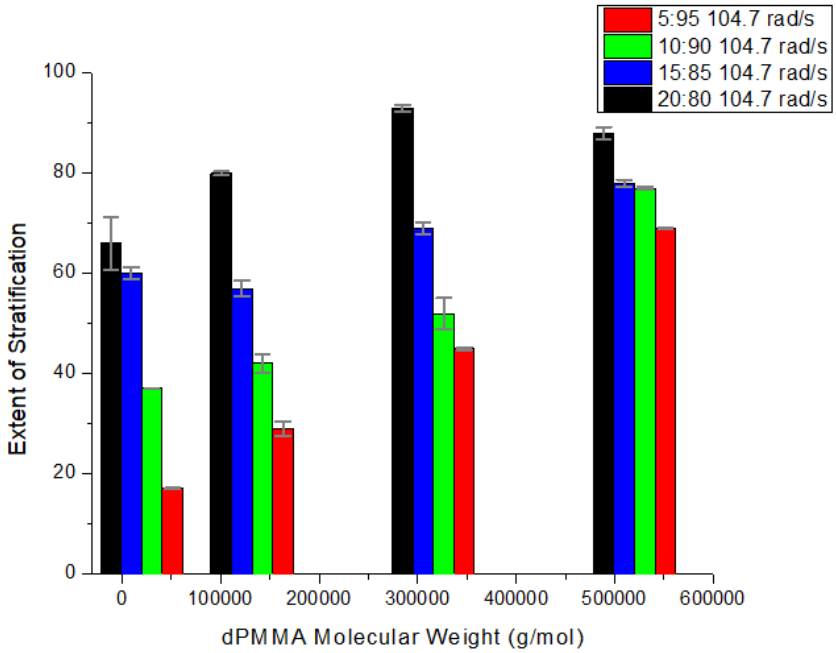


Figure 2.8 Plot of the extent of stratification as a function of dPMMA molecular weight and P3HT:dPMMA composition 5:95 (red), 10:90 (green), 15:85 (blue), 20:80 (black) all prepared at 104.7 rad/s. The P3HT volume fraction profiles for P3HT:dPMMA 20,000 g/mol, 316,000 g/mol, and 520,000 g/mol samples can be found in the appendix.

geometric mean method as shown in Equation 2.3:[102]

$$(1 + \cos \theta_t)\gamma_t = 2[(\gamma^d_t \gamma^d_s)^{1/2} + (\gamma_t^p \gamma_s^p)^{1/2}] \quad \text{Equation (2.3)}$$

In Equation 2.3, θ is the contact angle of the test liquid on a solid surface, and γ_t and γ_s are the surface energies of the test liquid and the solid surface, respectively. The accepted polar (p) and dispersive energy (d) components for water are 51.0 mJ/m^2 and 21.8 mJ/m^2 and for diiodomethane are 0.0 mJ/m^2 and 50.8 mJ/m^2.[38] The surface energy of PMMA increases with decreasing molecular weight, and the surface energy of PMMA is always larger than that of P3HT. P3HT and all molecular weights of PMMA have significantly different surface energies than that of the SiO_2 substrate. The decrease in the surface energy of dPMMA with molecular weight is accredited to an end group effect, where an increase in the number of chain ends in low molecular weight polymers relative to their high molecular weight counterparts alters the polymer surface energy.

Discussion

The data presented here documents and quantifies the impact of altering the processing conditions of spin coating immiscible polymer blends on the final film depth profile, including spin speed, polymer blend composition, and polymer molecular weight. Altering each of these parameters individually resulted in varying depth profiles and extent of stratification, yet the driving forces for these changes are less clear. Clearly, a number of factors may contribute to the stratification of a polymer blend during spin coating, including surface energy differences between two polymers,[103] the miscibility of the two

Table 2.1 Contact angles and calculated surface energies and measurements of the polymers studied.

Sample	H_2O Contact Angle (°)	CH_2I_2 Contact Angle (°)	Surface Energy (mJ/m^2)
15,000 g/mol PMMA	74.5	32.4	46.5
100,000 g/mol PMMA	73.0	32.5	47.0
350,000 g/mol PMMA	70.5	31.9	48.1
520,000 g/mol PMMA	67.4	32.1	49.2
P3HT	92.9	54.7	32.3
SiO_2	18.7	43.4	71.1

polymers, the relative solubility of each component in the pre-deposition solvent, the film formation time, and surface energy of the supporting substrate. It is clear that the surface energy differences between the two polymers does not fully explain our results, particularly the change in stratification with blend composition (Figure 2.2). To further investigate the importance of these driving forces of stratification, the Flory-Huggins interaction parameters, χ, between PMMA, P3HT, and chlorobenzene were estimated using Equation 4.[104] The literature solubility parameters, δ, for P3HT and PMMA are presented in Table 2 as well as the calculated χ parameter between P3HT and PMMA (χ = 1.08) using Equation 2.4.

$$\chi = \frac{V_0}{RT}(\delta_a - \delta_b)^2 \qquad \text{Equation (2.4)}$$

A χ parameter that is greater than 0.5 indicates poor polymer-polymer interactions, and an immiscible blend.[105] This is consistent with the results presented in Figure 2.2 that shows there is an increase of P3HT at the air interface with increase of P3HT loading in the blend, as this is consistent with increased phase separation between the two polymers and increased stratification as P3HT concentration in the blend increases, as shown in Figure 2.3. The increased immiscibility with increased P3HT concentration in the blend manifests as an increase in the P3HT concentration at the air interface. This result indicates that the immiscibility of P3HT and PMMA is a significant driving force for this stratification and that increasing the miscibility of two polymers will decrease the stratification.

The in-situ light reflectivity results (Figure 2.4) show that spin coating at 209.4 rad/s traps polymer movement over three times faster than the film formation process that occurs at the slowest spin speed of 52.4 rad/s. Since all other process conditions (blend composition, solvent interactions, blend molecular weight) are left unchanged, the kinetics of the film formation process are exclusively responsible for the disparity among all samples' final film depth profiles in Figure 2.5. Assuming the blend continually rearranges during the film formation process and is driven towards an equilibrium structure, the regulation of film formation time provides insight into the progress towards equilibrium of each blend's thin film. For instance, a sample fabricated with a fast spin speed and shorter film formation time has a depth profile further from equilibrium than a sample processed with slower spin speed and longer film formation time. The P3HT volume fraction depth profiles for the films formed from P3HT:131,500 g/mol dPMMA 20:80 blends (Figure 2.4) shows that P3HT segregates to the air surface (Z=0) for all three spin speeds with an increased P3HT concentration at the air interface with decreasing spin speed. Thus, the slower spin speed provides more time for the P3HT to be thermodynamically driven to the air interface, which is consistent with its lower surface energy. Figure 2.6 quantifies the percent stratification as a function of spin speed, where for each blend composition of P3HT and 131,500 g/mol dPMMA, the percent stratification increases with decreasing spin speed. This result indicates that the equilibrium of a P3HT:131,500 g/mol dPMMA blend is a more stratified sample with a P3HT dominated layer found at the air interface and a dPMMA rich layer found at the Si interface. Further, the effect of altering the

Table 2.2 Solubility parameters at room temperature for P3HT and PMMA.

Material	δ (MPa$^{1/2}$)	$\chi_{P3HT-PMMA}$
P3HT	14.8[106]	1.08
PMMA	19.5[107]	

P3HT:dPMMA blend composition is also evident at each examined spin speed (Figure 2.6), where increasing the P3HT concentration in the blend also increases the extent of stratification.

To broaden our understanding of the driving forces behind stratification of this system, PMMA molecular weights ranging from 20,000 g/mol – 520,000 g/mol were combined with P3HT in blend compositions of 5:95-20:80 and spin cast at 104.7 rad/s to investigate the effect of PMMA molecular weight on the film stratification patterns and extent of stratification. Altering the relative molecular weights of the two polymers in the blend allows us to evaluate the importance of entropic contributions to the stratification of the components in the film during the casting process. This is because smaller chains are entropically driven to the air interface to minimize the entropic penalty of confining a long polymer chain to an impenetrable interface.[108,109] Figures 2.7 and 2.8 present the depth profiles and the extent of stratification of the cast films as a function of dPMMA molecular weight and P3HT:dPMMA blend composition, respectively. Figure 2.8 clearly shows that increasing the P3HT concentration in the blend, regardless of dPMMA molecular weight, increases the extent of stratification which is consistent with previously discussed results. The P3HT volume fraction depth profile for blends of 5:95 P3HT:dPMMA with varying dPMMA molecular weight, as seen in Figure 2.7, shows various amounts of P3HT driven towards the air interface depending on the molecular weight of dPMMA. This result is quantified in Figure 2.7, where stratification decreases with decreasing dPMMA molecular weight, for all four blend compositions. This is consistent with an increase in importance

of entropic forces with the introduction of lower molecular weight dPMMA. A reduction of the free energy of the system provides a driving force for the low molecular weight dPMMA to entropically segregate to the air interface, challenging the enthalpically driven sequestration of the P3HT at the air interface. This competition leads to less stratification due to the failure for P3HT and dPMMA to form independent pure layers.

All of the extent of stratification results are in good agreement with the calculated surface energies where the P3HT is primarily driven to the air interface and the decrease in dPMMA molecular weight results in a lower surface energy material, such that it is approaching the surface energy of P3HT. It is important to emphasize that the similarity of surface energy and entropic forces in the 20,000 g/mol dPMMA samples lead to less stratified films, while increasing the loading of P3HT in the blend still elicits an additional driving force for stratification. This result indicates that the entropic forces due to varying dPMMA molecular weight are not sufficient to overcome the immiscibility of the two polymers, P3HT and dPMMA.

These results clearly indicate that all processing conditions, not solely the miscibility of the polymer blend or their surface energies dictate and drive final film morphology, depth profiles, and extent of stratification. It is evident that by simply altering processing conditions, a targeted final film morphology may be fabricated without additional post-processing modifications. Although P3HT:dPMMA blends were studied here, the guidelines produced are based on the thermodynamic driving forces and kinetics of film formation during spin casting. Therefore, these results should provide guidelines to

direct the stratification and assembly of a broad range of polymer blends. This foundation thus provides pathways to improve the structure and assembly of thin polymer blend films for a myriad of applications. These range from durable polymer coatings to organic electronic device processing where these results show that the interface between the polymers can be controlled without extensive alteration to the thin film itself, as well as controllably altering the extent of stratification by changing the processing conditions.

Conclusion

Neutron reflectivity experiments provide film depth profiles of various spin cast polymer blends processed by varying spin speed, blend composition, and polymer molecular weight. These results indicate that spin speed, blend composition, and molecular weight alter the stratification patterns of P3HT and dPMMA polymer blends and provide insight into the fundamental driving forces that guide the stratification process. In all cases, P3HT is driven toward the air interface and changing the processing conditions can further encourage this effect. This research also develops a method to analyze the degree of stratification, and therefore quantitatively compare the impact of processing parameters on the stratification process.

Our results show that the speed of spin casting controls film formation time where a slower spin speed leads to longer film formation. This longer film formation time allows the polymer layers more time to rearrange and approach equilibrium. By utilizing slower spin speeds, more stratified P3HT:dPMMA thin films emerge, when compared to samples formed at faster spinning speeds. In addition, altering the blend composition and molecular

weight of the polymers also influence the final film depth profile. As the concentration of P3HT in the blend increases, the stratification of the blend increases due to the decrease in miscibility of the blend. Not only does the stratification increase, but increasing the amount of P3HT in the blend also elicits a sharpened interface between the two layers.

Incorporating lower molecular weight dPMMA into the blend alters the entropic driving forces in the stratification process, due to the increase in number of chain ends. This lower molecular weight dPMMA is entropically driven towards the air interface competing with P3HT, therefore decreasing stratification. These results therefore provide guidelines to control and moderate the final film morphology and layering of deposited polymer blend thin films. Since P3HT and PMMA are widely used for organic field effect transistors, this research ultimately expands our ability to controllably alter the final film structure, and creates a pathway to better understand the correlation between processing conditions and thin film structure required for efficient device performance. Although this study outlines P3HT:dPMMA blends, the overall conclusions can be applied to other polymer blend systems and provides crucial insight that can direct the development of optimal cost-efficient methods to fabricate multi-layer films with the desired structure without the need for post-modification processes.

Acknowledgements

The authors gratefully acknowledge the National Science Foundation (DMR-1409034 and DMR-1808946) for support of this project. We acknowledge the support of

the National Institute of Standards and Technology, U.S. Department of Commerce, in providing the neutron research facilities used in this work.

Certain commercial equipment, instruments, or materials (or suppliers, or software) are identified in this paper to foster understanding. Such identification does not imply recommendation or endorsement by the National Institute of Standards and Technology, nor does it imply that the materials or equipment identified are necessarily the best available for the purpose.

Appendix

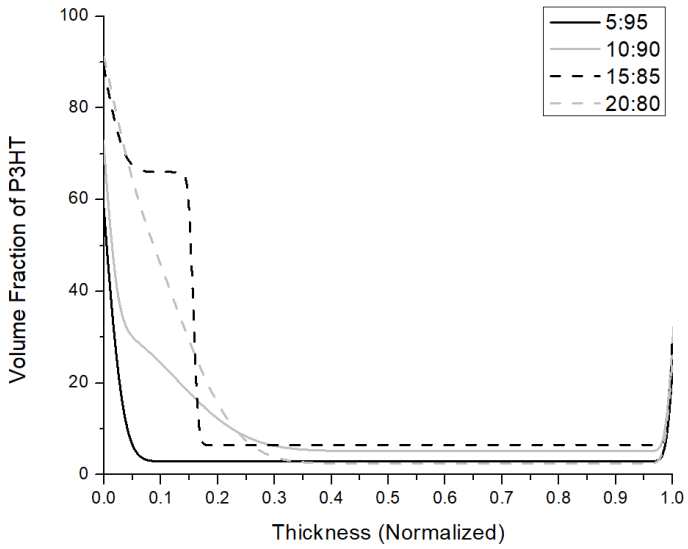


Figure 2.9 P3HT volume fraction depth profiles of P3HT:20,000 g/mol dPMMA 5:95 (black solid line), 10:90 (grey solid line), 15:85 (black dashed line), 20:80 (grey dashed line) blends spin cast from chlorobenzene at 104.7 rad/s where 0 is the air interface and 1 is the SiO_2.

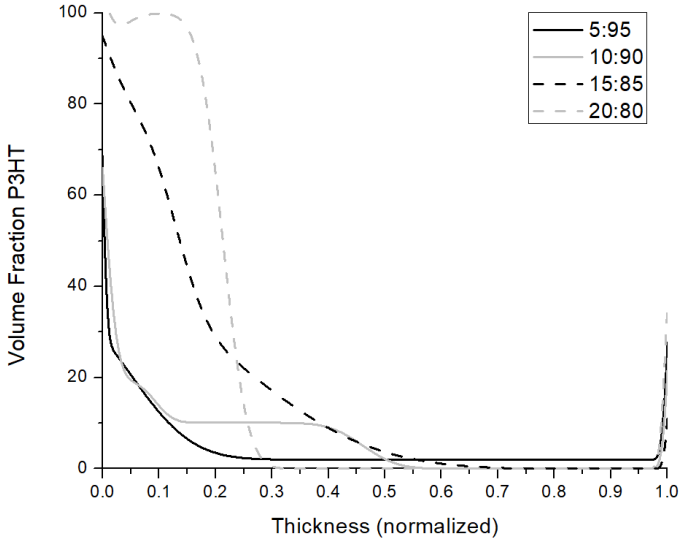


Figure 2.10 P3HT volume fraction depth profiles of P3HT:316,000 g/mol dPMMA 5:95 (black solid line), 10:90 (grey solid line), 15:85 (black dashed line), 20:80 (grey dashed line) blends spin cast from chlorobenzene at 104.7 rad/s where 0 is the air interface and 1 is the SiO_2.

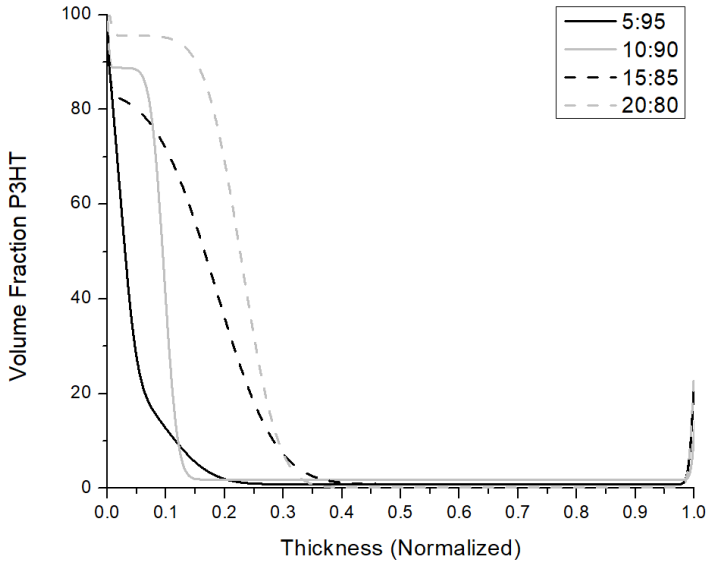


Figure 2.11 P3HT volume fraction depth profiles of P3HT:520,000 g/mol dPMMA 5:95 (black solid line), 10:90 (grey solid line), 15:85 (black dashed line), 20:80 (grey dashed line) blends spin cast from chlorobenzene at 104.7 rad/s where 0 is the air interface and 1 is the SiO_2.

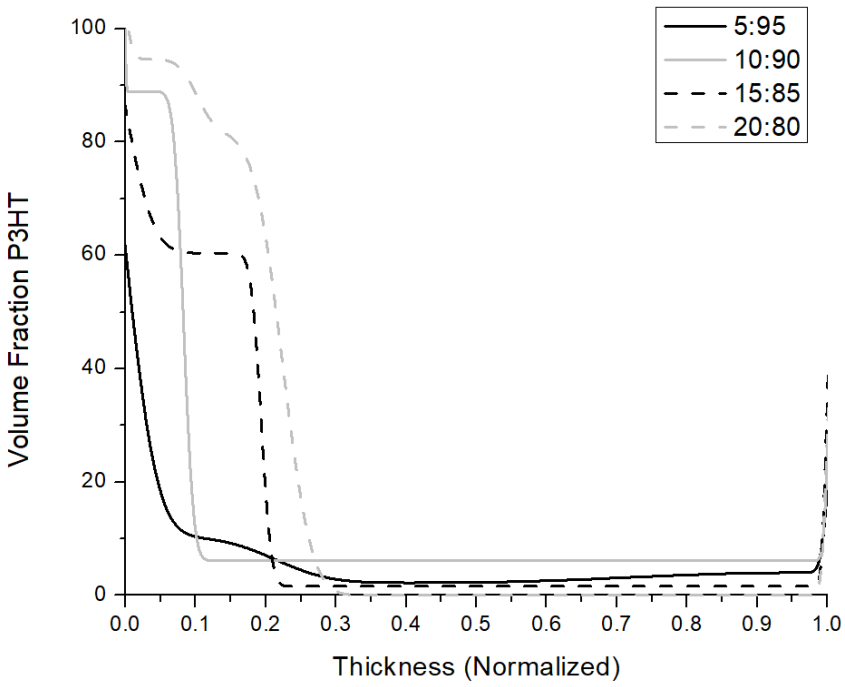


Figure 2.12 P3HT volume fraction depth profiles of P3HT:131,500 g/mol dPMMA 5:95 (black solid line), 10:90 (grey solid line), 15:85 (black dashed line), 20:80 (grey dashed line) blends spin cast from chlorobenzene at 52.4 rad/s where 0 is the air interface and 1 is the SiO_2.

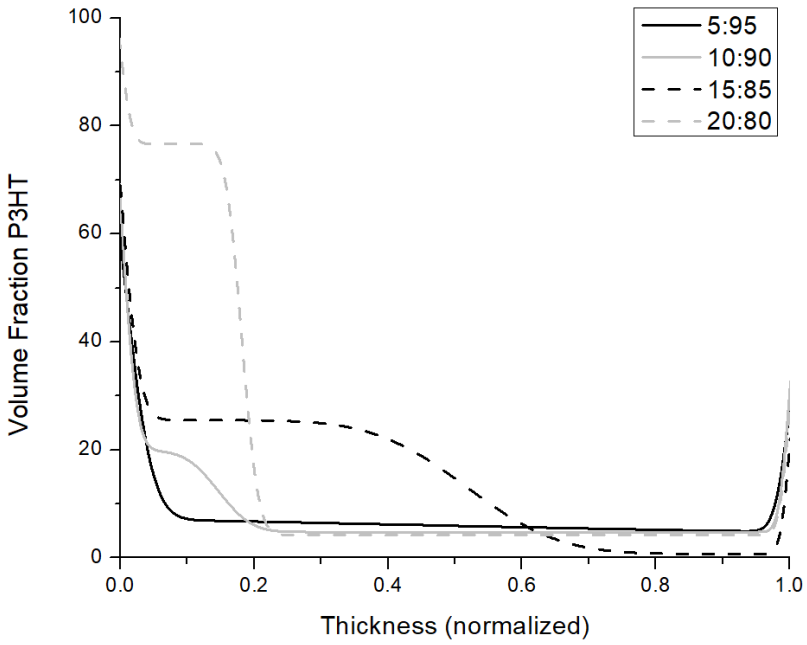


Figure 2.13 P3HT volume fraction depth profiles of P3HT:131,500 g/mol dPMMA 5:95 (black solid line), 10:90 (grey solid line), 15:85 (black dashed line), 20:80 (grey dashed line) blends spin cast from chlorobenzene at 209.4 rad/s where 0 is the air interface and 1 is the SiO_2.

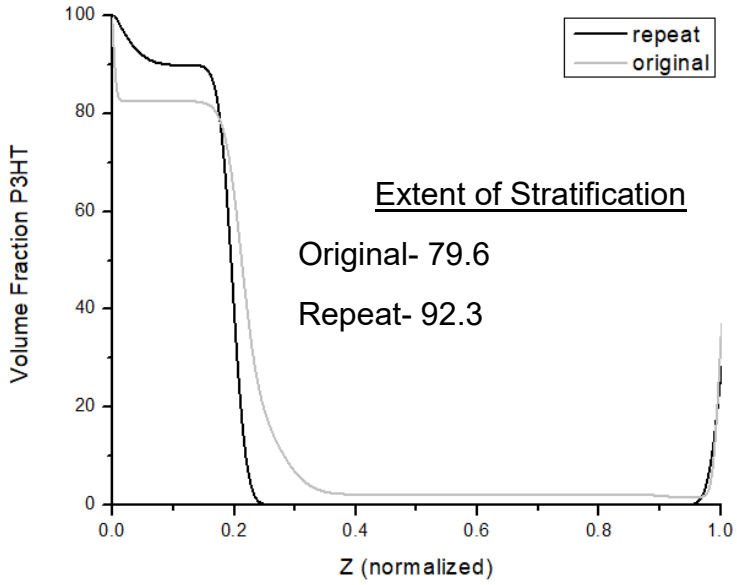


Figure 2.14 The original (grey solid line) and repeat (black solid line) P3HT volume fraction depth profiles of P3HT:131,500 g/mol dPMMA 20:80 prepared at 104.7 rad/s from chlorobenzene where 0 is the air interface and 1 is the SiO_2.

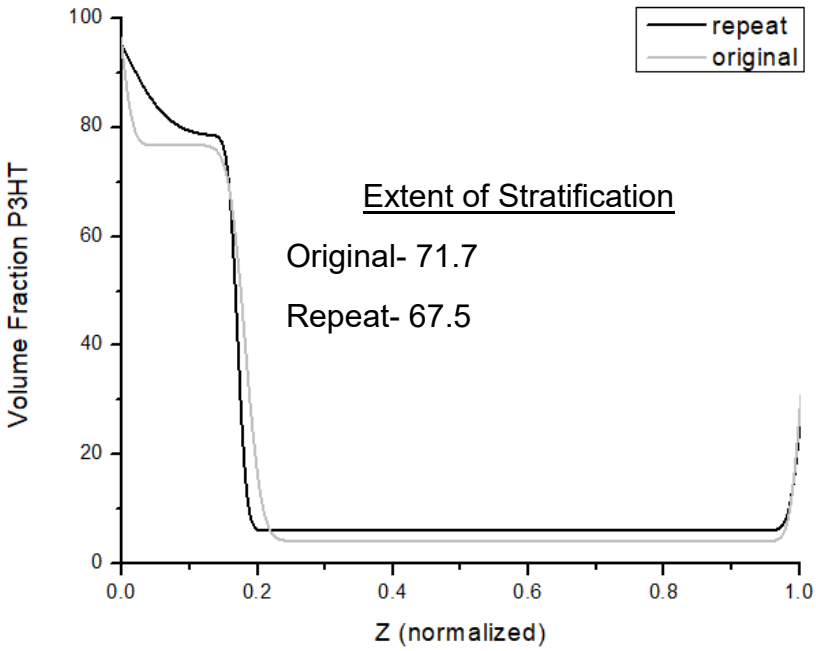


Figure 2.15 The original (grey solid line) and repeat (black solid line) P3HT volume fraction depth profiles of P3HT:131,500 g/mol dPMMA 20:80 prepared at 209.4 rad/s from chlorobenzene where 0 is the air interface and 1 is the SiO2.

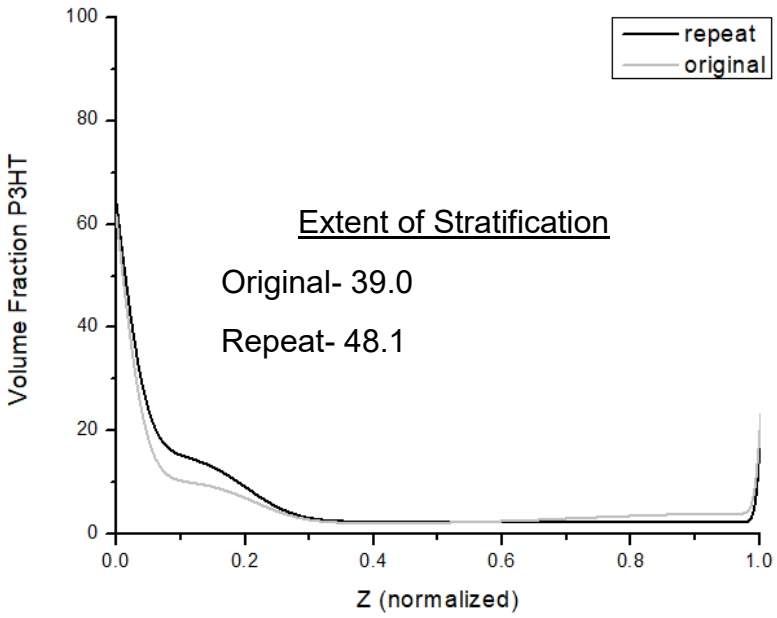


Figure 2.16 The original (grey solid line) and repeat (black solid line) P3HT volume fraction depth profiles of P3HT:131,500 g/mol dPMMA 5:95 prepared at 52.4 rad/s from chlorobenzene where 0 is the air interface and 1 is the SiO2.

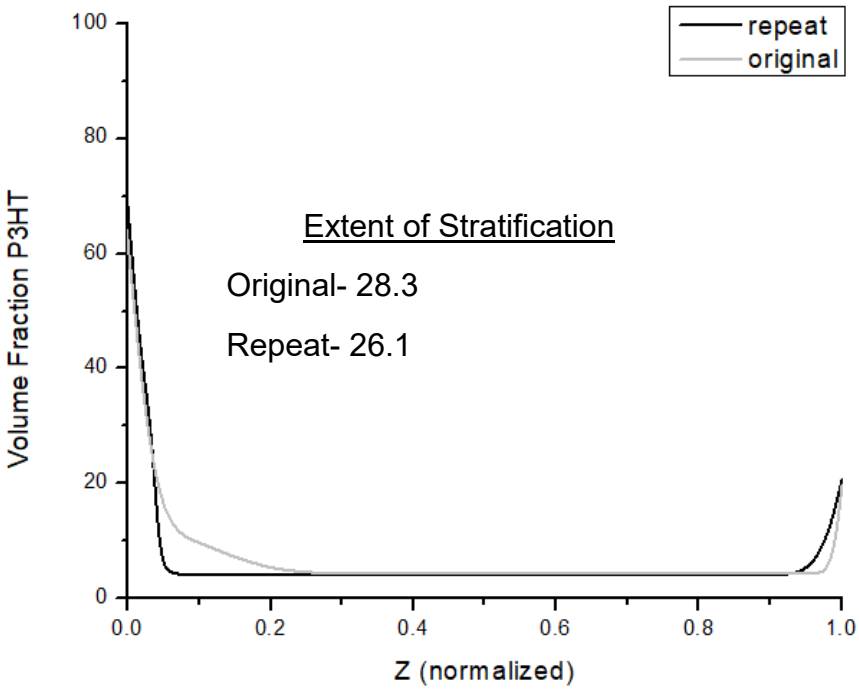


Figure 2.17 The original (grey solid line) and repeat (black solid line) P3HT volume fraction depth profiles of P3HT:131,500 g/mol dPMMA 5:95 prepared at 104.7 rad/s from chlorobenzene where 0 is the air interface and 1 is the SiO2.

CHAPTER THREE THE INTERPLAY OF THERMODYNAMICS AND KINETICS: IMPARTING HIERARCHICAL CONTROL OVER FILM FORMATION OF SELF-STRATIFIED BLENDS

Abstract

Spin casting has become an attractive method to fabricate polymer thin films found in organic electronic devices such as field-effect transistors, and light emitting diodes. Many studies have shown that altering spin casting parameters such as casting solvent and speed can improve device performance. Additionally, device performance has been directly correlated to the degree of polymer alignment, crystallinity, and morphology of the thin film. Our recent results investigate the impact of casting speed and molecular weight on the stratification of thin polymer blend films where surface energy and polymer-polymer miscibility are defined as controlling parameters. To provide a more complete understanding of the balance of thermodynamic and kinetic factors that influence the stratification of polymer blend thin films, we monitor stratified polymer blend thin films developed from the polymer blend of poly(3-hexylthiophene-2,5-diyl) and poly(methyl methacrylate) at controlled loading ratios, relative molecular weights, and casting speed. The structures of these thin films were characterized via neutron reflectivity, and the results show that at the fastest casting speed, polymer-polymer interactions and surface energy of the polymers in the blend dictates final film structure, and at the slowest casting speed, there is less control over the film layering due to the polymer-polymer interactions, surface energy, and entropy simultaneously driving stratification, and different from the fastest two casting speeds, the relative solubility limits also play a role in the stratification process. The relative solubility limits gain relevance at the slowest casting speed due to the reduced evaporation rate of the solvent and increased drying time of the film increasing the time

between polymer precipitation and final film formation. These results broaden the current understanding of the relationship between spin casting conditions and vertical phase separation in polymer blend thin films. This knowledge provides a foundation for improved rational design of polymer thin film fabrication processes to attain targeted stratification, and thus performance.

Introduction

Spin casting has been used for multiple decades as a method to fabricate thin films that are as large as 50 microns to as thin as a few nanometers.[110] It is well known that casting speed, solution loading, and polymer molecular weight have an effect on final film thickness.[111–113] Spin casting became an attractive deposition method for the fabrication of films for many applications ranging from organic electronic devices to a variety of polymer coatings.[114–116] Specifically in the device fabrication field, careful modification of the spin casting processing parameters such as solvent, casting speed, and polymer loading elicit various qualitative trends in polymer gelation, crystallization, and chain alignment.[81,95,117–120]

Recently, devices with improved performance and durability have been realized by fabricating from solution of polymer blends.[76,121–123] Typically each polymer in the blend is soluble in a common solvent which allows for one-step solution processing, streamlining the fabrication process.[76,121] Additionally, polymer blends open the possibility of auto-assembly or self-stratification into useful structures with practical interfaces for organic electronics.[73,94,124] As with spin casting single polymer solutions, the morphology of a

polymer blend final film is dictated by the deposition conditions. However, the relationship between spin casting conditions and structure formation in the fabricated film becomes more complex with the addition of another polymer.[38,55,80] The concurrent and competing interactions between the two polymers, between polymers and solvent, and between polymers and substrate result in a complex process where it is difficult to anticipate and predict the final film structure.[62] This limits the ability to rationally alter the spin casting processing conditions to design the final device structure to a targeted morphology, which is detrimental to improving device performance by directing final film architecture.[66]

The various binary interactions present in the deposition process of polymer blend films are known, yet the importance of each interaction in the deposition process and its contribution towards final film structure is less understood.[66] Self-stratification is a term used to encompass the vertical phase separation of polymer blends in thin films and is widely accepted as a thermodynamically driven process despite intrinsic kinetic trapping effects.[125] Kinetic trapping occurs during the short time scales of spin-cast film formation and prevents the blend solution from reaching its equilibrium. Many studies have demonstrated varying device performance with a change in casting solvent.[81,95,117,126] However, the variation in device performance is often attributed to polymer-solvent or specific surface energy interactions yet the impact of solvent evaporation rate and kinetics of film formation are often overlooked.

To address these shortcomings, our group has studied the dominating driving forces of film formation and stratification of poly(3-hexylthiophene-2,5-diyl) (P3HT) and

poly(methyl methacrylate) (PMMA) blends by monitoring the final film structure as a function of processing conditions, including casting speed, blend composition, and polymer molecular weight.[127] These experiments reveal that as polymer molecular weight and blend composition were altered, thermodynamic interactions such as polymer surface energy, and the polymer-polymer interaction parameter controlled final film stratification. Additionally, the kinetic and thermodynamic effects on final film structure were decoupled by controlling casting speed to vary film formation time, rather than introducing a more slowly drying solvent, which would also alter the thermodynamic interactions of the system. By keeping all thermodynamic parameters constant, the kinetic effects on final film structure are isolated. These results showed that the longer film formation time of slower casting speed resulted in larger extents of stratification relative to the samples prepared at fast casting speeds. We attribute this increased layering to the fact that the fully stratified film is the thermodynamic endpoint, and longer film formation time allows the film to evolve closer towards this equilibrium.

The work describe here expands the solution and casting parameters including blend composition, polymer molecular weight, and casting speed, to gain an increased understanding of the impact of each thermodynamic parameter on the stratification process, and provide a foundation that can aid in the development of guidelines to rationally design and tune the stratification in polymer blend films simply by altering pre-deposition solution properties and processing conditions.

Experimental

Chlorobenzene (Sigma Aldrich), Poly(3-hexylthiophene-2,5-diyl) (P3HT) (Ossila, regioregularity-95%, and number-average molecular weight (M_n) 19,500 g/mol and polydispersity index (PDI) 1.75) and deuterated poly(methyl methacrylate (dPMMA) (Polymer Source Inc., M_n (PDI), 20,000 g/mol (1.6), 131,500 g/mol (1.4), 316,000 g/mol (1.35), 520,000 g/mol (1.4)) were used directly from the supplier and were not further purified. Polymer blends were dissolved at 1 percent by weight in ratios of P3HT:dPMMA 5:95, 10:90, 15:85, 20:80 in chlorobenzene at 55°C overnight. Thin films were prepared by spin coating (209.4 rad/s or 52.4 rad/s) the chlorobenzene solutions onto Si wafers. The Si wafers were cleaned in a piranha solution (1:3 ratio of sulfuric acid and hydrogen peroxide), washed with nanopure water, and placed under UV irradiation and ozone.

Neutron reflectivity experiments were conducted at the National Institute of Standards and Technology's Center for Neutron Research (NCNR) using the NG7 beamline with a Q range of 0.008-0.2 A^{-1} where $Q= 4\pi/\lambda \sin(\theta)$; λ is the neutron wavelength, and θ is the angle of incidence. The data for all incident angles was reduced utilizing the NCNR software.

The solubility limits of protonated poly(methyl methacrylate) (H-PMMA) in chlorobenzene were determined using transmission infrared spectroscopy (IR). H-PMMA was obtained from Acros (M_n 15,000 g/mol), Sigma-Aldrich (weight average molecular weight (M_w) 120,000 g/mol and 350,000 g/mol), and M_n 520,000 g/mol dPMMA was obtained from Polymer Source. IR spectra were recorded with a Thermo Scientific Nicolet

iS50 FTIR Spectrometer and a transmission cell. The solubility limits for H-PMMA and dPMMA were determined by monitoring the intensity of the carbonyl peak (1730 cm^{-1}) (A) combined with the Beer-Lambert law (Equation 3.1) where c is the concentration of the solution, ε is the molar absorptivity, and l is the path-length.

$$A = c\varepsilon l \qquad \text{Equation (3.1)}$$

The molar absorptivity was determined by measuring the intensity of the carbonyl peak for each molecular weight of H-PMMA and dPMMA at known concentrations and plotted as a function of PMMA concentration. The slope of the line from each of these graphs is the molar absorptivity. A separate saturated solution for each molecular weight was made, filtered, and serially diluted. The serial dilution is necessary because the detector cannot detect such high carbonyl absorptivity. The intensity of the carbonyl peak is obtained for each of the dilutions, compared to the Beer-Lambert Plot to determine the concentration, and then this concentration is multiplied by the dilution factor to determine the solubility limit. The P3HT solubility limit in chlorobenzene was obtained by following a similar procedure except with the use of a Thermo Scientific Evolution 300 UV-vis spectrophotometer and monitoring the intensity of the 457 nm peak.

Results

The effects of blend composition of P3HT:dPMMA (5:95, 10:90, 15:85, or 20:80), dPMMA molecular weight (20,000 g/mol, 131,500 g/mol, 316,000 g/mol, or 520,000 g/mol) and casting speed (209.4 rad/s, 104.7 rad/s, or 52.4 rad/s) on thin film vertical structure were examined via neutron reflectivity. Neutron reflectivity provides a

normalized reflection profile as a function of incident wave vector, Q. The neutron reflectivity data was fit using IGOR and Motofit software packages using a multi-layer model. The analysis provides a scattering length density (SLD) depth profile with the restraint that the SLD depth profile must adhere within 5% to the known composition of the sample. The SLD depth profile from each sample was transformed into a P3HT volume fraction as a function of the normalized thickness, where 0 denotes the air interface to 1 denotes the SiO_2 interface. The normalization of thickness allows a more direct comparison among the films formed from all casting speeds and polymer molecular weights. The transformation into the P3HT volume fraction transpires by employing Equation 3.2:

$$\frac{SLD_{layer}(z)-SLD_{dPMMA}}{SLD_{dPMMA}-SLD_{P3HT}} = \phi_{P3HT}(z) \qquad \text{Equation (3.2)}$$

where $SLD_{layer}(z)$ is the layer SLD of the sample at depth z, and $\varphi_{P3HT}(z)$ is the volume fraction of P3HT at depth z. The SLDs of P3HT and dPMMA were calculated from the NCNR SLD calculator. The SLD values used throughout these experiments are 0.7×10^{-6} $Å^{-2}$ and a range of $6.7 \times 10^{-6} Å^{-2}$–$7.1 \times 10^{-6}$ $Å^{-2}$ for P3HT and the range of molecular weights of dPMMA, respectively. The P3HT volume fraction depth profiles can be further analyzed to provide a qualitative measure of the stratification. The extent of stratification and the amount of error is determined by employing a previously described method.[127] In this method, the extent of stratification of a two-component system is compared to two theoretical limits: a homogenous (0%, non-stratified) thin film and a completely stratified (100%, two independently pure layers) thin film. The extent of stratification value obtained by this analysis describes the extent of vertical phase separation of the two components.

For example, a sample containing a 50/50 blend of two polymers is defined as stratified if any layer contains more than 50% of either polymer.

Our previous studies of the stratification in spin-coated films investigated the impact of molecular weight at a single spin speed (104.7 rad/s, Figure 3.1) as well as the impact of casting speed at a single molecular weight (131,500 g/mol, Figure 3.2) on the layered structure of the fabricated P3HT/dPMMA films. These results show that as the dPMMA molecular weight decreased, a decrease of extent of stratification was observed for all blend compositions prepared at 104.7 rad/s. In addition, as the P3HT concentration in the blend increased, the extent of stratification increased regardless of the molecular weight of dPMMA or casting speed used in the preparation of the sample. Moreover, the casting speed did not alter the variation in stratification of samples formed from high or low loadings of P3HT in the blend, yet a sample cast with a slower casting speed resulted in a larger extent of stratification relative to the same sample prepared at faster casting speeds.

The results reported in this manuscript expand the parameter space to include a matrix of conditions that include spin casting speed (and thus rate of film formation), dPMMA molecular weight, and blend composition. Figure 3.3 plots the extent of stratification of the fabricated films as a function of dPMMA molecular weight for samples containing four different blend compositions all cast at 209.4 rad/s. The samples consisting of blend compositions of P3HT:dPMMA 10:90, 15:85, and 20:80 prepared at 209.4 rad/s elicit a decrease in extent of stratification as the molecular weight of dPMMA decreases,

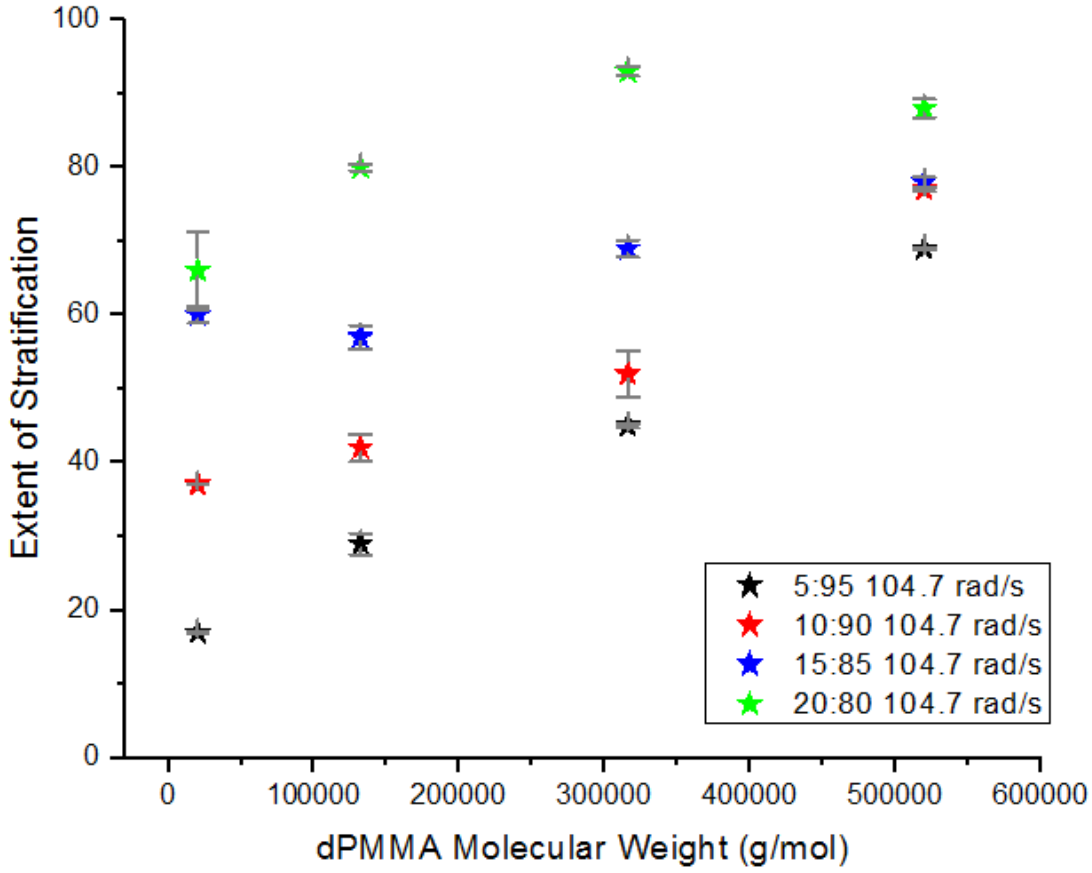


Figure 3.1 A previously reported (Fig. 2.8) plot of extent of stratification as a function of dPMMA molecular weight and blend composition 5:95 (black stars), 10:90 (red stars), 15:85 (blue stars), and 20:80 (green stars) all prepared at 104.7 rad/s.

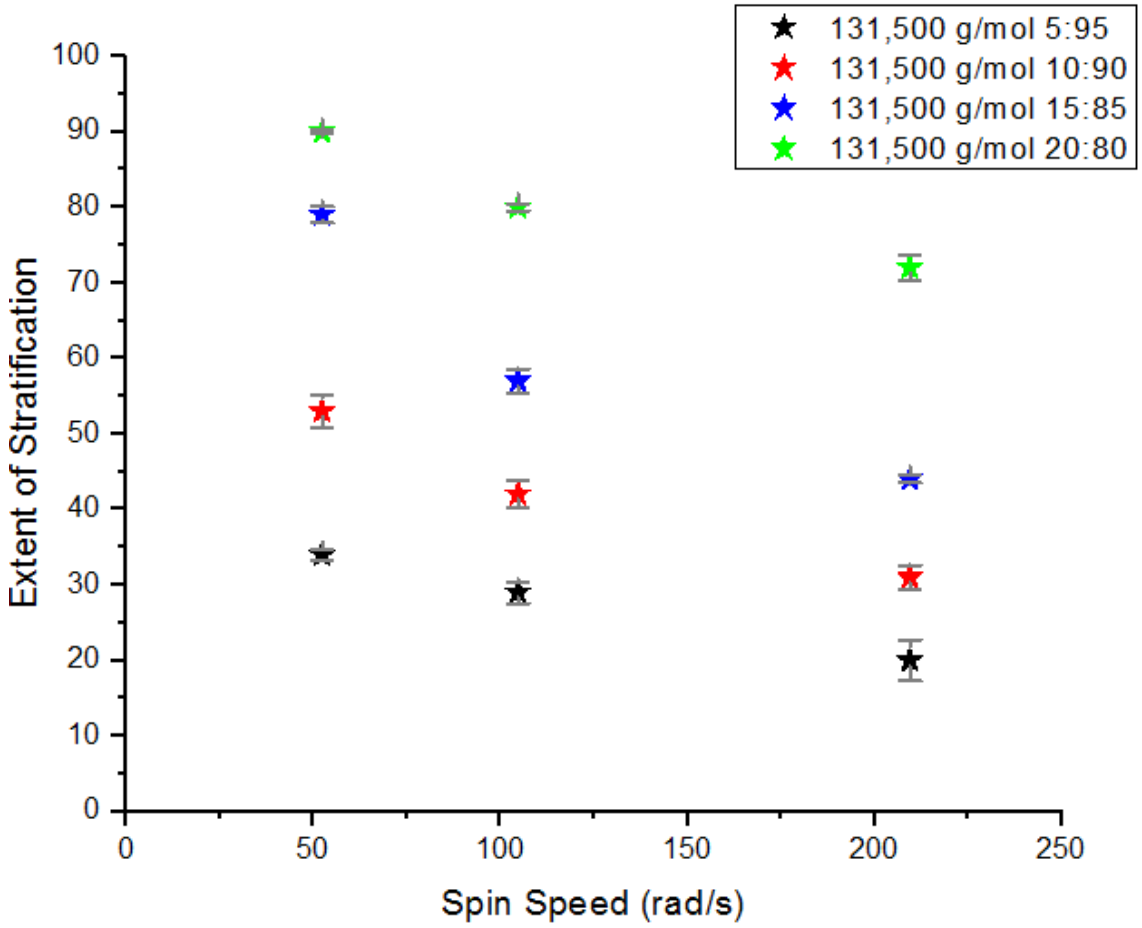


Figure 3.2 Previously reported (Fig. 2.6) plot of extent of stratification as a function of spin cast speed, and blend composition 5:95 (black stars), 10:90 (red stars), 15:85 (blue stars), and 20:80 (green stars) all prepared with 131,500 g/mol dPMMA.

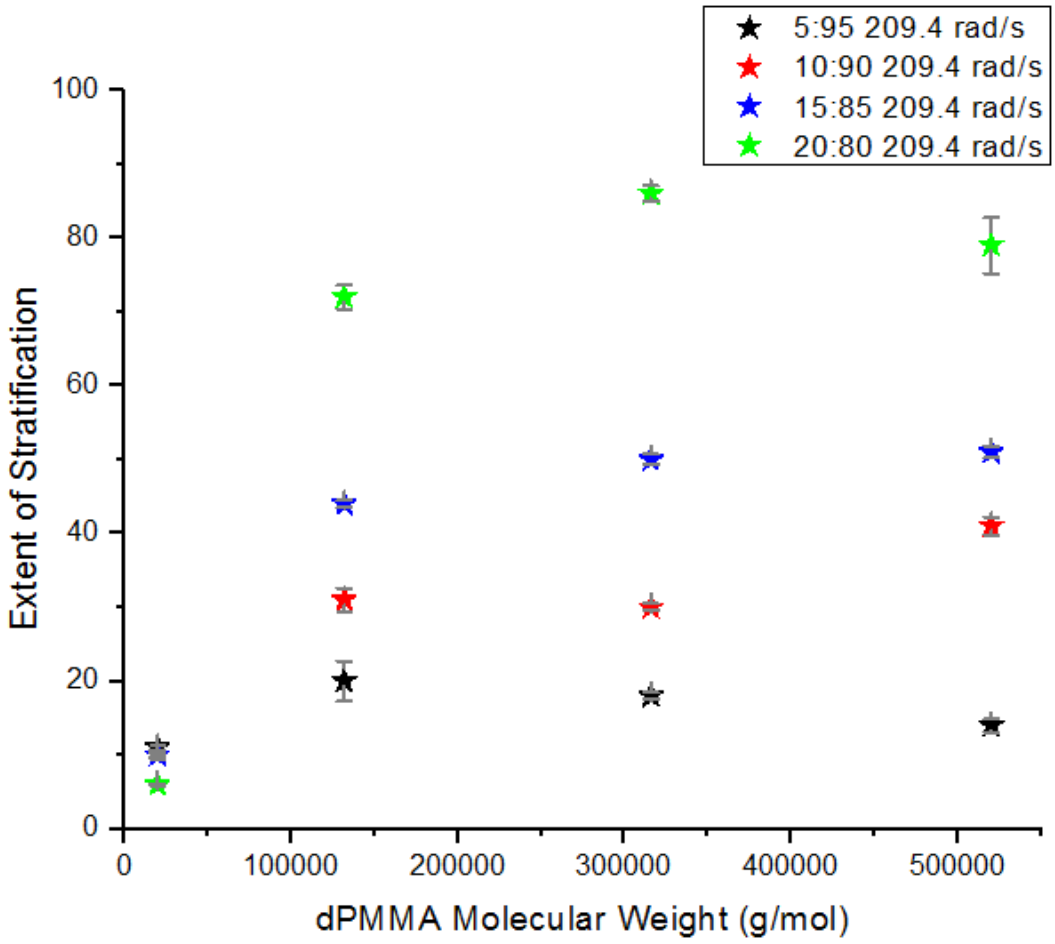


Figure 3.3 Plot of extent of stratification as a function of dPMMA molecular weight, and blend composition 5:95 (black stars), 10:90 (red stars), 15:85 (blue stars), and 20:80 (green stars) all prepared at 209.4 rad/s.

although the molecular weight impact on stratification is minimal relative to the samples prepared at 104.7 rad/s. On the contrary, the samples consisting of 5:95 show an increase in extent of stratification as a function of decreased dPMMA molecular weight from 520,000 g/mol to 131,500 g/mol. All blend compositions prepared with 20,000 g/mol dPMMA display a drastically reduced extent of stratification relative to all the other molecular weights measured. As the P3HT concentration increases in the blend composition, the extent of stratification increases for samples prepared with molecular weights of dPMMA of 131,500 g/mol, 316,000 g/mol, and 520,000 g/mol. Because the extents of stratification for all blend compositions comprised of 20,000 g/mol dPMMA are very similar, it is difficult to determine the impact of blend composition for these samples.

Figure 3.4 plots the extent of stratification for samples containing all four blend compositions cast at 52.4 rad/s as a function of dPMMA molecular weight in the blend. The overall trends for samples prepared at 52.4 rad/s as a function of blend composition and dPMMA molecular weight are less clear compared to the trends observed from samples prepared at faster casting speeds. When investigating each blend composition individually as a function of molecular weight, 5:95 is the only blend composition in which an increase in molecular weight elicits an increase in extent of stratification. The extent of stratification for samples prepared with a blend composition of 10:90 remains fairly constant across all molecular weights. The blend compositions 20:80 and 15:85 for molecular weights of 131,500 g/mol, 316,000 g/mol, and 520,000 g/mol exhibit a decrease in extent of stratification as dPMMA molecular weight increases. The same blend compositions

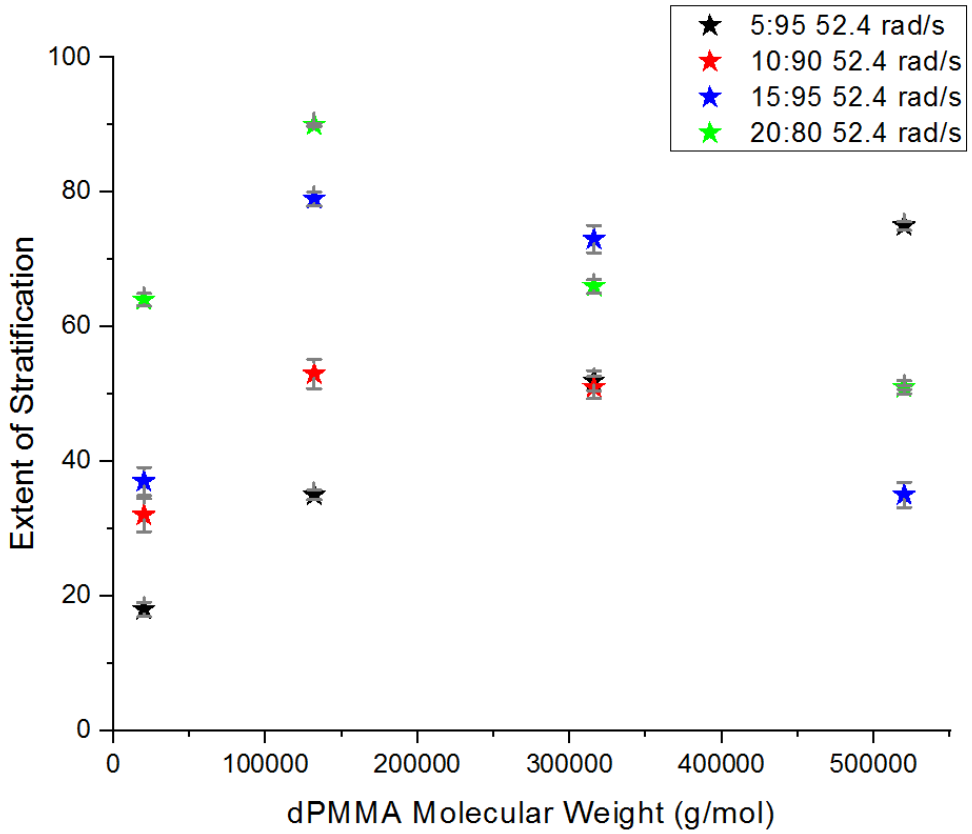


Figure 3.4 Plot of extent of stratification as a function of dPMMA molecular weight, and blend composition 5:95 (black stars), 10:90 (red stars), 15:85 (blue stars), and 20:80 (green stars) all prepared at 52.4 rad/s.

prepared with 20,000 g/mol dPMMA do not follow the same molecular weight dependence. For the most part, an increase in P3HT concentration elicits an increase in extent of stratification, however, this is only true for samples prepared with 131,500 g/mol or 20,000 g/mol dPMMA at 52.4 rad/s.

To further investigate the impact of film formation time (kinetics) upon final film structures and provide more insight into the driving forces of polymer blend stratification, films formed from each dPMMA molecular weight was investigated independently as a function of casting speed (209.4 rad/s, 104.7 rad/s, and 52.4 rad/s) for all P3HT:dPMMA blend compositions (5:95, 10:90, 15:85, 20:80). Evaluating the extent of stratification as a function of dPMMA molecular weight for samples prepared at 52.4 rad/s (Figure 3.4) reveal a difference amongst the samples prepared with dPMMA molecular weights of 316,000 g/mol and 520,000 g/mol compared to samples prepared with 20,000 g/mol and 131,500 g/mol dPMMA. Figures 3.5 and 3.6 display the extent of stratification as a function of casting speed for dPMMA molecular weights of 316,000 g/mol and 520,000 g/mol, respectively, while Figure 3.7 displays the extent of stratification as a function of casting speed for samples containing 20,000 g/mol dPMMA. The extent of stratification for samples containing 131,500 g/mol dPMMA as a function of casting speed can be referenced in Figure 3.2.

All P3HT:316k dPMMA samples, displayed in Figure 3.5, show an increase in extent of stratification as a function of decreased casting speed except for the sample prepared with a blend ratio of 20:80. The composition of 20:80 experiences the largest

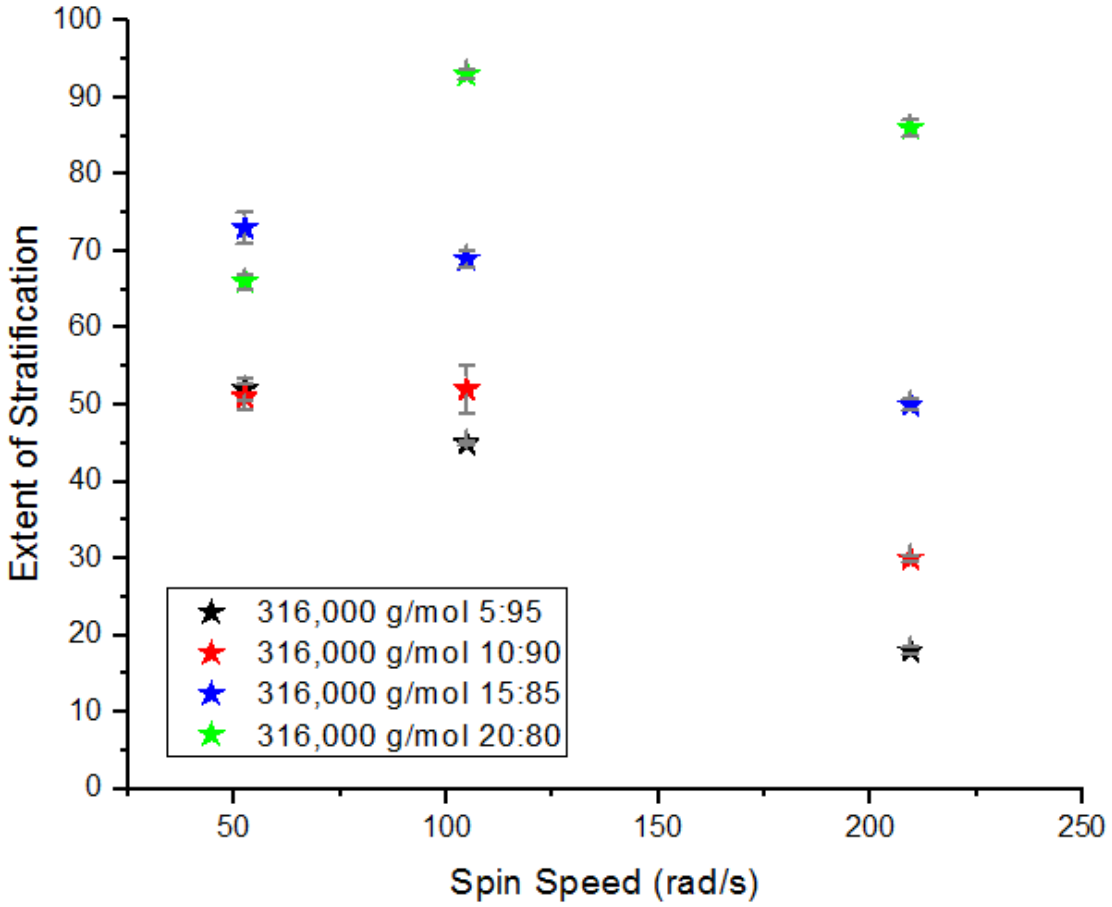


Figure 3.5 Plot of extent of stratification as a function of spin cast speed, and blend composition 5:95 (black stars), 10:90 (red stars), 15:85 (blue stars), and 20:80 (green stars) all prepared with 316,000 g/mol dPMMA.

extent of stratification when prepared at 104.7 rad/s, while all the other blend compositions result in the largest extents of stratification when prepared at the slowest casting speed, 52.4 rad/s.

Regardless of blend composition, decreasing the casting speed from 209.4 to 104.7 rad/s results in an increase in extent of stratification. The difference in extent of stratification between samples prepared at 104.7 rad/s and 209.4 rad/s is quite large. The increase in the extent of stratification in the films when decreasing the casting speed from 104.7 rad/s to 52.4 rad/s results in smaller, if any, increases for all the blend compositions except for the 20:80 blend. Apart from the differences in extent of stratification observed at each casting speed, all blend compositions exhibit a correlation to the concentration of P3HT in the blend, where an increase in P3HT concentration results in an increase in the extent of stratification. The only discrepancy from this trend is the extent of stratification observed for the 20:80 sample prepared at 52.4 rad/s.

Samples containing P3HT:520,000 g/mol dPMMA (Figure 3.6) prepared at 104.7 rad/s and 209.4 rad/s exhibit an increase in extent of stratification as a function of increasing P3HT concentration in the blend. However, an increase in P3HT concentration for samples prepared at 52.4 rad/s does not result in an increase in extent of stratification. In fact, the extent of stratification decreases for samples prepared at 52.4 rad/s relative to samples prepared at 104.7 rad/s for all blend compositions except the samples prepared with P3HT:dPMMA 5:95. Additionally, the previously determined impact of casting speed on extent of stratification (decrease in casting speed results in an increase in extent of

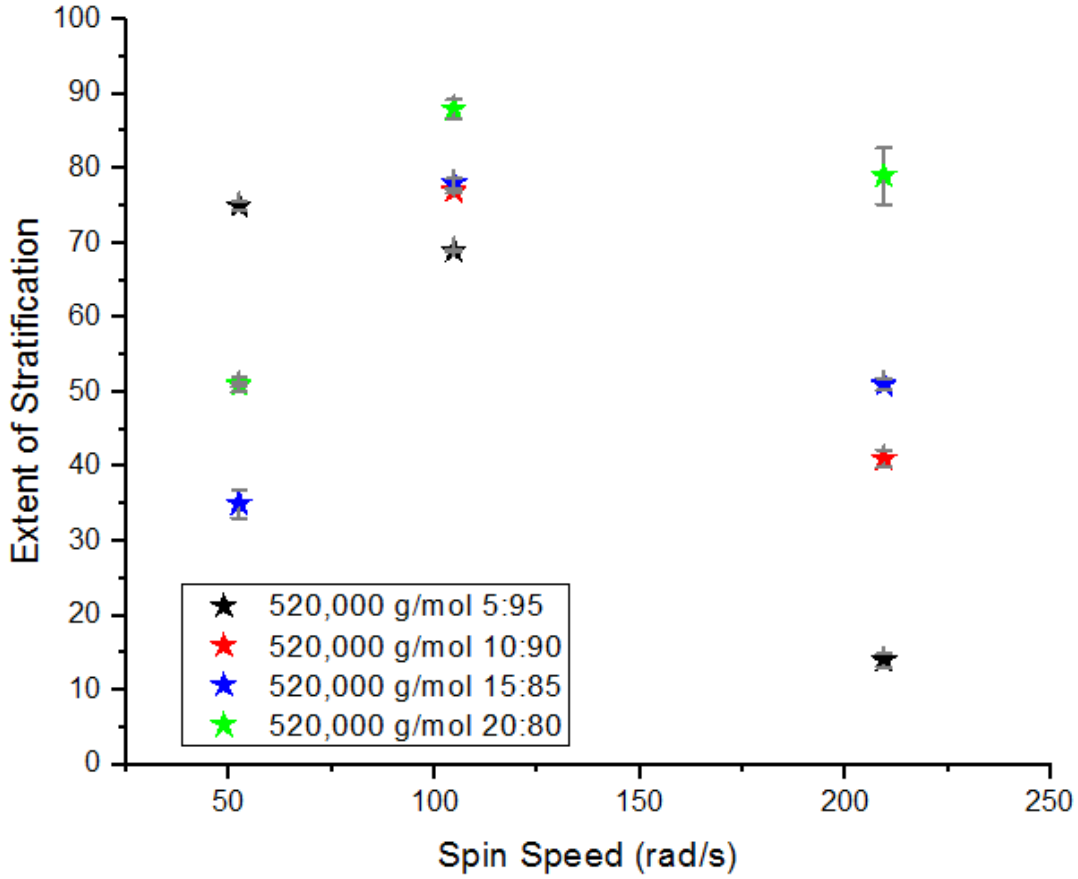


Figure 3.6 Plot of extent of stratification as a function of spin cast speed, and blend composition 5:95 (black stars), 10:90 (red stars), 15:85 (blue stars), and 20:80 (green stars) all prepared with 520,000 g/mol dPMMA.

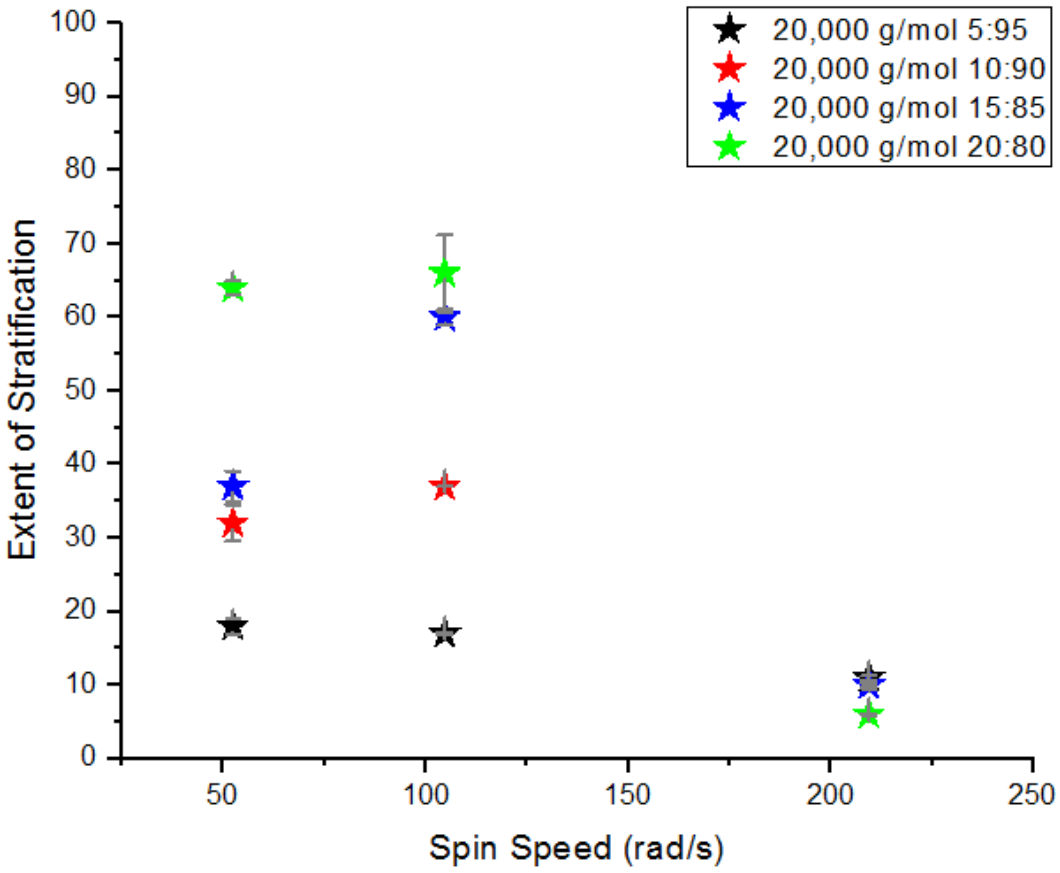


Figure 3.7 Plot of extent of stratification as a function of spin cast speed, and blend 5:95 (black stars), 10:90 (red stars), 15:85 (blue stars), and 20:80 (green stars) all prepared with 20,000 g/mol dPMMA.

stratification) is only observed for the samples prepared with 5:95 blend compositions. However, the extent of stratification does increase as the casting speed decreases from 209.4 rad/s to 104.7 rad/s for all the blend compositions, but when the samples are prepared at 52.4 rad/s, a further increase in extent of stratification is not observed for blend compositions of 10:90, 15:85, and 20:80.

The samples prepared with blend compositions of P3HT:20,000 g/mol dPMMA 5:95 result in an increase in extent of stratification as casting speed increases. The blend composition of 10:90 results in a relatively constant extent of stratification around 35%, for the slowest casting speeds, but when prepared at the fastest casting speed, a reduction in the extent of stratification occurs. The samples prepared with blend compositions of 15:85 and 20:80 result in a drastic increase in extent of stratification when the casting speed is decreased from 209.4 rad/s to 104.7 rad/s. The blend composition of 20:80 does not experience a change in the extent of stratification as the casting speed is decreased from 104.7 rad/s to 52.4 rad/s, yet the blend composition of 15:85 experiences a decrease in extent of stratification when changing the casting speed from 104.7 rad/s to 52.4 rad/s. The 15:85 blend composition obtains the largest extent of stratification (60%) occurring when prepared at 104.7 rad/s, approximately 20% larger than the extent of stratification for this sample prepared at 52.4 rad/s. For the samples containing 20,000 g/mol dPMMA, the influence of P3HT concentration in the blend is dependent upon the casting speed. When samples are prepared at 52.4 rad/s or 104.7 rad/s, an increase in P3HT concentration leads

to an increase in extent of stratification. Contrarily, when samples are prepared at 209.4 rad/s, the impact of P3HT concentration upon the extent of stratification is unclear.

Discussion

The results presented here investigate the combined impact of the kinetics of casting and the polymer molecular weights on the extent of stratification of spin-cast polymer blend films. Our previous results (Figures 3.1 and 3.2) indicate that molecular weight, film formation kinetics, and polymer loading, all play similar, yet independent roles in dictating the final film layering structure. As a brief review, our previous results found that an increase in P3HT concentration, which alters the miscibility of the blend, a decrease in casting speed, which increases film formation time, and an increase in dPMMA molecular weight, which alters the entropy of mixing, each independently increase the extent of stratification in the fabricated blend film. The previous study examined each independently and cannot speak to their relative impacts on stratification. To more accurately define the relative importance of these factors in determining the extent of stratification in spin cast polymer blend thin films, we have expanded our studies to investigate thin films consisting of P3HT:dPMMA blends (5:95, 10:90, 15:85, 20:80), with one of three dPMMA molecular weights (20,000 g/mol, 316,000 g/mol, 520,000 g/mol), prepared at one of three casting speeds (209.4 rad/s, 104.7 rad/s, 52.4 rad/s). The vertical structure of thin films formed from all blend compositions and all molecular weights of dPMMA prepared at 104.7 rad/s as well as blends including 131,500 g/mol dPMMA prepared at all casting speeds have been previously reported and will not be reviewed in

this chapter, but the conclusions from those studies will be referenced throughout this discussion.[127] The discussion will be organized by first examining the impact of casting speed (209.4 rad/s then 52.4 rad/s) and will proceed to elucidate the role of dPMMA molecular weight in the extent of stratification in the spin cast polymer blend film.

209.4 rad/s Casting Speed Preparation

dPMMA Molecular Weight

The extents of stratification of all the samples prepared at 209.4 rad/s are provided in Figure 3.3. For each specific blend composition prepared at 209.4 rad/s, the molecular weights of the dPMMA did not have a significant impact on the extents of stratification. This is contrary to the samples that are prepared at 104.7 rad/s, where a dependence of dPMMA molecular weight was found. This change may be attributed to the film formation time, where the samples prepared at 209.4 rad/s have a shorter film formation time than those made at 104.7 rad/s.[127] We attributed the stratification of the samples prepared at 104.7 rad/s to the entropic surface segregation of the smaller P3HT chains (i.e. an entropic phase separation) during the slightly longer film formation time. Due to the shorter film formation time of the 209.4 rad/s samples, we believe that there is not ample time for the smaller P3HT chains to stratify in the spin casting process. Since chain end concentration correlates to the amount of entropy in the system, our results indicate that entropy plays a reduced role in the final film structure when samples are prepared at 209.4 rad/s, relative to when samples are prepared at 104.7 rad/s. However, the extents of stratification for all P3HT:20,000 g/mol dPMMA blends are significantly reduced relative to the blends

containing larger molecular weight dPMMA. P3HT (~ 20,000 g/mol) and 20,000 g/mol dPMMA have similar molecular weights and we can assume that both polymers contain the same amount of free energy or entropy. Considering each polymer contributes a similar amount of entropy to the system, the entropic contribution would not drive de-mixing of the two polymers. Therefore, entropy plays a reduce role in driving stratification when samples are prepared at 209.4 rad/s relative to slower casting speeds, yet the entropic driving force must be present for other driving forces to have an impact on stratification.

P3HT Concentration

At 209.4 rad/s, the extent of stratification increases as the P3HT concentration increases in the blend for all dPMMA molecular weights, except the smallest dPMMA chains (20,000 g/mol) (Figure 3.3). The samples prepared with 20,000 g/mol dPMMA do not show a trend as a function of extent of blend composition. The 5:95, 10:90, and 15:85 blends result in the similar extents of stratification while the 20:80 blend has a reduced extent of stratification. Despite this result, the extent of stratification increase for less P3HT concentrated blends is very minimal when compared to the impact P3HT concentration has in larger dPMMA molecular weight blends prepared at 209.4 rad/s as demonstrated in the supplementary information.

The P3HT volume fraction depth profiles (PVFDP) are obtained by transforming the scattering length density profiles derived from the neutron reflectivity multi-layer fits. The PVFDP provide crucial insight into the stratification patterns and must be examined to inform our understanding of the samples prepared with 20,000 g/mol dPMMA at 209.4

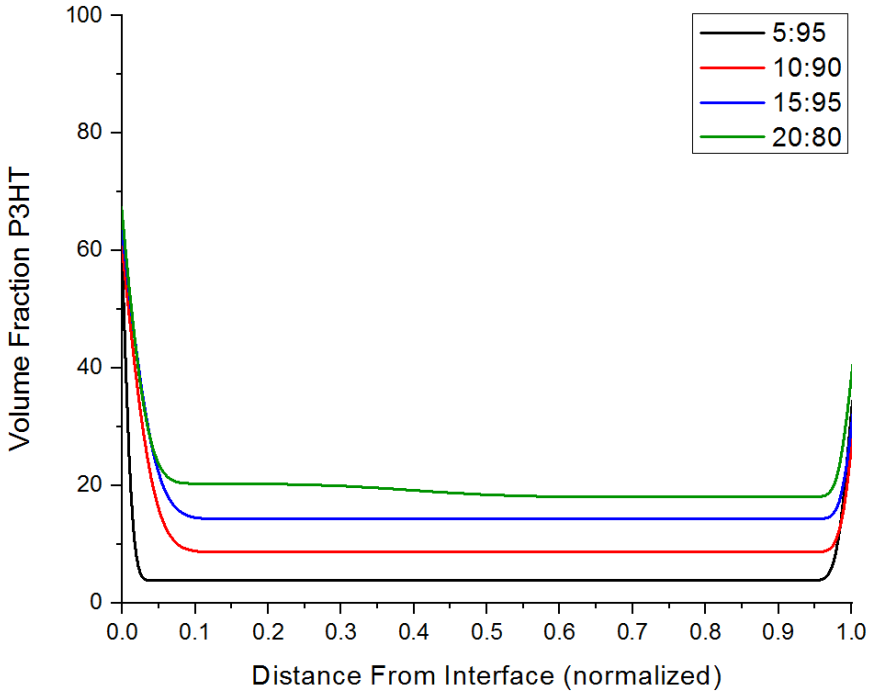


Figure 3.8 Plot of P3HT Volume Fraction Depth Profile for samples prepared with 20,000 g/mol dPMMA at 209.4 rad/s as a function of blend composition 5:95 (black), 10:90 (red), 15:85 (blue), and 20:80 (green).

rad/s (Figure 3.8). Films formed from all blend compositions result in a relatively constant P3HT concentration throughout the entire thickness of the film.

Our previous work ascribes the increase in extent of stratification observed with P3HT concentration to the phase separation of the dPMMA and P3HT due to repulsive interactions between the two polymers. These repulsive interactions are consistent with a decrease in miscibility of the blend with increased loading of the P3HT, and the observed increase in stratification with P3HT concentration at the highest dPMMA molecular weights. We attribute the limited stratification of the P3HT (MW ~ 20,000 g/mol) and low molecular weight dPMMA (20,000 g/mol) films prepared at 209.4 rad/s to a decrease in P3HT and dPMMA immiscibility relative to the blends that contain the larger molecular weight dPMMA (131,500 g/mol, 316,000 g/mol, 520,000 g/mol). The molecular weight dependence of the miscibility of two polymers is captured by the Flory-Huggins thermodynamic theory on mixing (Equation 3.3), where Equation 3.3 describes how the degree of polymerization (N) of each polymer (A and B) impacts the critical interaction parameter (χ_c).[104,105]

$$\chi_c = \frac{1}{2} * \left(\frac{1}{\sqrt{N_A}} + \frac{1}{\sqrt{N_B}}\right)^2 \qquad \text{Equation (3.3)}$$

The critical interaction parameter is a dimensionless thermodynamic value describing the propensity of two materials (polymer-polymer or polymer-solvent) to form a homogenous system. A positive χ_c close to zero describes a blend that is less likely to form a homogenous solution, relative to a larger positive χ_c which describes a blend more likely to mix. To understand our results, Equation 3.3 is employed to estimate the critical

interaction parameter of two polymers of different molecular weights where the degree of polymerization of P3HT (N_A) is kept constant as the degree of polymerization of dPMMA (N_B) is changed. The critical interaction parameters for each P3HT and dPMMA blend is thus provided in Table 3.1 which shows that increasing the degree of polymerization of dPMMA, N_B , decreases χ_c. This is further interpreted to indicate that P3HT/dPMMA blends containing larger molecular weights of dPMMA are less likely to be homogenous and more likely to phase separate relative to blends containing a lower molecular weight dPMMA. The lack of stratification in the 20,000 g/mol dPMMA samples prepared at 209.4 rad/s is also consistent with the lack of an entropic driving force for the smaller polymer to segregate tot eh surface as both polymers in this blend have very similar chain lengths.

52.4 rad/s Casting Speed

To understand the impact of blend composition and molecular weight on the extent of stratification at the slowest film formation time, all dPMMA molecular weights and blend compositions were prepared at 52.4 rad/s. These extents of stratification of these samples are plotted as a function of the dPMMA molecular weight in Figure 3.4. The impact of dPMMA molecular weight on the extent of stratification for samples prepared at 52.4 rad/s is less clear relative to the impact of dPMMA molecular weight for samples prepared at the two faster casting speeds. The stratification of the blend composition of 5:95 increased steadily with the dPMMA molecular weight, while the other compositions exhibited an increase in extent of stratification at low dPMMA molecular weight but remain constant or decrease for the two largest dPMMA molecular weights. The impact of

Table 3.1 Critical interaction parameters based on the molecular weight of P3HT and dPMMA in each blend.

dPMMA Molecular Weight (g/mol)	$\chi_{c(\mathbf{P3HT-PMMA})}$
20,000 g/mol	0.0128
131,500 g/mol	0.007
316,000 g/mol	0.006
520,000 g/mol	0.005

P3HT concentration on the extent of stratification is slightly clearer than the impact of molecular weight for the samples prepared at 52.4 rad/s. Nonetheless, the impact of P3HT concentration on the extent of stratification is not trivial for the polymer blend films prepared at 52.4 rad/s. As P3HT concentration increases in the blend, the extent of stratification increases for samples prepared with either 20,000 g/mol and 131,000 g/mol dPMMA molecular weights, but the behavior of the samples prepared with 316,000 g/mol and 520,000 g/mol dPMMA are more complex. Investigating the stratification of the 316,000 g/mol and 520,000 g/mol dPMMA samples prepared at 52.4 rad/s independently may aid in elucidating the driving forces that guide extent of stratification when these samples are prepared at this casting speed.

316,000 g/mol dPMMA

In the blend thin films that contain 316,000 g/mol molecular weight dPMMA, the extent of stratification does not clearly correlate to the P3HT concentration in the blend. The blend compositions that exhibit the smallest extent of stratification are the 5:95 and 10:90 samples (~50%) followed by the 20:80 film (66%) and finally, 15:85 (73%). To understand this non-linear behavior, unlike the stratification of the samples that contain 20,000 g/mol and 132,000 g/mol dPMMA, the PVFDP of these films must be inspected (Figure 3.9).

Inspection of Figure 3.9 shows that the blends composed of 5:95 and 10:90 have P3HT rich layers at the air interface, while the 15:85 and 20:80 blends have P3HT rich layers at both interfaces. The blend containing 15:85 P3HT:316,000 g/mol dPMMA has a

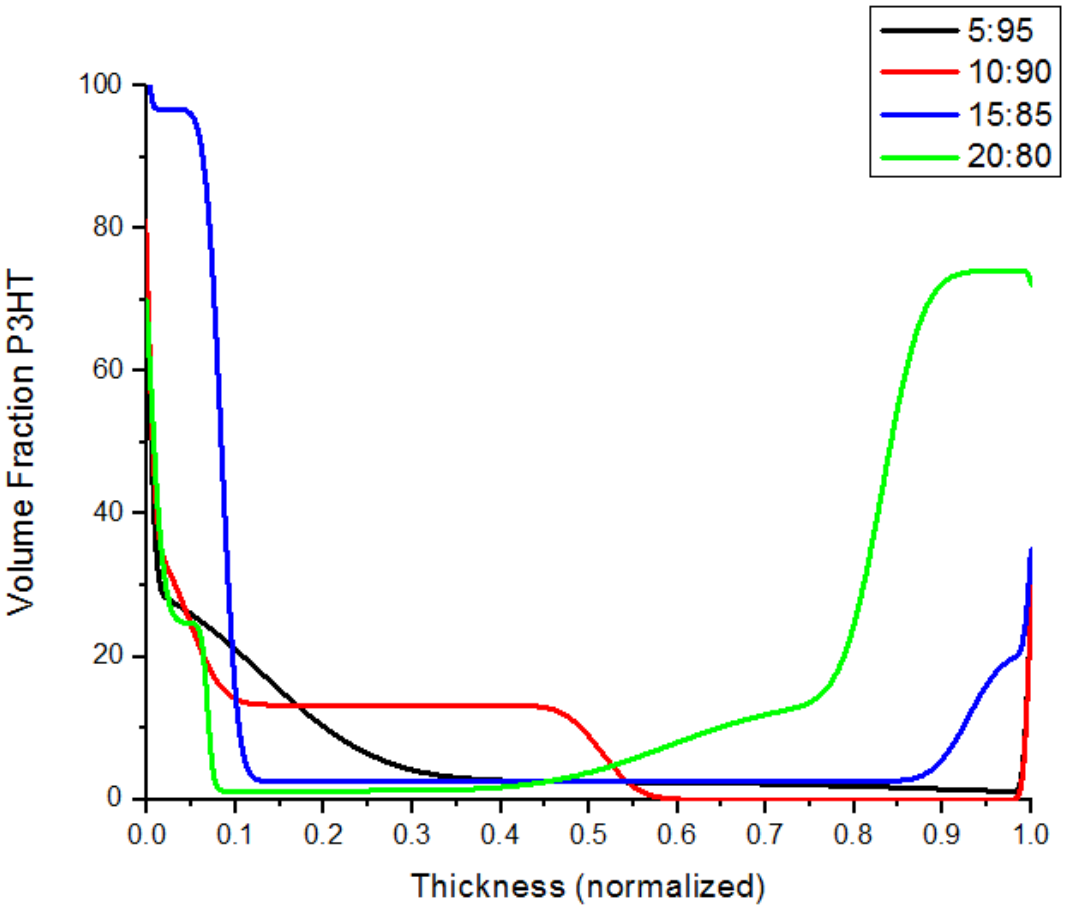


Figure 3.9 Plot of P3HT Volume Fraction Depth Profile for samples prepared with 316,000 g/mol at 52.4 rad/s as a function of blend composition 5:95 (black), 10:90 (red), 15:85 (blue), and 20:80 (green).

thin layer of nearly pure P3HT at the air interface, while the P3HT in the layer at the silicon interface is not the majority component. The blend containing 20:80, on the other hand, has a highly concentrated P3HT layer at the silicon surface, while the P3HT layer at the air interface contains a lower concentration of P3HT.

A P3HT rich layer forming at the Si interface is unexpected based on the thermodynamic properties of the film, including the entropic driving forces and surface energy. The surface energy and molecular weight of P3HT is much lower than that of dPMMA in these blends. If the surface energy was the dominant driving force responsible for stratification, P3HT would segregate to the air interface. Additional driving forces for stratification must be considered to explain the P3HT rich layer at the Si surface when this blend of P3HT:dPMMA is prepared at 52.4 rad/s.

As the casting speed is decreased during film fabrication, the film formation time increases due to slower solvent evaporation times. As solvent evaporates, the concentration of solids dissolved in solvent increases until the final film formation. At a certain point in the solvent evaporation process, the solubility limit of a polymer is reached, and the polymer precipitates. At fast casting speeds, the precipitation of the polymer and the final film formation appear to occur nearly simultaneously, and the solubility limit of the polymer does not appear to impact the film structure. However, as the casting speed decreases, the amount of time between the precipitation of the polymer and the final film formation increases. Since we only observe P3HT formation at the Si surface at the slowest

casting speed, it seems reasonable that the relative solubility limits need to be considered for these slow casting speeds.

The solubility for all the polymers in the casting solvent (chlorobenzene) used in this study were experimentally determined and are plotted in Figure 3.10. The solubility limit of P3HT in chlorobenzene (16 mg/mL) is an order of magnitude less than the solubility of all the dPMMA samples in chlorobenzene (10-32 g/mL depending on molecular weight). It is important to note that the solubility of each polymer is well above the solution concentrations used to cast the thin films and prior to spin casting, i.e. both polymers are fully dissolved in chlorobenzene in the pre-casting solution. Despite this fact, spin casting drives solvent evaporation, leading to an increase solid concentration during spin coating, where the polymer concentration crosses the solubility limit of each polymer during deposition. Since P3HT is less soluble in chlorobenzene, P3HT reaches its solubility limit first. We therefore attribute the formation of P3HT rich layers at the Si interface for samples containing P3HT:dPMMA 15:85 and 20:80 to the large differences in the solubility limits of dPMMA and P3HT in chlorobenzene. During the casting process and solvent evaporation, P3HT reaches its solubility limit prior to dPMMA. Once the solubility limit is reached, P3HT precipitates from solution, and forms a layer of P3HT at the silicon surface. This interpretation is consistent with the fact that the P3HT rich layer at the Si surface transpires for samples with higher concentrations of P3HT. These blends reach the solubility limit more quickly than the lower concentration blends at the same casting speed. The precipitation of P3HT initiates a phase separation for the otherwise miscible blend

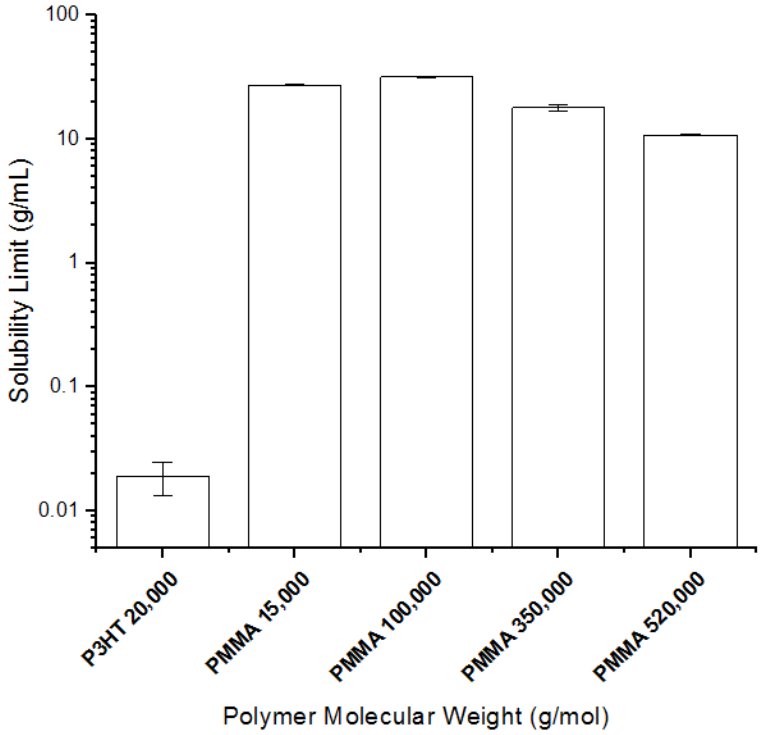


Figure 3.10 Solubility of the polymers utilized in this study in chlorobenzene.

solutions resulting in the P3HT rich layer found at the Si interface for the blends with higher P3HT concentration. This precipitation results in increased extents of stratification relative to the blends containing a lower P3HT concentration.

Additionally, the formation of a thin P3HT layer at the silicon substrate masks the surface energy of the substrate (becoming similar to P3HT) leading to a drastic increase in the apparent surface energy of the substrate. This change in substrate surface energy further drives P3HT towards the Si surface, in addition to the otherwise preferred air interface. The simultaneous driving forces that sequester the P3HT to both air and silicon interfaces results in smaller extents of stratification for samples prepared at 52.4 rad/s when the solubility limit is reached prior to final film formation.

520,000 g/mol dPMMA

To utilize the same analysis process as above, the PVFDP of the thin film blends that include 520,000 g/mol dPMMA prepared at 52.4 rad/s are provided in Figure 3.11. Unlike the samples prepared with 316,000 g/mol dPMMA, the blend composition resulting in the largest extent of stratification is 5:95 (75%) followed by 20:80 and 10:90 having almost the same extent of stratification (51%) and finally, 15:85 has the lowest extent of stratification (35%).

The P3HT rich layer organizes at the air interface for the sample containing 5:95 and it is the only sample with this structure. The blend composition of 20:80 is comprised of a P3HT rich layer at the air interface, as well as at the silicon substrate. The 20:80 sample

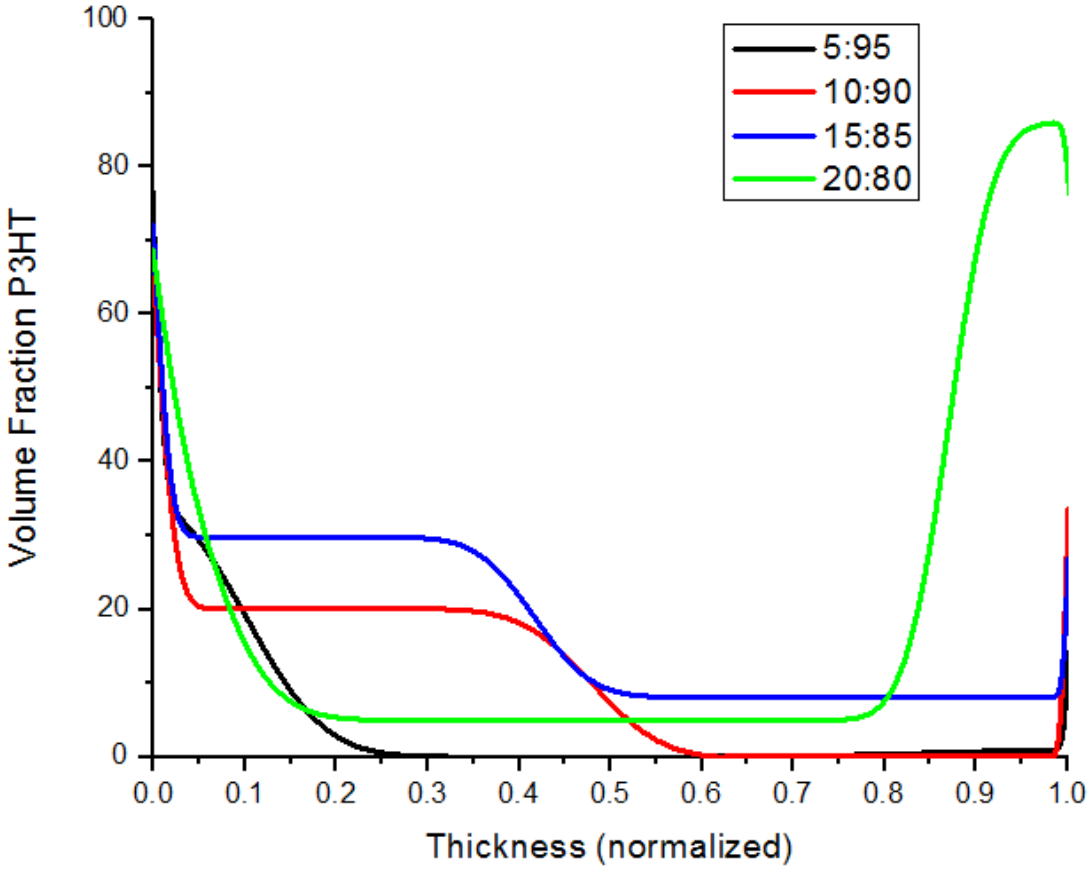


Figure 3.11 Plot of P3HT Volume Fraction Depth Profile for samples prepared with 520,000 g/mol at 52.4 rad/s as a function of blend composition 5:95 (black), 10:90 (red), 15:85 (blue), and 20:80 (green).

is the only sample where a P3HT rich layer is found at the Si substrate. The middle two blend compositions (10:90 and 15:85) exhibit similar stratification patterns to one another where the P3HT rich layer seems to broaden into the middle bulk of the film. The P3HT layer accumulating at the silicon substrate is explained by the premature precipitation of P3HT occurring prior to film formation, yet the reason that the P3HT extends into the bulk of the film is less understood. This middle layer is found in the top half of the film closest to the air interface, consistent with the stratification of P3HT towards the air interface. As mentioned above, the precipitation of P3HT during the deposition process appears to be an important process in the development of the stratification of slowly formed blend films. In this process, the precipitated P3HT must also diffuse though the solvated dPMMA to reach the silicon substrate. The rate at which P3HT diffuses through solvated dPMMA is dictated by the size of the dPMMA chains, where the diffusion of the P3HT chains through a larger dPMMA matrix will be slower than its diffusion through a smaller matrix.

The slower diffusion of P3HT through the 520,000 dPMMA matrix manifests as the broadening of the P3HT concentration profile in the middle of the film rather than at the silicon surface. Additionally, the inability of P3HT is unable to phase separate from dPMMA leads to a decrease in the extent of stratification for the higher concentration P3HTR samples. The coupling of this precipitation to the entropic and enthalpic driving forces for stratification results in a complex process that is difficult to control for the high chain length dPMMA samples. However, these results do reveal the importance of considering the solubility limits of the polymers in the pre-deposition solvent, especially

when the polymer with the lower solubility limit is the polymer with the smallest surface energy.

Influence of Film Formation Time on Stratification

These results indicate that an increase in miscibility and reaching the solubility limit may dominate the film formation process over other entropic and enthalpic driving forces. The results presented above show that the increased miscibility of polymers with the same molecular weight leads to more homogeneous and less stratified samples, but only at the fastest casting speed and that the relative solubility limits of the two polymers needs to be considered at the slowest casting speed. Determining the dominant driving force(s) for the stratification of the polymer blend films at each specific spin speed provides an interesting summary of the results. With this in mind, the extents of stratification as a function of casting speed for each molecular weight (316,000 g/mol, 520,000 g/mol, 20,000 g/mol) and blend composition are provided in Figures 3.5, 3.6, and 3.7, respectively.

316,000 g/mol dPMMA

Figure 3.5 shows the extent of stratification for samples containing 316,000 g/mol as a function of casting speed and blend composition. The extent of stratification increases as the casting speed decreases for three of the four blend compositions (5:95, 10:90, and 15:85). The 20:80 blend thin film exhibits an increase in extent of stratification as the casting speed decreases from 209.4 rad/s to 104.7 rad/s, but the extent of stratification decreases for the slowest casting speed analyzed. We attribute this decrease in stratification

to P3HT precipitating from solution prior to film formation, as in the previous section. It is noteworthy that, except for this slowest casting speed and highest blend composition, the extent of stratification increases as the casting speed decreases, or as film formation time is extended. This result agrees with previous results that monitor the extent of stratification as a function of casting speed for similar P3HT:dPMMA blend thin films that contain 131,500 g/mol dPMMA.

520,000 g/mol dPMMA

The thin film formed from the 5:95 blend with 520,000 g/mol dPMMA exhibits an increase in the extent of stratification with a decrease in casting speed (which correlates to an increase in film formation time), as shown in Figure 3.6. The three blend compositions with highest concentrations of P3HT (10:90, 15:85, and 20:80) exhibit an increase in the extent of stratification as casting speed decreases from 209.4 rad/s to 104.7 rad/s but shows a drastic decrease in extent of stratification at the slowest casting speed (52.4 rad/s)/longest film formation time. The more concentrated P3HT blend compositions result in reduced extents of stratification due to the precipitation of P3HT from solution during film formation and the inhibited diffusion of P3HT to the silicon interface in the high dPMMA molecular weight matrix. The studies of the stratification of the 316,000 g/mol and 520,000 g/mol dPMMA samples as a function of casting speed indicate that the longer film formation time does indeed provide a driving force to increase the extent of stratification, except when the film formation time is long enough that solubility limit of the P3HT inhibits stratification of P3HT to the air interface.

20,000 g/mol dPMMA

The solubility limits of P3HT interfered with the extent of stratification as a function of casting speed trends for samples prepared with 131,500 g/mol and 520,000 g/mol dPMMA at slow casting speeds, while at fast casting speeds, the improved miscibility of 20,000 g/mol P3HT and 20,000 g/mol dPMMA inhibited stratification as well. To complete this study, the extent of stratification of the 20,000 g/mol dPMMA blend as a function of casting speed is also analyzed and is shown in Figure 3.7.

As the casting speed is decreased, the 5:95 blend experiences an increase in extent of stratification. Casting speed has an inverse relationship with film formation time, and therefore, an increase in film formation time leads to an increase in extent of stratification, agreeing with previous results. However, this is not the case for the other three blend compositions 10:90, 15:85, and 20:80. For the 10:90 and 15:85 samples, the extent of stratification drastically increases as the casting speed decreases from 209.4 rad/s to 104.7 rad/s, but decrease in the extent of stratification as the casting speed decreases further from 104.7 rad/s to 52.4 rad/. Meanwhile, the extent of stratification of the film formed from the 20:80 blend remains consistent at ~65% at the slower spin speeds. To understand these trends, the PVFDP are analyzed. The PVFDP for samples containing 20,000 g/mol dPMMA prepared at 209.4 rad/s are shown in Figure 3.8 and the PVFDP for the same samples prepared at 52.4 rad/s and 104.7 rad/s are displayed in Figures 3.12 and 3.13.

In the depth profiles for samples prepared at the slowest spin speed, 52.4 rad/s, P3HT rich layers are found near the air interface (0) that extend into the middle of the film

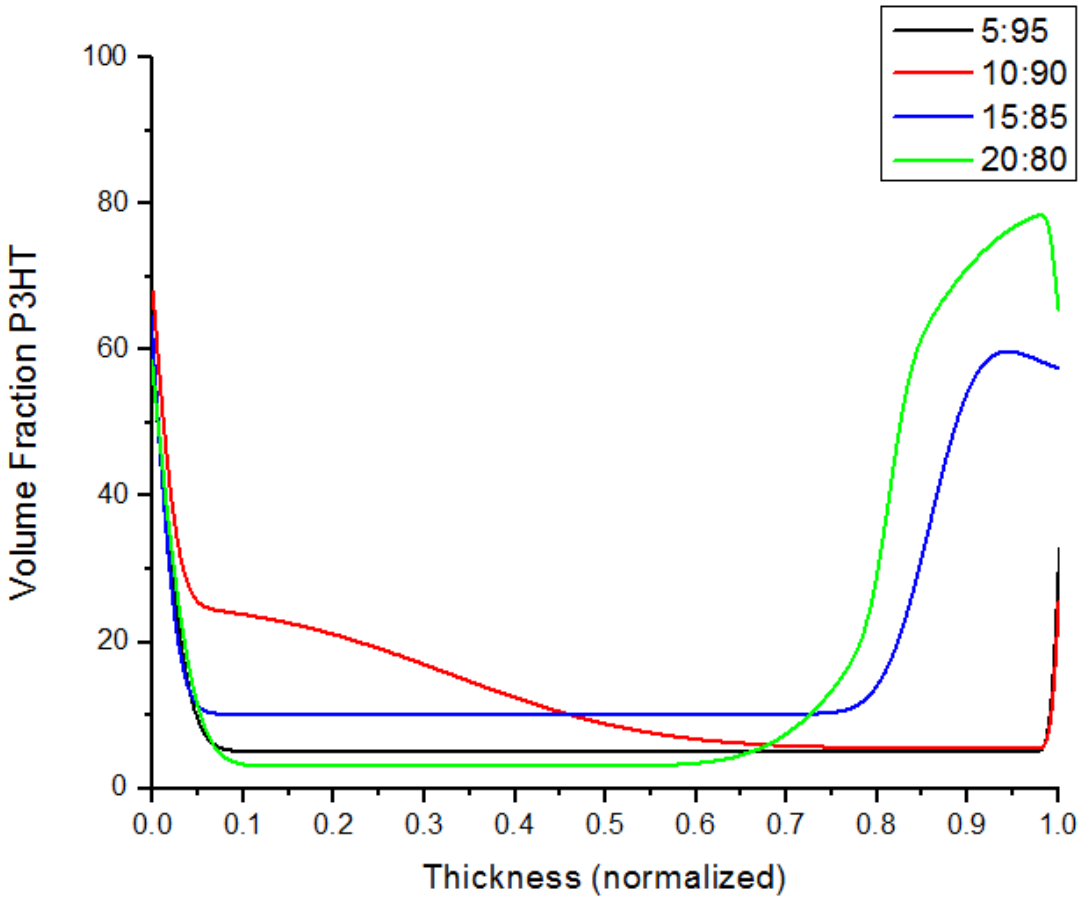


Figure 3.12 Plots of P3HT Volume Fraction Depth Profiles for samples prepared with 20,000 g/mol at 52.4 rad/s as a function of blend composition 5:95 (black), 10:90 (red), 15:85 (blue), and 20:80 (green).

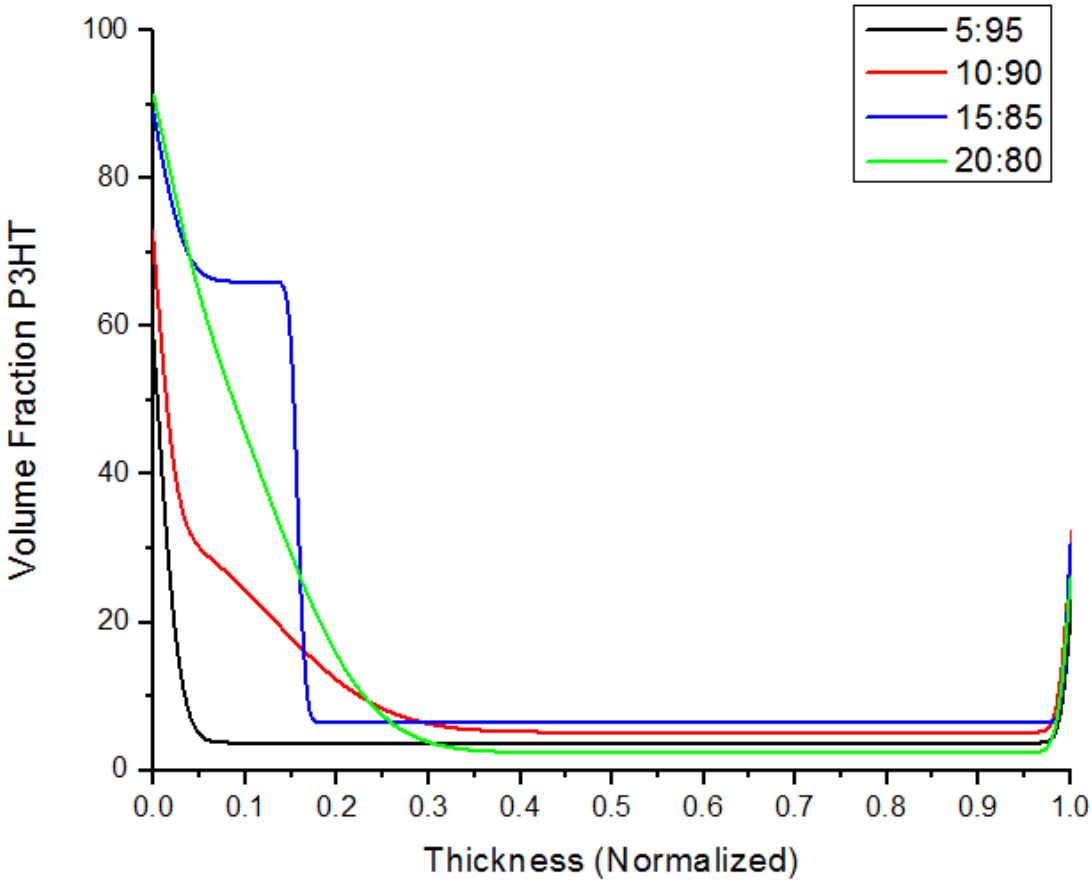


Figure 3.13 Plots of P3HT Volume Fraction Depth Profiles for samples prepared with 20,000 g/mol at 104.7 rad/s as a function of blend composition 5:95 (black), 10:90 (red), 15:85 (blue), and 20:80 (green).

for the 5:95 and 10:90 blend compositions. The 15:85 and 20:80 blend compositions form a P3HT rich layer at the silicon interface. It is interesting that even though the P3HT rich layers do not form at the same air or silicon interface, the extents of stratification for each of these blend compositions appears to increase with the concentration of P3HT in the blend. This result emphasizes that only looking at the extent of stratification for a specific sample does not describe the stratification completely. The P3HT layers formed at the silicon substrate for the highest blend compositions are ascribed to the precipitation of P3HT prior to film formation. The extent of stratification is largest for the samples cast at 104.7 rad/s, rather than the samples cast with the slowest casting speed. The precipitation of P3HT competes with the entropic and surface energy factors driving P3HT to the air interface for samples cast at the slowest casting speeds and although the extent of stratification is larger for films formed at slightly higher speeds, the precipitation may also play a role in the stratification of films formed at slightly faster spin speeds as well. For samples with 20,000 g/mol prepared at 104.7 rad/s (Figure 3.13), the P3HT layers are only found at the air interface but show either two P3HT rich layers with varying concentrations, or a P3HT rich layer with broad interface (gradual change in concentration) into the PMMA rich layer for the 10:90, 15:85, and 20:80 blends. This is consistent with the segregation of the P3HT to the air interface, combined with the precipitation of P3HT during film formation, but the impact of this precipitation is less apparent than the samples prepared at a slower casting speed and longer film formation time. The precipitation of P3HT competes

with the forces responsible for driving P3HT to the air interface which may decrease the extent of stratification measured for these samples.

131,500 g/mol dPMMA

The highly concentrated P3HT blend compositions prepared with 20,000 g/mol, 316,000 g/mol, and 520,000 g/mol dPMMA exhibit P3HT precipitation when prepared at the slowest casting speed, 52.4 rad/s. Figure 3.14 compares the PVFDP of samples consisting of 131,500 g/mol dPMMA prepared at 52.4 rad/s. Regardless of blend composition, all samples stratify to form P3HT rich layers at the air interface. As with the 20,000 g/mol samples prepared at 104.7 rad/s, the P3HT rich layers at the air interface show two to three distinct P3HT rich layers each with different P3HT concentrations. This is consistent with P3HT precipitation where its segregation to the Si surface is attenuated by other driving forces (i.e. lower surface energy and smaller molecular weight) that pull P3HT to the air interface. The fact that the 131,500 dPMMA is a longer chain than the P3HT in this samples means that there is a larger entropic driving force for the P3HT to go to the surface than in the 20,000 dPMMA samples. This larger entropic driving force can compete with the segregation of the P3HT to the Si surface that is driven by the P3HT precipitation, where this competition results in a layering of the P3HT in the film, but no segregation at the Si surface.

Since the entropic driving force for P3HT to stratify at the air interface increases with larger molecular weight dPMMA, the influence of the P3HT solubility limit on the stratification therefore decreases with increasing dPMMA chain length. These results

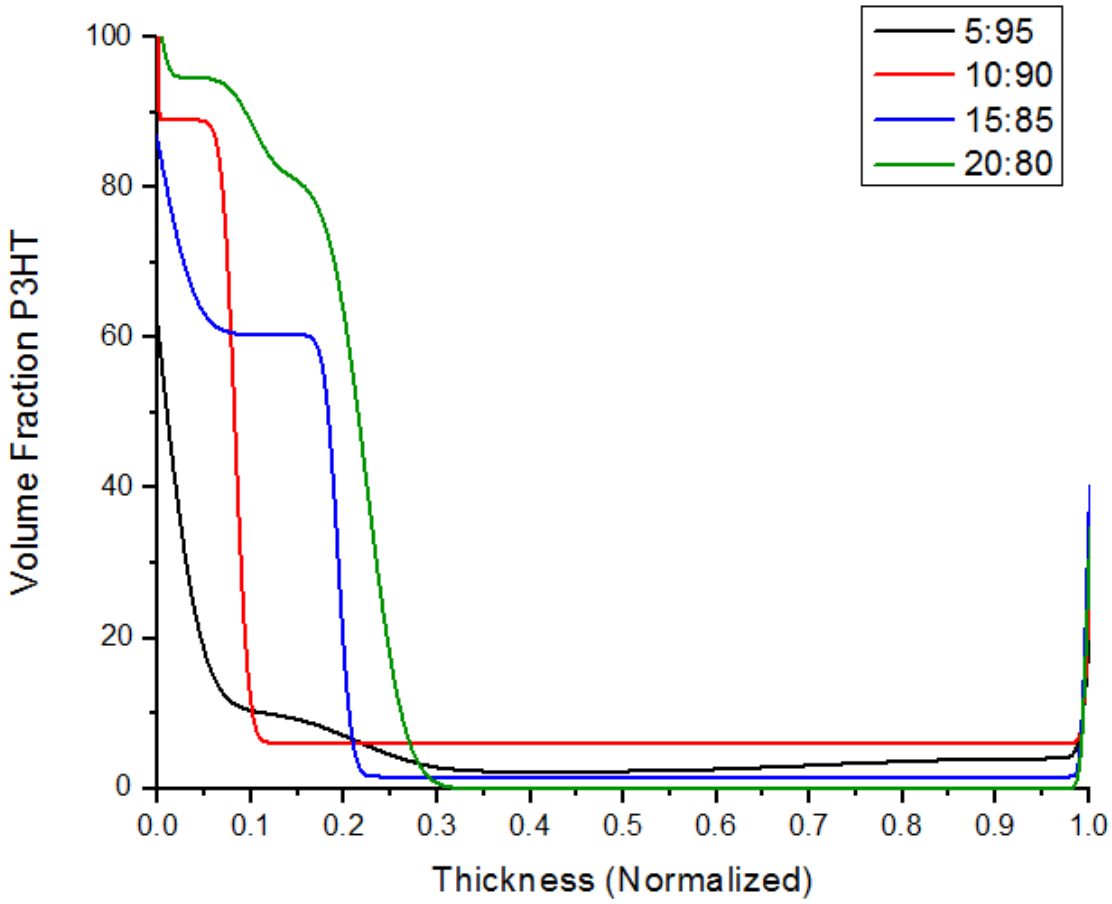


Figure 3.14 Plot of P3HT Volume Fraction Depth Profile for samples prepared with 131,500 g/mol at 52.4 rad/s as a function of blend composition 5:95 (black), 10:90 (red), 15:85 (blue), and 20:80 (green).

indicate that the entropic driving forces and the influence of the P3HT solubility compete in the stratification process, and to control the stratification of polymer blends, these two driving forces must be understood and controlled when films are prepared at slow casting speeds and long film formation times.

Conclusion

Polymer blend thin film depth profiles were obtained through neutron reflectivity experiments of spin cast P3HT/dPMMA blend thin films. The results presented in this paper indicate a hierarchy of driving forces that control the film vertical profile, where there appears to be a coupling of the thermodynamic and kinetic factors that influence film morphology. At high spin rates and thus films that are formed very quickly, the immiscibility of the blend is the dominant driving force in the stratification of the polymer blend. More specifically, the stratification of the components is driven by the relative surface energies of the polymers in the blend. As the casting speed decreases and film formation time increases, the immiscibility and surface energy contrast between the two polymers still drives the vertical stratification, but entropic driving forces, which are related to the relative molecular weight of the two polymers, become important in the stratification process. This competition of multiple factors manifests the most at the slowest casting speed and longest film formation times, where the polymer-polymer miscibility, relative surface energies, and entropy of the two polymers in the thin film simultaneously dictate the extent of stratification. Moreover, at these longer film formation times, the solubility limits of the two polymers in the pre-deposition solvent also play a role in the final film

structure. As the casting speed is decreased, the time between precipitation of the solid polymers from solution and the film completion increases. Once a polymer has reached its solubility limit during the casting process, further stratification of that polymer is now impeded.

The entirety of these results indicate that the dominant thermodynamic driving force driving the stratification of P3HT:dPMMA thin films is the immiscibility of the polymer blend. Yet by intelligently altering the kinetics and balancing the thermodynamic properties controlled by the polymer blend composition and polymer molecular weight, the extent of stratification and depth profiles can be tailored. Although these results isolate the relative importance of individual thermodynamic parameters, the results
reported here provide insight into the kinetic factors that couple to the important thermodynamic properties (entropy, enthalpy, solubility, miscibility) and impact the stratification of a polymer blend.

In these studies, the least amount of stratification was observed when the two polymers were the most miscible, which occurs for the blend containing the two smallest molecular weights. According to the results in this manuscript, to maximize the amount of stratification of a sample, as well as acquire a sharp interface between the stratified layers, the surface energy difference and variation in quantity of chain ends between the polymers should be maximized. However, it should be noted that for these P3HT:PMMA blends, the P3HT always has the lowest molecular weight and smallest surface energy. The conclusions outlined in this paper may be applied to other systems where the lowest

molecular weight polymer also has the smallest surface energy because these thermodynamic properties drive the polymer to the air interface. Additional experiments are required to understand the balance between surface energy and entropic driving forces in stratification of polymer blends where the lowest surface energy polymer has a significantly higher molecular weight.

Although these results monitored the behavior of P3HT:dPMMA, polymer blends that are suitable for organic transistors where a sharp interface is desirable, these results also provide a fundamental understanding of the coupling of thermodynamic and kinetic factors in the film formation process to create a less stratified film, for instance if a blend thin film that were to be used in bulk heterojunction devices. Moreover, this fundamental understanding provides insight that can be used to rationally design one step solution processing protocols of a multitude of polymer blends where the targeted stratification for the application is known.

Acknowledgements

The authors gratefully acknowledge the National Science Foundation (DMR-1409034 and DMR- 1808946) for support of this project. We acknowledge the support of the National Institute of Standards and Technology, U.S. Department of Commerce, in providing the neutron research facilities used in this work. A portion of this research used resources at the Spallation Neutron Source, a DOE Office of Science User Facility operated by the Oak Ridge National Laboratory.

Appendix

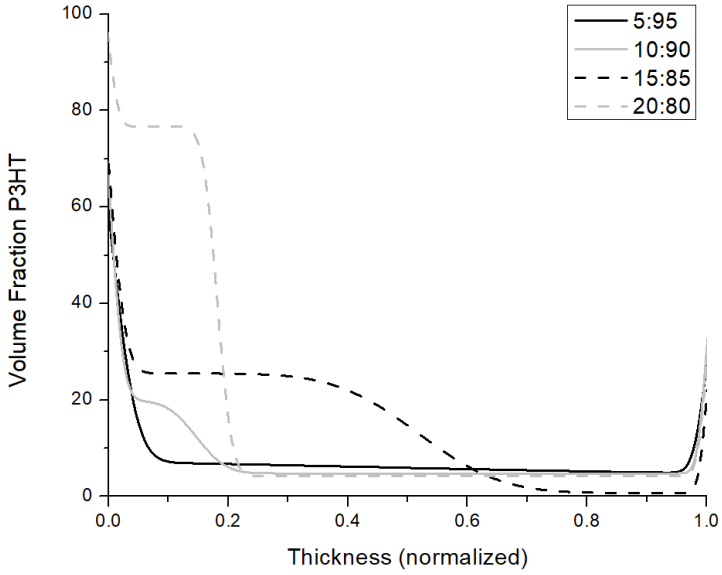


Figure 3.15 P3HT volume fraction depth profiles of P3HT:131,500 g/mol dPMMA 5:95 (solid black), 10:90 (solid grey), 15:85 (dashed black), 20:80 (dashed grey) blends spin cast from chlorobenzene at 209.4 rad/s where 0 is the air interface and 1 is the SiO2.

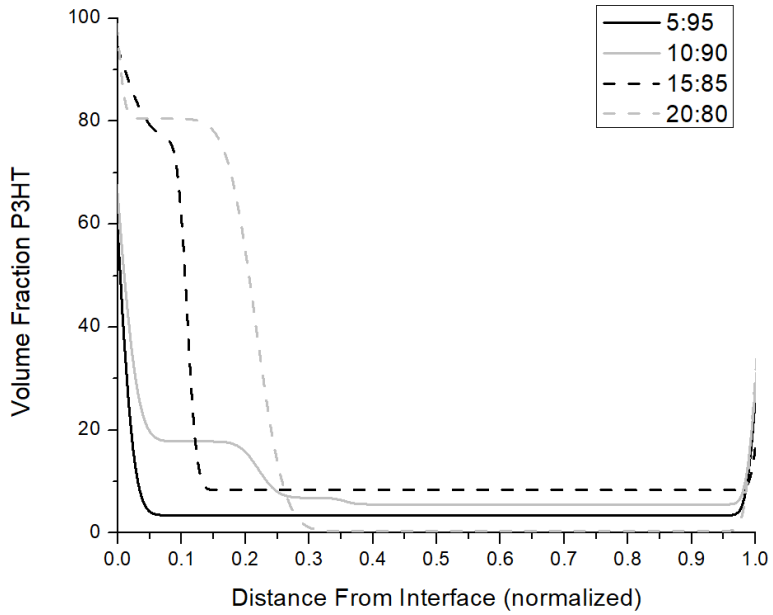


Figure 3.16 P3HT volume fraction depth profiles of P3HT:316,000 g/mol dPMMA 5:95 (solid black), 10:90 (solid grey), 15:85 (dashed black), 20:80 (dashed grey) blends spin cast from chlorobenzene at 209.4 rad/s where 0 is the air interface and 1 is the SiO2.

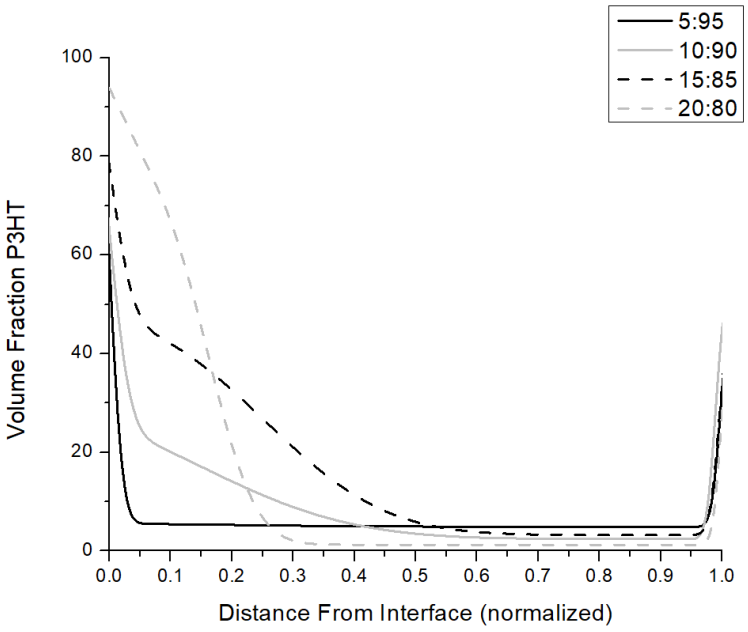


Figure 3.17 P3HT volume fraction depth profiles of P3HT:520,000 g/mol dPMMA 5:95 (solid black), 10:90 (solid grey), 15:85 (dashed black), 20:80 (dashed grey) blends spin cast from chlorobenzene at 209.4 rad/s where 0 is the air interface and 1 is the SiO2.

CHAPTER FOUR A 3-DIMENSIONAL ASSESSMENT OF THE LATERAL AND VERTICAL PHASE SEPARATION OF IMMISCIBLE POLYMER BLEND THIN FILMS

Abstract

Blends of conjugated and insulating polymers are of recent interest to improve the efficiency and durability of organic electronic devices such as field effect transistors. The necessary morphologies and appropriate crystalline length scales for effective electronic devices have been widely reported, in addition to the processing conditions necessary to fabricate effective devices. However, the processing conditions needed to elicit the required morphologies for effective device properties are often overlooked. The work presented in this chapter investigates the impact of polymer blend composition of poly(3-hexylthiophene-2,5-diyl) (P3HT) and deuterated poly(methyl methacrylate) (dPMMA) and spin cast speed on the 3-dimensional thin film blend morphologies. These processing conditions are correlated to the lateral and vertical film structures obtained by the careful analysis of Small Angle Neutron Scattering (SANS) and Neutron Reflectometry (NR) experiments, respectively.

Our results indicate specific control of the vertical and horizontal interfacial breadths, as well as the purity of each P3HT rich or dPMMA rich phase through simple changes in the processing conditions. An increase in the sharpness of the vertical interfaces in conjunction with a decrease in the horizontal interfacial breadth is observed when the spin cast speed is increased. Additionally, as spin cast speed decreases, the lateral phase contrast increases while decreasing the vertical phase contrast and phase purity. Increasing the concentration of P3HT in the blend increases the breadth of horizontal interfaces, while decreasing the breadth of the vertical interfaces.

Quick inspection of the SANS and NR data is counterintuitive where an increase in film formation time via a decrease in casting speed leads to decreased phase contrast in the lateral direction, but increased phase contrast in the vertical direction. A more thorough analysis reveals that vertical rearrangement of P3HT to the air interface, driven by entropy and the reduction of surface energy at the air interface, is the dominant directional phase separation during the spin casting process, relative to lateral phase separation of P3HT and dPMMA. As P3HT is driven towards the air interface, P3HT is thermodynamically driven to spread across the surface of dPMMA. The lateral spreading is monitored in the SANS experiment and manifests as an increase in phase size and a reduction in compositional contrast between domains as film formation time increases.

Introduction

Organic electronics have gained attention recently for their low-cost, flexibility, and simple processing.[76,89,92,93,128] Conjugated polymers are a common component in organic electronics as their inherent preference to align with a high degree of pi-conjugation orientation can enhance performance. However, on their own, conjugated polymers exhibit poor environmental and electronic stability over long periods of operation.[129,130] One method to combat this is the deposition of a conjugated polymer active layer with an insulating dielectric polymer from solution as a single step solution.[121] Combining these materials couples their advantageous properties and many times the electronic properties of a blended device exceeds the properties of a device consisting solely of the conjugated polymer.[131] This is often the case because blending during the

processing step results in an automatic self-assembly of the thin film during deposition referred to as self-stratification.[53,86,123,124] Self-stratification, a spontaneous thermodynamic process in which a film separates into layers in a film is used to streamline and lower costs in a range of thin film fabrication processes.[97,132]

The structures produced during self-stratification result in an increase in the quality of the interfaces between the active and insulating layers', which allows further exciton dissociation throughout the active layer.[133] The length scales of highly ordered regions and the qualities of the interfaces between them that are necessary for efficient device performance is well understood.[134] Moreover, the orientation of the insulating/conducting interface, i.e. whether it is perpendicular or parallel to the substrate, plays a key role in device efficiency.[135] Whether a sharp or broad interface is required is also device dependent; where a well-defined interface, or channel, parallel to the substrate is beneficial for field-effect transistors,[129] and any interface between an acceptor and a donor region, regardless of orientation, is preferred for photodiodes due to the importance of exciton separation.[136]

Many studies across a wide array of electronic devices have utilized blended materials and have confirmed improvement of device efficiency by changing the deposition conditions such as solvent, active or insulating polymer, substrate surface energy, or by introducing a post fabrication annealing step[56,131,137–139] Optimizing the processing conditions to obtained increased device performance shows that the processing conditions impact the final device structure. Unfortunately, a thorough understanding of the

correlation between final device structure and specific processing conditions is still lacking. Moreover, the in plane and out of plane structures of the thin film blend undoubtedly play a role in electron transfer throughout an active layer, yet the understanding and characterization of these structures is limited.[140]

The work presented in this chapter looks to bridge the gap between solution processing conditions and the final film structures that develop parallel and perpendicular to the substrate during the deposition process. By analyzing polymer blend thin films with neutron reflectivity and small-angle neutron scattering (SANS), the lateral and vertical morphology of the thin film can be determined. SANS and reflectivity offer orthogonal techniques to understand the 3-dimensional phase separation of the thin film blend, which is important as structures in either or both directions may contribute to the properties of the final film.[66,117] The polymer blend of interest is poly(3-hexylthiophene-2,5-diyl) (P3HT) and deuterated poly(methyl methacrylate) (dPMMA), bench mark organic materials used in field effect transistors.

The phase separation of P3HT and dPMMA can be attributed to the immiscibility of the blend, however, extensive vertical phase separation but limited lateral phase separation is needed to obtain effective devices.[74,81,90] Because of the impact morphology and directional phase separation has on device efficiency, the final film structures must be closely monitored as the processing conditions are changed. In this study, thin films are fabricated via single step spin casting from solution and the processing conditions of interest are blend composition and casting speed. The experiments presented here not only

utilize a single step process to streamline the film fabrication process, the results provide insight that will enable the control and engineering of lateral and vertical interfaces in many thin film blends simply by altering the processing conditions. This straightforward method to tailor final film morphology and structure presents opportunities for streamlined thin film fabrication regardless of the polymer materials.

Experimental

Chlorobenzene (Sigma Aldrich), d_5-chlorobenzene (Sigma-Aldrich), (Poly(3-hexylthiophene-2,5-diyl) (P3HT) (Ossila, regioregularity-95%, with number-average molecular weight (M_n) 19,500 g/mol and polydispersity index (PDI) 1.75), deuterated poly(methyl methacrylate-d_8) (dPMMA) (Polymer Source Inc., M_n (PDI), 316,000 g/mol (1.35)), protonated poly(methyl methacrylate) (PMMA) (Sigma-Aldrich, weight average molecular weight, M_w 350,000 g/mol) were used directly from the supplier and were not further purified.

Polymer blends were dissolved at 1 percent by mass in ratios of 5:95, 20:80 P3HT:dPMMA in chlorobenzene. These ratio annotations will be used throughout the paper to describe blend compositions. These solutions were dissolved by stirring at 55 °C overnight.

The Si wafers were cleaned in a piranha solution (1:3 ratio of sulfuric acid and hydrogen peroxide), washed with nanopure water, and allowed to sit under UV irradiation and ozone for 30 minutes. Thin films were prepared by spin coating the chlorobenzene solutions at a range of speeds (209.4 rad/s, 104.7 rad/s, 52.4 rad/s) onto Si wafers.

Neutron reflectivity experiments were conducted at the National Institute of Standards and Technology's Center for Neutron Research using the NG7 beamline with a Q range of 0.008-0.2 A^{-1} where $Q= 4\pi/\lambda \sin(\theta)$; λ is the neutron wavelength, and θ is the angle of incidence. The data for all incident angles was reduced utilizing the NCNR software.[99]

Small Angle Neutron Scattering (SANS) experiments were conducted at Oak Ridge National Laboratories at the High Flux Isotope Reactor using the General-Purpose SANS (CG-2) beamline. Three separate detector distances of 0.3, 2, and 12.5 meters with a wavelength of 6Å allowed a Q range of 0.0034 to 0.3363 $Å^{-1}$ where $Q = 4\pi/\lambda \sin(\theta/2)$, λ is the neutron wavelength, and θ is the scattering angle. Each sample was prepared as a thin film spin cast onto a Si wafer. This sample was then cut into 2x2 cm squares. Twelve of the cut samples were stacked and place in the scattering beam for analysis. Dilute solutions of P3HT in d_5-chlorobenzene (0.25 weight percent, 0.5 weight percent, 0.75 weight percent and 1 weight percent) and PMMA in d_5-chlorobenzene (1 weight percent, 1.5 weight percent, 2 weight percent, 2.5 weight percent) were prepared for a Zimm plot analysis. All raw data was normalized to detector dark current, detector sensitivity, and empty cell.

Results

The spin casting variables investigated in this paper are the casting speed and the blend composition. These parameters were selected to investigate the impact of both thermodynamic interactions (blend composition) and kinetic (casting speed) effects on the lateral and vertical phase separation of the blend in the cast film. We employ both neutron

reflectivity and SANS to determine the extent of phase separation in the vertical and lateral directions, respectively.

Vertical stratification was characterized with neutron reflectivity. Each sample's reflectivity curve was fit with a multi-layer model using IGOR and Motofit software packages.[100] The model fit provides the scattering length density (SLD) of the sample as a function of distance from the air interface. The model fit was verified for conservation of mass by verifying the model SLD is within 5% of the expected average SLD of the polymer blend based on the spin cast solution. Each SLD curve was transformed into a P3HT volume fraction profile using Equation 4.1:

$$\frac{SLD(z)-SLD_{dPMMA}}{SLD_{dPMMA}-SLD_{P3HT}} = \phi_{P3HT}(z) \qquad \text{Equation (4.1)}$$

where SLD(z) is the SLD of the sample at depth z, SLD_{dPMMA} is the SLD of dPMMA, SLD_{P3HT} is the SLD of P3HT, and $\varphi_{P3HT}(z)$ is the volume fraction of P3HT at depth z in the layer. The SLDs of P3HT and dPMMA were calculated from the NCNR SLD calculator and are estimated to be 0.7×10^{-6} A^{-2} and $6.6 \times 10^{-6} A^{-2}$, respectively. In addition, the thickness of each sample was normalized using the total film thickness from the neutron fit, where 0 is the air interface and 1 is the SiO_2 interface. The normalized film thickness allows for a comparison of all samples, regardless of casting speed or blend composition, parameters known to impact film thickness.[141]

Each P3HT volume fraction depth profile provides a horizontally average of the concentration of P3HT as a function of film depth (thickness) for each sample. To qualitatively compare each volume fraction depth profile, a P3HT rich layer represents the

layers in which the P3HT concentration exceeds the concentration of P3HT in the original polymer blend solution. For example, a P3HT rich layer in a sample deposited from a solution of P3HT:dPMMA 5:95 will have concentrations above 5% P3HT. This same definition is applicable for dPMMA rich layers.

Figures 4.1a and 4.1b show the P3HT volume fraction depth profiles of the cast 5:95 and 20:80 blends, respectively, as a function of casting speed. As observed in each Figure, the stratification varies with casting speed despite the fact all other processing conditions remain unchanged. The shape and relative thickness of the P3HT rich layer in all 20:80 samples (Figure 4.1b) are similar, where the breadth of the interfaces between the P3HT rich layer and the PMMA rich layer are sharp. Paradoxically, the samples prepared with 5:95 blends (Figure 4.1a), all have a gradual slope representing a broad interface between the P3HT rich layer and PMMA rich layer. It is difficult to determine the exact thickness of the P3HT rich phase in each spin cast sample prepared with 5:95 due to the breadth of this interface. Despite the difficulty in precisely locating the interface between the P3HT rich and PMMA rich phases, the normalized thickness of the P3HT rich layer is not drastically different among the samples prepared with 5:95 solution. For all samples prepared with 5:95, P3HT is found at the air interface with an increase in P3HT concentration in the P3HT rich layer at the air interface as the casting speed decreases.

The volume fraction depth profiles for samples prepared from 20:80 solutions (Figure 4.1b) display a drastic difference in the concentration of P3HT and the interface (air or Si) in which it resides; both properties are seemingly dependent on casting speed.

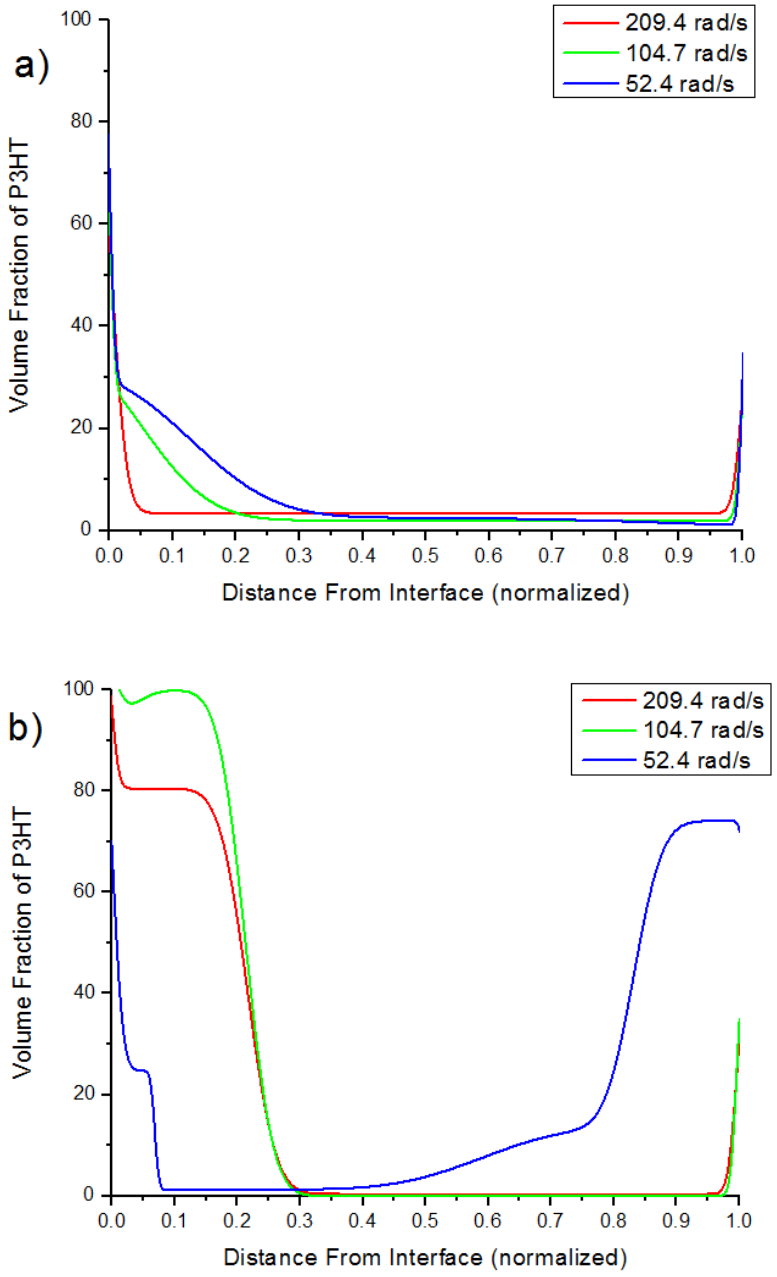


Figure 4.1 P3HT volume fraction depth profiles for P3HT:dPMMA (a) 5:95 and (b) 20:80 cast from chlorobenzene at 209.4 rad/s (red), 104.7 rad/s (green), and 52.4 rad/s (blue) where 0 is the air interface and 1 is the SiO2 interface.

The sample prepared at 209.4 rad/s exhibits a reduced concentration of P3HT in the P3HT rich layer relative to the samples prepared at 104.7 rad/s, yet the sample prepared at 52.4 rad/s has the smallest concentration of P3HT in the rich layer relative to the other two casting speeds. The P3HT rich layer of the two samples prepared at 52.4 rad/s, 20:80 and 5:95, are located at the air and Si interfaces, respectively. The 20:80 sample prepared at 52.4 rad/s is the only sample in this set where the P3HT rich layer is at the Si interface.

To quantify and compare the degree of stratification for each sample, a previous analytical method was employed.[127] This method defines limits to describe the extent of stratification in a final film. First, a theoretical completely stratified sample is represented by two layers of pure P3HT and dPMMA and second, a homogenous thin film is defined as a constant concentration of P3HT throughout the entire thickness of the film. These limits provide the baseline limits to quantify the stratification of different samples regardless of processing conditions as described in our previous work.[127] This protocol was utilized for each of the samples in Figures 4.1a and 4.1b and the extent of stratification for each sample is displayed in Figure 4.2. At each spin speed utilized, the extent of stratification is larger in samples with 20% P3HT relative to the samples with 5% P3HT. For the samples prepared with 5:95 solutions, there is a small increase in extent of stratification as the spin speed decreases. On the other hand, samples containing 20:80 show a small increase in extent of stratification as the spin speed decreases from 209.4 rad/s to 104.7 rad/s, but a drop of the extent of stratification occurs when the spin speed is decreased further from 104.7 rad/s to 52.4 rad/s where the extent of stratification is the

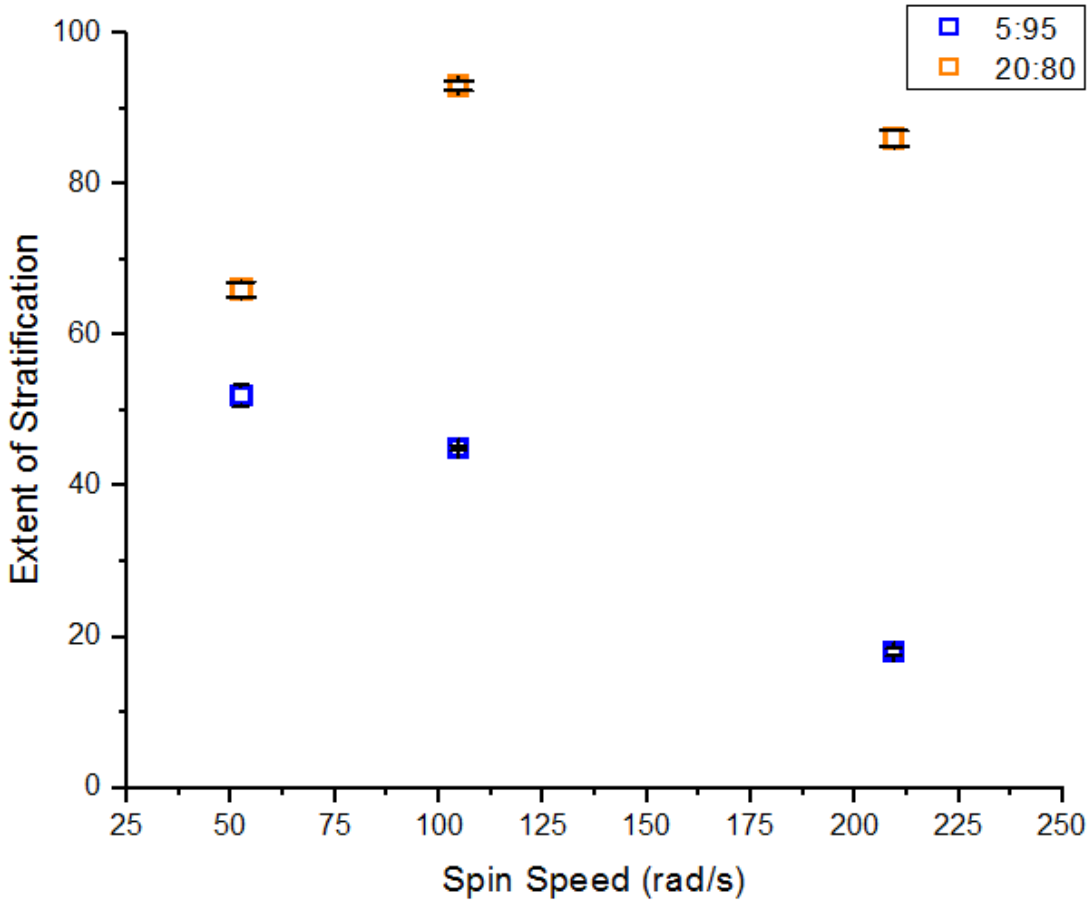


Figure 4.2 Plot of extent of stratification as a function of spin speed, and blend composition, P3HT:dPMMA 5:95 (blue squares) and 20:80 (orange squares).

smallest of all three casting speeds.

The lateral phase separation of the thin films was determined by the analysis of the SANS curves. The resultant SANS curves for all samples P3HT:dPMMA 5:95 and 20:80 prepared at 209.4 rad/s, 104.7 rad/s, and 52.4 rad/s are displayed in Figure 4.3. To account for differences among film thicknesses, all sample curves were reduced to the thickness of the P3HT:dPMMA thin film. Before fitting any thin film sample, the scattering of the blank silicon wafer was fit to the non-homogenous solid Debye-Anderson-Brumberger (DAB) model as shown in Equation 4.2.[142]

$$I(q) = \frac{A*\alpha^3}{[1-(q*\alpha)^2]^2} \qquad \text{Equation (4.2)}$$

The scattering of the thin film was then fit to a sum of two solid DAB models, one that accounts for the scattering of the Si wafer and one that accounts for the scattering of the phase separated thin film blend. Each DAB model provides a correlation length (α), in Angstroms, representing the average distance between phases, and a scale factor (A). Although the scale factor is an individual fitting parameter, it is directly proportional to the SLD contrast between the two phases ($\Delta\rho$) and their respective volume fractions (ϕ_1, ϕ_2) as described in Equation 4.3:

$$A = 8\pi(\Delta\rho)^2\phi_1\phi_2 \qquad \text{Equation (4.3)}$$

The scale factor (A) that emerges from the fits of each thin film blend was divided by $8\pi*10^8$ to offer a quantity that represents the phase contrast between the phases and the volume fractions of each phase. This new scale factor is now defined as Σ*. All SANS curves were fit using the NCNR SANS analysis macros in Igor Pro.[143] Figure 4.4 displays

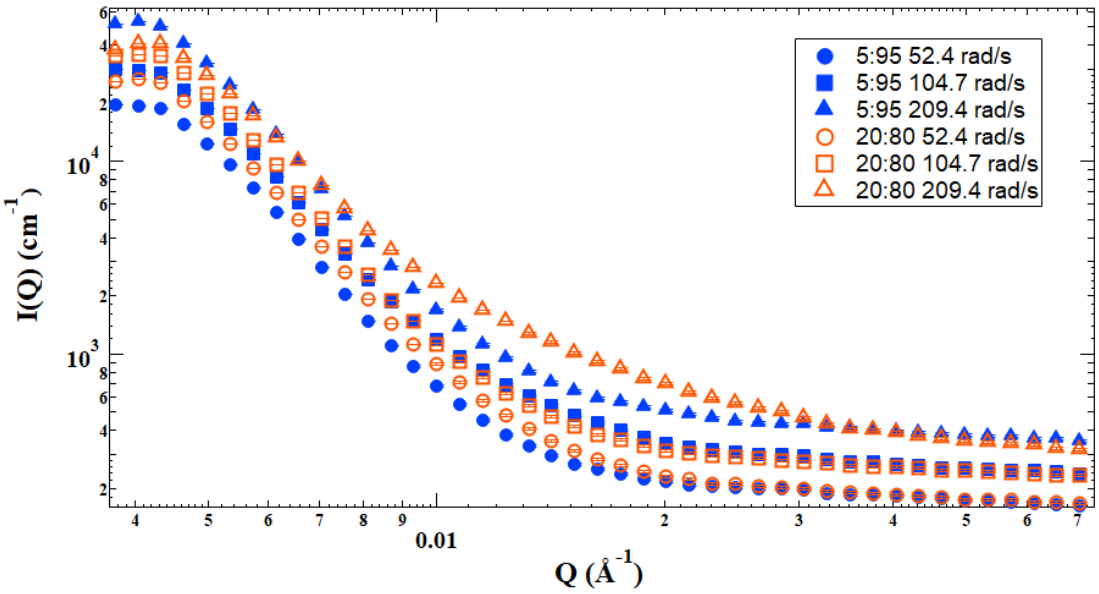


Figure 4.3 Small-angle neutron scattering curves of P3HT:dPMMA 5:95 (blue closed shapes) and 20:80 (orange open shapes) prepared at 209.4 rad/s (triangles), 104.7 rad/s (squares), and 52.4 rad/s (circles).

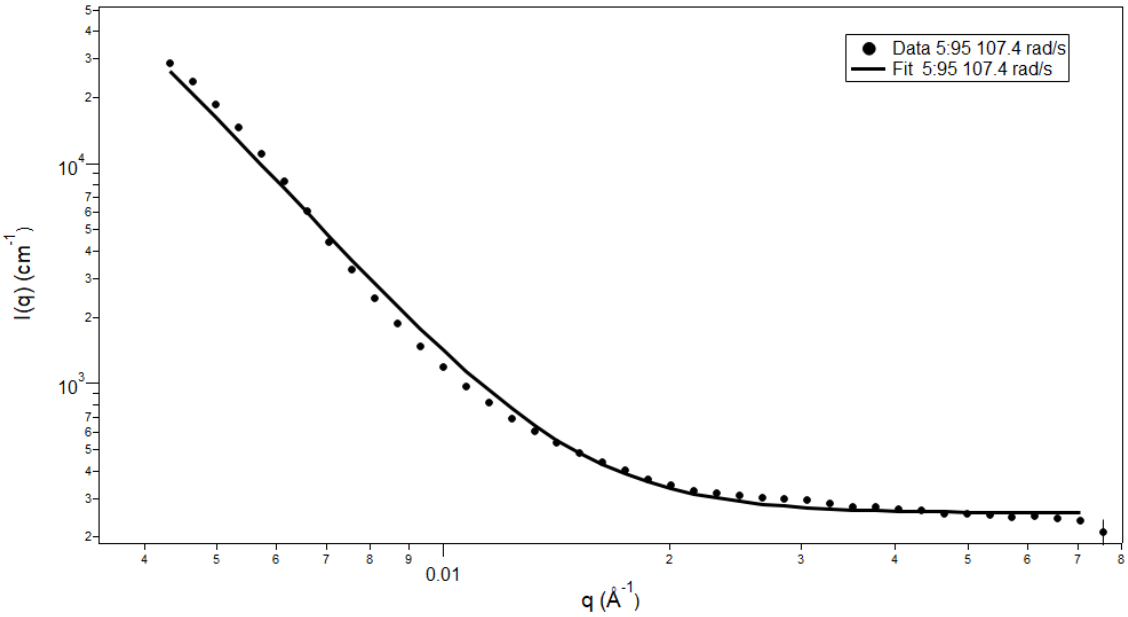


Figure 4.4 DAB model fit (black trace) for a P3HT:dPMMA 5:95 sample prepared at 107.4 rad/s.

the data, an example fit and the residuals for the thin film blend prepared from a 5:95 solution cast at 52.4 rad/s. Similar, excellent agreement for all fits were observed over the entire Q-range.

Figures 4.5 and 4.6 provide the change in the correlation length (Figure 4.5) and Σ* (Figure 4.6) as a function of casting speed and blend composition. The correlation length of each phase is larger for samples containing 20:80 than samples containing 5:95 at each casting speed. As the casting speed decreases, the correlation length increases from 502 Å to 845 Å for samples containing P3HT:dPMMA 5:95. The 20:80 samples, on the other hand, do not exhibit as drastic of an increase of correlation length as casting speed decreases, where the correlation length for these samples remains around 1000 Å.

Figure 4.6 illustrates the Σ*, which is proportional to the amount of contrast between the coexisting phases, as a function of casting speed. The phase contrast increases with increasing casting speed regardless of blend composition. Additionally, an increase in P3HT concentration at the same casting speed results in an increase in the phase contrast. Although the samples prepared with solutions of 20:80 always have a larger phase contrast relative to the samples prepared with 5:95 solutions, the differences in phase contrast between the two blend compositions are much larger when samples were prepared at 209.4 rad/s relative to the samples prepared at 52.4 rad/s.

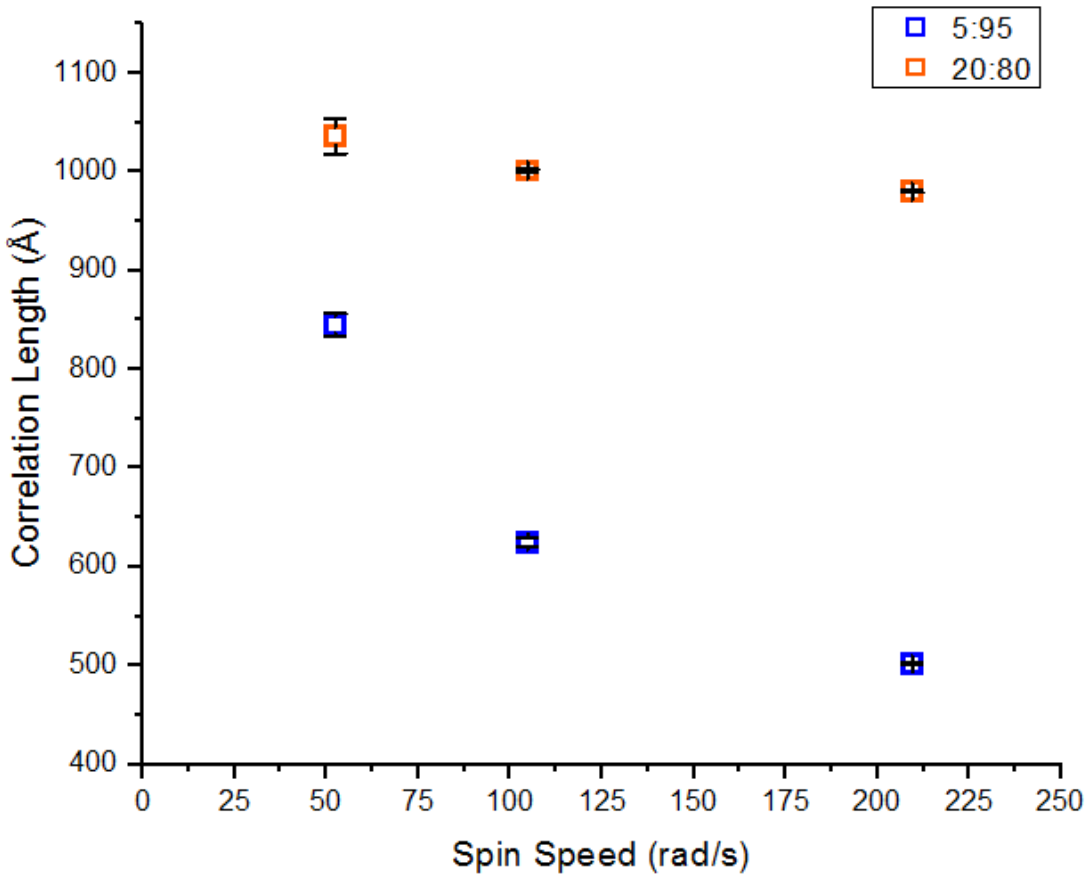


Figure 4.5 Plot comparing correlation length derived from the model fits for both P3HT:dPMMA compositions 5:95 (blue squares) and 20:80 (orange squares) as a function of spin speed.

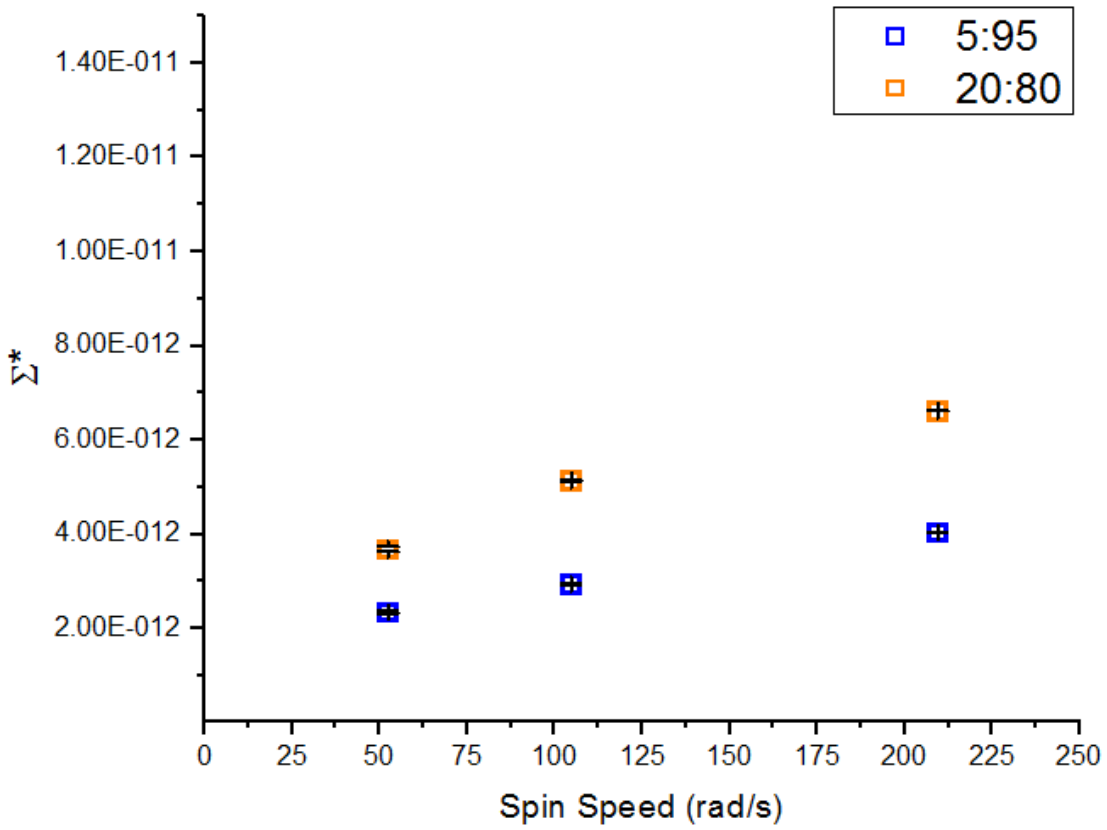


Figure 4.6 Plot comparing Σ* for both P3HT:dPMMA compositions 5:95 (blue squares) and 20:80 (orange squares) as a function of spin speed.

Discussion

Neutron Reflectivity

The dependence of extent of stratification on casting speed differs from that of its dependence on blend composition. Recent studies define the process of stratification to be driven by the difference in the surface energy of the two blended materials.[74] However, the surface energy difference alone does not explain the drastic variation in the P3HT volume fraction depth profiles for the samples investigated in this report. Figures 4.1a and 4.1b illustrate the changes in vertical ordering observed by changing either P3HT loading or casting speed. Samples prepared with 20:80 solution blends, regardless of spinning speed, are richer in P3HT in the stratified layers relative to the samples prepared from the 5:95 samples. This result agrees with previously reported results where the stratification is driven by the immiscibility of P3HT and dPMMA.[127] As the amount of P3HT increases, the immiscibility of the blend also increases. Equation 4.4 calculates the critical composition (ϕ_c(A)) of P3HT, where N_A is the degree of polymerization of (~20,000 g/mol) P3HT and N_B is the degree of polymerization of dPMMA (316,000 g/mol), which gives Φ_c (P3HT) = 0.85

$$\phi_c(A) = \frac{\sqrt{N_B}}{\sqrt{N_A}+\sqrt{N_B}} \qquad \text{Equation (4.4)}$$

All examined blend compositions contain concentrations of P3HT significantly smaller than the calculated critical P3HT concentrations. However, as the concentration of P3HT in the blend increases and approaches the critical concentration, the polymer blend

becomes more immiscible. Thus, the thin films fabricated from solutions comprised of 20% P3HT phase separate more strongly than the stratified layers fabricated from solutions comprised of 5% P3HT.

The smaller surface energy of P3HT relative to dPMMA[65] drives the P3HT towards the air interface.[56] In all samples, except for the sample cast from a 20:80 blend solution at 52.4 rad/s, P3HT is found at the air interface. Previously reported results indicate that solutions with high concentrations of P3HT prepared at slow casting speeds result in P3HT precipitating before the PMMA, due to the poor solubility of P3HT in the casting solvent, chlorobenzene. The solubility limits for PMMA and P3HT in chlorobenzene, originally reported in Chapter 3, are re-reported in Table 4.1. The precipitation of P3HT prior to the complete evaporation of chlorobenzene leads to the formation of a P3HT rich layer at the Si interface.

In the 20:80 thin film blend prepared at 52.4 rad/s, a thick, highly concentrated P3HT rich layer is found at the Si interface while a thin P3HT rich layer is also found at the air interface. The early precipitation of P3HT explains the P3HT rich layer at the Si interface, yet the P3HT layer at the air interface indicates the thermodynamic forces driving P3HT to the air interface are not completely inhibited by the precipitation of P3HT. This segregation of the P3HT to both the air and Si surface results in a lower extent of stratification than 20:80 films formed at other spin speeds. Arguably, the presence of two P3HT rich regions represents a more phase separated system relative to a film with only one P3HT rich region. Overall, however, neutron reflectivity reveals *increased vertical*

Table 4.1 Solubility limits of the polymers studied in this chapter.

Sample	Solubility in chlorobenzene (mg/mL)
350 kg/mol PMMA	198.5 ± 10.9
20 kg/mol P3HT	15.67 ± 0.40

stratification with *reduced casting speeds* and *increased P3HT concentration*.

Small-Angle Neutron Scattering

Figures 4.5 and 4.6 show the correlation length and Σ*, respectively for both blend compositions as a function of casting speed. The correlation length, interpreted as the average phase size, is larger for the 20% P3HT samples relative to that of the 5% P3HT samples, regardless of casting speed. Additionally, the size of the phase domain increases as casting speed decreases for samples containing P3HT:dPMMA 5:95 from 502 Å, to 625 Å, to 845 Å as the casting speed decreases. The samples containing the 20:80 blend exhibit relatively consistent correlation lengths (~1000 Å) for all casting speeds.

It has been reported that the solubility of the polymers in the casting solvent play a role in thin film structure, where transistors fabricated from spin cast P3HT perform more efficiently when P3HT has a higher solubility in the casting solvent.[144–146] The efficiency of the device is ascribed to an increase in the size and quantity of π-π stacked crystalline areas.[81] Moreover, one method to quantify solvent quality is to determine the radius of gyration (R_g) of the polymer in casting solvent.[104] The radii of gyration of both polymers dissolved in chlorobenzene are reported in Table 4.2. The correlation lengths of the phase separated thin film blends are larger than the R_g for either P3HT and PMMA. This indicates that the domain sizes derived from the DAB model fit to each SANS curve consist of multiple chains and are not single chain polymer domains.

Figure 4.6 plots the Σ* for each blend composition as a function of casting speed. Recall that the Σ* is a representation of the compositional contrast between the two phases

Table 4.2 The radii of gyration for PMMA and P3HT in chlorobenzene obtained via Zimm analysis with SANS.

Material	Radius of Gyration (chlorobenzene)
PMMA 316 kg/mol	213 Å
P3HT 19.5 kg/mol	101 Å

the two-phase system. Because the Σ* has multiple components: two volume fractions and the SLD contrast squared, it is non-trivial to interpret the Σ*. Qualitatively, a smaller Σ* value represents a more homogenous lateral phase distribution lacking lateral phase separation, while a larger Σ* value represents a more phase separated system in the lateral direction. Because the Σ* values in Figure 4.6 decrease as spin speed decreases, it is clear that the samples become more homogenous laterally with increased film formation time.

Figure 4.6 reveals that an increase in P3HT concentration increases the lateral phase contrast for each spinning speed. The domain compositional contrast increases as the concentration of P3HT increases because of the inherent enthalpic polymer-polymer interactions in the blend. Figure 4.6 also shows that samples prepared at the fastest casting speed, 209.4 rad/s, result in larger phase contrast than samples prepared at the slowest casting speed, 52.4 rad/s, regardless of the blend composition. Spin speed is directly related to film formation time and therefore the amount of time a polymer can rearrange before all solvent evaporates and the film is formed.[127] As the casting speed decreases, film formation time increases, and the phase contrast decreases.

Therefore, the results obtained from NR reveal that an *increase in P3HT concentration* and *decrease in casting speed* elicits *increased* vertical phase separation. The results obtained from SANS, however, indicate *increased* lateral phase contrast with *increased P3HT concentration* and an *increase in casting speed*. Increasing the P3HT concentration in the blend leads to an increase in phase size while an increase in casting speed decreases the average phase size. Translating the set of results as a function of

increased film formation time shows that during film formation, the average phase size increases and the composition difference between the phases decreases with longer formation time.

3D Assessment of Final Film Structure

When constructing a comprehensive story that holistically explains the results obtained from both characterization methods, it is important to remember that each data set corresponds to a specific sample orientation. To emphasize the respective orientations of neutron reflectivity and small angle neutron scattering, a schematic illustration of each method is shown in Figure 4.7. In neutron reflectivity, the reflection is only sensitive to contrast that occurs in the vertical direction while averaging the scattering over the lateral foot print of the beam. On the other hand, during a neutron scattering experiment, the sample substrate is positioned normal to the neutron source and remains stationary for the duration of scattering collection. This orientation provides the compositional and phase information in the lateral directions of the thin film, averaging over the thickness of the sample.

The NR and SANS results may at first glance appear contradictory. A decrease in casting speed, when the samples are measured with neutron reflectivity, results in an increase in vertical phase separation, while when the samples are measured with SANS, a decrease in casting speed results in a decrease in lateral phase separation. To provide a possible explanation for this discrepancy, Figure 4.8 illustrates potential thin film morphologies from the perspective of each characterization method that are consistent with

the observed results. In Figures 4.8a-4.8c, as casting speed decreases, vertical stratification increases where P3HT (depicted by the purple region) is driven towards the air interface, and the P3HT region broadens as a function of decreased casting speed. The illustrations for small angle neutron scattering (4.8d-4.8f) show the lateral phase size growing as a function of decreased casting speed, and the definition between phases becomes broader. Additionally, the contrast between phases decreases as casting speed decreases.

The data collected for each characterization method is an average over the orthogonal direction that it is monitoring. Thus, the presence of a pure phase in one direction may not be detected by the measurement collected in the orthogonal direction. For example, if there is a pure P3HT layer parallel to the substrate measured with reflectivity, it will not contribute to the lateral contrast measured with small angle scattering. Furthermore, a mixed layer parallel to the substrate measured with reflectivity are the *dominant* regions of the film detected by small angle scattering because these are the regions that contain lateral distribution of both polymers. If Figures 4.8a-4.8c (neutron reflectivity samples) are used as a guide, the size of these mixed regions that are sensitive to small angle scattering decreases with a decrease in spin speed. The size of the regions in Figures 4.8a-4.8c sensitive to SANS (denoted as the light purple gradient between pure purple and pure white regions) are reduced for samples prepared at 52.4 rad/s relative to samples prepared at 107.4 rad/s and further reduced relative to samples prepared at 209.4 rad/s. This indicates a possible explanation for the Σ^* decrease as a function of casting speed. P3HT rich layers organize at the air interface during film formation. As the

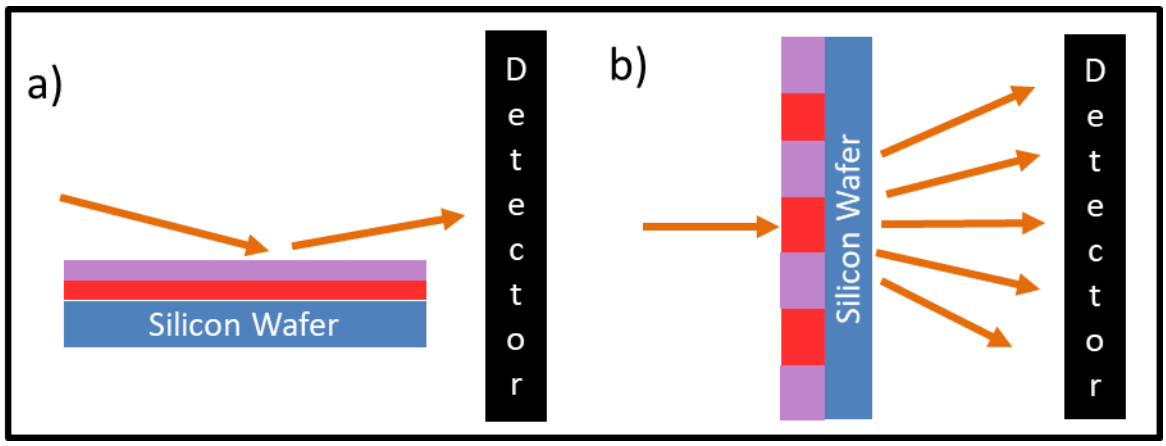


Figure 4.7 Schematic depiction of thin film orientation during both Neutron Reflectivity (a) and Small Angle Neutron Scattering (b) measurements. The orange arrows represent the path neutrons take before and after they hit the sample.

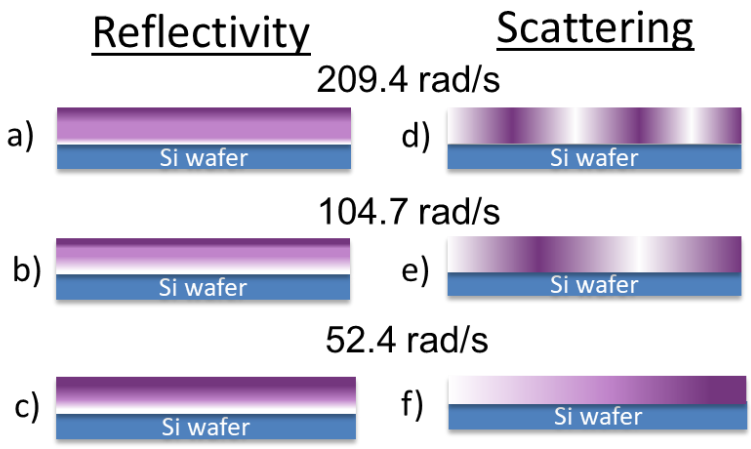


Figure 4.8 Schematic depiction of vertical and lateral phase separation. Illustrations are representations of reflectivity (a, b, c) and small angle neutron scattering (d, e, f) samples collected at 209.4 rad/s, 104.7 rad/s, and 52.4 rad/s, respectively.

concentration of P3HT increases at the air interface, the concentration of P3HT in the broad P3HT:dPMMA interface decreases. The reduced concentration in a smaller region of the film sensitive to small angle scattering manifests as a decrease in the lateral phase contrast in the SANS data.

Another possible explanation for the discrepancy between the decreased phase contrast in the lateral direction as casting speed decreases, and an increased vertical stratification with decreased casting speed is the thermodynamic spreading of P3HT throughout film formation. The Young-Dupré Spreading Coefficient (Equation 4.5) provides insight to whether two liquids with different surface energies will spread or wet one another. In Equation 4.5, *S* is the spreading parameter, γ_a is the surface energy of liquid *a* or the bottom liquid, γ_b is the surface energy of liquid *b* or the top liquid, γ_{ab} is the surface energy of the interface between liquid *a* and liquid *b*.[147]

$$S = \gamma_a - (\gamma_b + \gamma_{ab}) \qquad \text{Equation (4.5)}$$

If *S* is positive, thermodynamic spreading is favored and if S is negative, spreading will not occur. To encourage spreading of liquid *b* onto liquid *a*, it is required that liquid *b* have a smaller surface energy relative to liquid *a*. For our case, solvated P3HT is the top liquid (liquid *b*) (thermodynamically driven to the air interface), while solvated dPMMA is the bottom liquid (liquid *a*). P3HT (liquid *b*) has a smaller surface energy and is thermodynamically driven to spread over dPMMA. This spreading process is consistent with both the vertical stratification measured with neutron reflectivity and the decreased phase contrast and increased domain size measured with small angle neutron scattering.

Overall these results indicate that vertical stratification, driven by surface energy and polymer-polymer interaction parameters, dominates over lateral phase separation because in addition to thermodynamics driving vertical phase separation, thermodynamic lateral spreading is also favored for this system.

It is important to note that although thermodynamics explain the trends observed in this data, it should be noted that this spreading does not always occur. Many polymer blend studies utilize thermal annealing to attain desired structures. During the annealing step, the polymers rearrange to decrease the interfacial area[148] which may form spherical structures in the lateral direction. We hypothesize that this also would be the case if the two polymers did not have such a large surface energy bias.

Conclusion

Small-angle neutron scattering and neutron reflectivity have been combined to probe the effects of spin casting speed and blend composition on the lateral and vertical phase separation of P3HT:dPMMA blends. The phase separation was analyzed by coupling vertical polymer depth profiles from neutron reflectivity to horizontal phase size and phase contrast provided from analysis of SANS data. These results provide insight into processes that control phase separation to fabricate films with desired depth and lateral profiles. In most cases, P3HT was found at the air interface. The only time the P3HT rich layer was not measured at the air interface was under conditions of increased P3HT concentration in the blend film and slow casting speed where the solubility limit of P3HT appears to play a role in film fabrication. Increasing the P3HT concentration in the blend leads to sharp

horizontal interfaces and increased lateral phase sizes and contrast. Increasing the film formation time by decreasing the spinning speed leads to an increase in the size and concentration of the P3HT rich horizontal layer, and an increase in the size of the lateral phases while reducing the lateral phase contrast. This three-dimensional structural analysis holds promise to benefit the fabrication of active layers in devices as it provides fundamental insight into the correlation between processing conditions and 3-dimensional thin film structure, which is critical to optimize electronic performance.

All results discussed here demonstrate that processing conditions impact the kinetics and thermodynamics that drive phase separation in the lateral and vertical directions. Although blends consisting of P3HT and dPMMA, typically studied for their application in field effect transistors which require sharp horizontal interfaces, were studied here, the overall conclusions relating bi-directional phase separation to processing condition can be extended to other systems that require specific vertical or lateral interfacial conditions. The direct control of lateral and vertical thin film morphology from spin casting allows for direct design of interfaces for a wide range of applications simply by altering the processing conditions. Therefore, this research holds promise to streamline the process of fabricating efficient, durable devices and materials without post-modification of the material.

Acknowledgements

The authors gratefully acknowledge the National Science Foundation (DMR-1409034 and DMR-1808946) for support of this project. We acknowledge the support of

the National Institute of Standards and Technology, U.S. Department of Commerce, in providing the neutron research facilities used in this work. A portion of this research used resources at the High Flux Isotope Reactor, a DOE Office of Science User Facility operated by the Oak Ridge National Laboratory.

CHAPTER FIVE IMPACT OF SUBSTRATE RIGIDITY ON THE COMPOSITION AND DENSITY OF FUNCTIONAL MULTILAYER FILMS

Abstract

Polymeric substrates have become increasingly important in the recent drive in technology to produce flexible displays and mechanically adaptable devices. Multi-nanoscale layer coatings are often necessary for specific device applications and these complex coatings are often fabricated by sputtering onto the substrate. Correlating fabrication conditions to bi-layer structure and performance is currently investigated by monitoring microstructure via x-ray diffraction, and microscopy, but these techniques do not provide an understanding of interfacial structure between subsequent layers. The work presented here investigates the impact of depositing increasingly thick bi-layer films of indium tin oxide (ITO) and tungsten (W) on flexible (Poly(ethylene terephthalate) (PET)) and rigid (silicon) substrates by utilizing complimentary characterization methods of x-ray and neutron reflectivity and grazing incidence x-ray scattering to study the depth profiles and interfacial structure. Sputtering a W layer onto ITO that resides on a silicon substrate increases the density of the supporting ITO layer as the thickness of the W layer increases. Interestingly, an increase in the thickness of ITO leads to a decrease in density and compositional changes, which are dependent on the supporting substrate. Additionally, the interlayer interfaces of the multilayer on PET broaden relative to those in the multilayer that is on the silicon substrate. The compositional, density, and interfacial structure fluctuations are attributed to the difference in rigidity/hardness between the two substrates and the role of substrate rigidity on the sputtering process. This fundamental study defines the influence of substrate properties on coating composition, density, and interfacial

structure; all of which play important roles in the application specific properties and function of the targeted bi-layers.

Introduction

Multi-layer thin films deliver performance, durability, and desired aesthetics by incorporating properties of many components into a single applied finish for various applications and function.[44,149] The ability to devise multi-component thin films leads to efficient production of complex devices, including touch screens and 'smart' windows.[150,151] Transparent and conductive materials such as tin doped indium oxide (ITO) are important in the current evolution of such multi-layer films, including in the realm of liquid crystal displays (LCDs).[152,153] LCDs are used in a wide array of applications from computer monitors, flat screen televisions, telephones, and automobile displays. ITO is the most widely used transparent conductor in LCDs because it has the best performance in conductivity, transmission, and stability.[154] The inherent properties of ITO are enhanced by incorporating additional metals such as Ag, Cu, Ga, and Cd which alter the bandgap of the material and in turn enhance the conductivity and indirectly the transparency of the films.[155,156] ITO is traditionally fabricated onto rigid substrates such as glass or silicon which are suitable for a range of applications. However, such inflexible substrates have significant drawbacks such as non-transparency, rigidity, cost, and brittleness when developing new technology that require flexible smart materials.[157]

Conjugated polymers are an attractive alternative to metal-based semiconductors because of the synthetic tunability, ease of processing, and flexibility, however, the

electrical efficiency does not match metal-based semi-conductors.[158] ITO and other oxide compounds are favorable as electrodes over crystalline polymers because of the ability to fabricate thin films at room temperature while maintaining the required mechanical stability and compositional uniformity.[153] Room temperature processing is essential for flexible substrates which lose their optical clarity and surface smoothness at higher temperatures.[159] Poly(ethylene terephthalate) (PET) is widely used as a flexible substrate in place of silicon for ITO thin films.[160,161] ITO is typically mechanically sputtered onto PET substrates resulting in materials with moderately high mobilities.[162] Transitioning to a polymer based substrate like PET not only opens the door for flexible electronics, but is also advantageous because the polymer substrate provides flexibility, is light weight, has low cost, and high durability.[163,164]

Additionally, scaling up thin film fabrication methods from typical benchtop scale device fabrication, such as spin-coating, to industrially scaled roll-to-roll processing makes assembly of large-scale devices more efficient.[165] The research regarding the expansion of applications capable of utilizing ITO on various substrates focuses on optimizing the electron mobility, electrical resistivity, mechanical stability, and the overall optical transmittance of the ITO film.[166] Oftentimes, the structure or overall depth profile of the fabricated thin film is overlooked though the correlation between the structure of conductive materials, as well as the sharp interface necessary for the desired electrical properties are known.[167]

The aim of the current study is therefore to investigate the fabrication of ITO and tungsten (W) sputtered thin films onto both flexible and rigid substrates, and more specifically, determine the impact of the supporting substrate on the depth profile of the deposited films and the interfacial structure between sputtered layers. The structure of the interface is determined by neutron and x-ray reflectivity and grazing incidence x-ray scattering. The reflectivity methods provide compositional and density dependent depth profiles of the thin films while grazing incidence x-ray scattering provides information on the lateral organization and horizontal interfacial quality of the thin films. The information provided by these experiments offer insight into the impact of substrate rigidity on interfacial structure, sputtering film thickness limitations, and provide an additional method to correlate the processing of the sputtered films to the respective electronic properties by understanding the structure of the multilayer films.

Experimental

Indium Tin Oxide (ITO), Tungsten (W), Poly(ethylene terephthalate) (PET), and silicon (Si) were used directly from the supplier. Bi-layer films comprised of ITO (25 and 50 nm) and W (0, 10 and 20 nm) coatings were sputtered onto PET and Si substrates. The ITO layers are deposited directly onto the substrate and if there is a W layer, it is deposited onto the ITO layer. An illustration of the thin film orientation is provided in Figure 5.1.

ITO was sputtered with gas flow 10 sccm (4 sccm of 10% oxygen in Argon, 6 sccm Argon) which in this process equates to a pressure ~10 mTorr. The power was set to 61 watts with a fixed current (~180 mA) and voltage (~340 V). W was sputtered with a gas

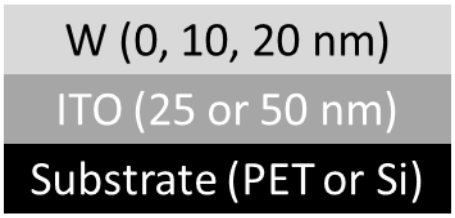


Figure 5.1 An illustration of the thin film orientation where the ITO layers were sputtered directly onto the substrate and W layers were sputtered onto ITO.

flow of 10 sccm Argon which in this process equates to a pressure ~10 mTorr. The power was set to 41 watts with a fixed current of (~100 mA) and voltage of (~400 V).

The bi-layer coatings were characterized with neutron reflectivity, x-ray reflectivity, and grazing incidence x-ray scattering. Neutron reflectivity experiments were conducted at the National Institute of Standards and Technology's Center for Neutron Research (NCNR) using the NG7 beamline and a Q range of 0.008-0.2 A^{-1} where $Q= 4\pi/\lambda \sin(\theta)$; λ is the neutron wavelength, and θ is the angle of incidence. The data for all incident angles was reduced utilizing the NCNR software.[99]

X-Ray reflectivity experiments were conducted at the National Institute of Standards and Technology's Center for Neutron Research (NCNR) using the Bruker D8 Advance in the reflectometry configuration with a Q range of 0.02-0.25 A^{-1}. The data for all incident angles was reduced utilizing the NCNR software.[99]

Grazing Incidence X-Ray scattering experiments were performed at the Duke University Shared Materials Instrumentation Facility using the SAXSLab Ganesha which has a 0.154 nm source. The grazing incidence configuration was used with a fixed angle of incidence (α_i) of 0.2°. The instrument was calibrated to a silver behenate standard for accurate analysis. Each data set was stored as a TIFF detector image. Each image was converted from pixels into 2θ (in-plane diffraction angle) and α (out of plane diffraction angle) coordinates. Equations 5.1 and 5.2 were used for the calculation of (α, 2θ) where p_s is the pixel size (0.172 mm), d is the sample to detector distance (1041 mm), and (x_c,y_c) is the coordinate of the beam center in pixels.

$$2\theta = \frac{180}{\pi} tan^{-1}(\frac{(y-y_c)p_s}{d}) \quad \text{Equation (5.1)}$$

$$\alpha = \frac{180}{\pi}(tan^{-1}\left(\frac{(x_c-x)p_s}{d}\right) - \frac{\pi\alpha_i}{180}) \quad \text{Equation (5.2)}$$

Results

Neutron and X-ray Reflectivity

Due to the importance of the layer composition and density as well as the interfacial structure between different layers in sputtered thin films, the depth profile analysis was determined using both neutron and x-ray reflectivity. Regardless of the source, reflectivity measurements provide a normalized reflection profile as a function of incident wave vector, Q. The data obtained from reflectivity was fit using IGOR and the Motofit software packages using bi-layer models.[100] The software provides a scattering length density (SLD) profile from the model fit of the normalized reflection profile. The SLD profiles are plotted as a function of distance from the substrate interface where 0 is either the Si or PET interface.

It is essential to use both characterization methods because of their specific contrast sensitivities. Neutrons interact with the nucleus of the atom, and thus the neutron scattering length density of a material is dependent on both the density and the atomic composition of the material.[168] X-rays interact with the electrons in the sample, therefore x-ray scattering is more sensitive to density fluctuations in the material than small compositional changes.[168] Comparing the results from both characterization methods allows for a thorough analysis of the density and composition of each layer of the sample's depth

profile. The expected SLD values of each component is calculated with the National Institute of Standards and Technology (NIST) Center for Neutron Research (NCNR) calculator based on the provided densities and compositions of the deposited layers used in the following experiments are provided in Table 5.1.

Monitoring the SLD depth profiles of the same sample using both x-ray and neutron reflectivity provides qualitative assessment of layer thickness, composition, density, and interfacial breadth and roughness. The composition and the density of each layer can be calculated from the layer's SLD and the interfacial breadth and clarity is determined by inspecting the transition of the SLD profile between each layer. A steep transition indicates a sharp, well-defined interface while a gradual slope represents a broad interface.

The analyses of the samples are grouped by both substrate and ITO thickness. First the impact of the deposition of W onto a 25 nm ITO layers is investigated. Figure 5.2 shows the SLD profiles from neutron reflectivity (a) and x-ray reflectivity (b) of 25 nm ITO layers deposited on both Si and PET substrates. Each of these profiles exhibits multiple interfaces: substrate/ITO, and ITO/air or ITO/W and W/air. The 25 nm ITO layers deposited on Si substrates exhibit sharper interfaces at the ITO/substrate interface relative to the ITO layers on PET substrates, regardless of reflectivity source. Additionally, the ITO/W interface on PET substrates is broader than the same interface on Si substrates. The broad nature of the interfaces when deposited on PET substrates indicates regions consisting of a gradient from pure PET to pure ITO. Due to the broad interfaces present in the multilayer films deposited Close inspection of Figure 5.2 shows that both the x-ray and neutron SLDs of the 25 nm

Table 5.1 The scattering length densities for all the materials in this paper.

Material	Density (g/cm^3)	Composition	Calculated Neutron SLD (10^{-6} A^{-2})	Calculated X-Ray SLD (10^{-6} A^{-2})
W	19.3	W	3.00	122.0
ITO	7.11	$In_{18}O_{27}SnO_2$	4.03	53.55
PET	1.38	$C_{10}H_8O_4$	2.59	12.24
Si	2.32	Si	2.07	19.98
SiO_2	2.32	SiO_2	3.47	19.89

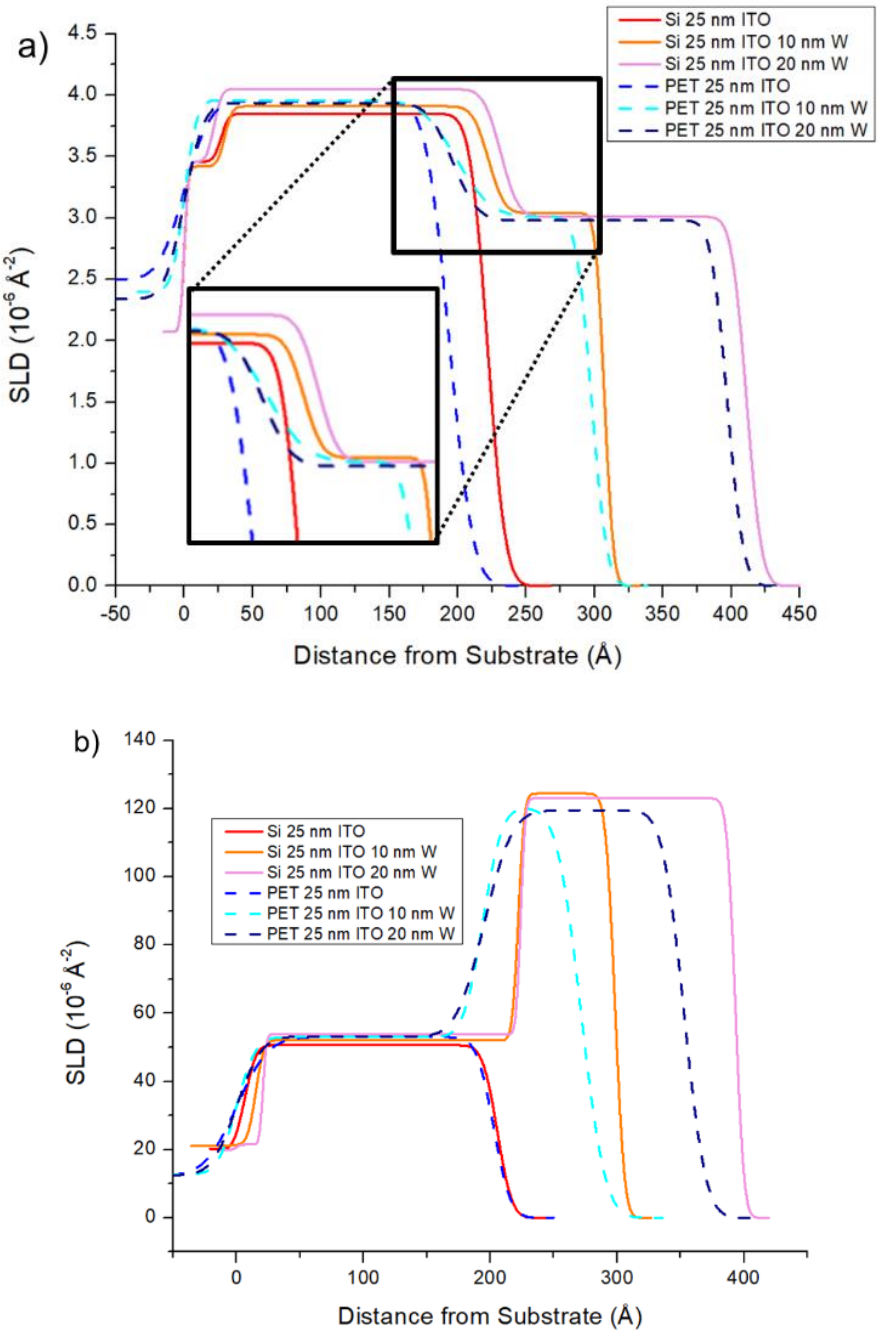


Figure 5.2 The neutron (a) and x-ray (b) SLD depth profiles for 25 nm ITO (Si/red, PET/dotted dark blue), 25 nm ITO plus 10 nm W (Si/orange, PET/dotted light blue), and 25 nm ITO plus 20 nm W (Si/pink, PET/dotted purple).

ITO layer increases as the W layer is deposited for the samples on Si substrates, while the SLD of the ITO layer on PET does not appear to change with W deposition. The neutron SLD of W is slightly larger for the Si substrate samples than on the PET substrate. on PET, the thickness of the pure region of the applied layers (ITO or W) may be reduced relative to the same layers on Si substrates. This increase in W SLD for the Si samples relative to the PET samples is much more apparent in the x-ray SLD depth profiles.

The experimental neutron and x-ray SLDs and thicknesses of the 25 nm ITO layer are provided in Table 5.2. The increase in the neutron SLD as the W is applied can be the result of an increase in oxygen in the film or an increase in density. To decouple the potential compositional or density change, Table 5.2 also provides theoretical x-ray SLD values based on the experimental neutron SLD. The NCNR SLD calculator tabulates x-ray and neutron SLDs based on the density and composition of a material. By independently altering the oxygen content and density of ITO, the calculated SLD changes. Both composition and density were altered independently until the calculated x-ray SLD matched the experimental neutron SLD. The x-ray SLDs of ITO with variation of density or compositional changes are also presented in Table 5.2. Comparison of the theoretical x-ray SLDs and the experimental x-ray SLD determines whether the change in neutron SLD is due to changes in the density or composition of the ITO layer. This analysis was conducted for the samples where the experimental neutron and x-ray SLDs differed from the expected SLD values. Finally, the last column in Table 5.2 provides the calculated change in density or composition for these samples.

Table 5.2 The experimental neutron and x-ray SLD values of the 25 nm ITO layers as well as the calculated x-ray SLD values based on an ITO composition or density change. Asterisks denote expected density or composition.

Sample	Neutron ITO Layer Thick-ness (Å)	Experi-mental Neutron ITO SLD (10^{-6} A^{-2})	X-ray ITO Layer Thick-ness (Å)	Experi-mental X-Ray ITO SLD (10^{-6} A^{-2})	Calcu-lated X-RAY ITO SLD Comp-osition Change (10^{-6} A^{-2})	Calcu-lated X-RAY ITO SLD Density Change (10^{-6} A^{-2})	ITO Density (g/cm^3) or ITO Composition
Si + 25 nm ITO	188	3.85	199	50.6	53.1	51.0	6.8
Si + 25 nm ITO + 10 nm W	194	3.90	207	52.1	53.1	52.0	6.95
Si + 25 nm ITO + 20 nm W	215	4.04	203	53.8	53.2	53.2	7.11*
PET +25 nm ITO	194	3.95	208	53.0	53.1	53.1	$In_{18}O_{27}SnO_2$*
PET +25 nm ITO + 10 nm W	199	3.96	194	53.1	53.2	53.2	$In_{18}O_{27}SnO_2$*
PET +25 nm ITO + 20 nm W	196	3.94	195	53.1	53.1	53.0	$In_{18}O_{27}SnO_2$*

Analysis of the Si substrate samples shows that experimentally, the neutron SLD of ITO increases as the 10 nm W layer is applied, and the neutron SLD of ITO continues to increase when the W layer is 20 nm. This increase in neutron ITO SLD corresponds to an increase in the experimental x-ray SLD for these samples as well. The theoretical x-ray SLD associated with an ITO density increase is close to the experimental x-ray SLDs of ITO in all the Si substrate samples with 25 nm ITO. For the thickest layer (20 nm) of W on 25 nm ITO and Si substrate, the experimental neutron and x-ray SLDs are the expected ITO SLD values. Thus, the deposition of the W layer on the underlying ITO layer results in an increase in the density of the ITO layer. The change in density of ITO as W is applied increases with W thickness, where the ITO density in the sample without a W layer is 6.8 g/ cm^3, the ITO density in the sample with a 10 nm W layer is 6.95 g/cm^3 and the ITO attains its expected density of 7.11 g/cm^3 with a coating of 20 nm W.

The ITO SLD on the PET substrate differed from the ITO SLD on Si substrates. The neutron and x-ray ITO SLDs on PET did not vary more than 0.5% throughout the application of the subsequent W layers. Moreover, both the x-ray and neutron ITO SLDs closely resemble the expected ITO SLD based on the expected density and the composition. The same experimental protocol and analysis was performed to determine the impact of depositing W onto 50 nm ITO layers. Figure 5.3 shows the SLD profiles from neutron reflectivity (a) and x-ray reflectivity (b) for 50 nm ITO layers deposited on Si and PET substrates. The ITO layers on Si substrates required a 2-layer model to best fit both the x-ray and neutron reflectivity profiles. The second layer is a thin layer (2-3 nm) at the

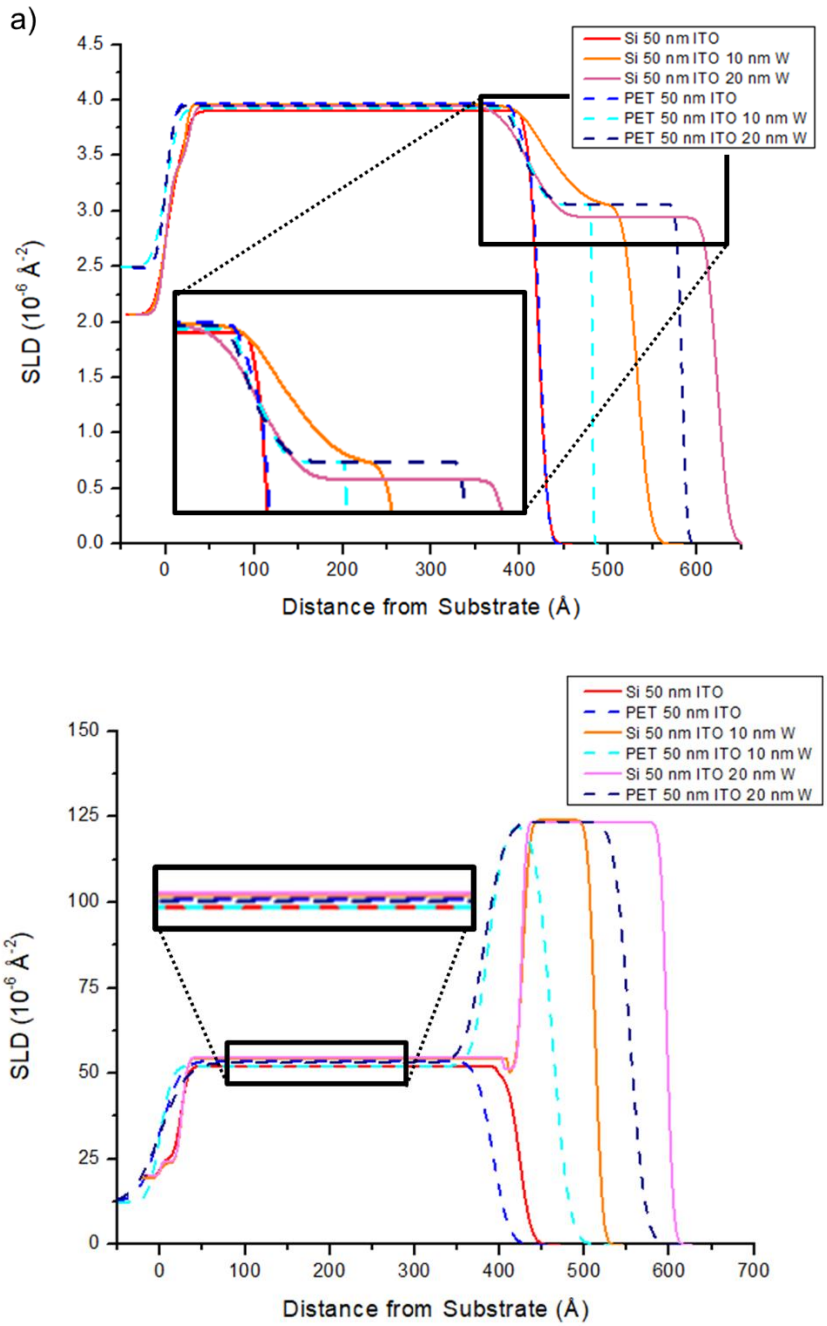


Figure 5.3 The neutron (a) and x-ray (b) SLD profiles for 50 nm ITO (Si/red, PET/dotted dark blue), 50 nm ITO plus 10 nm W (Si/orange, PET/dotted light blue), and 50 nm ITO plus 20 nm W (Si/pink, PET/ dotted purple).

air interface that has a slightly reduced SLD than the layer at the substrate interface. In the x-ray SLD profile, the thin layer manifests itself as a small dip in SLD while the neutron SLD profile presents the thin ITO layer near the air interface as a gradual slope and a broadened interface. Overall, the bulk ITO SLD does not appear to change for the samples on Si substrates with the deposition of W. The PET substrate samples with 50 nm ITO fit to a single ITO layer. Relative to the interfaces present in the Si substrate samples, even with the ITO layer on the Si substrates having a two-layer model, both the PET/ITO and ITO/W interfaces on PET substrates are broad. Neither the neutron or x-ray reflectivity SLD profiles of the 50 nm ITO layers on PET exhibit a change in the ITO SLD with the further deposition of the W layer on top.

Table 5.3 provides the thickness and SLD values of the 50 nm ITO layers for both neutron and x-ray reflectivity as a function of W layer thickness. The 50 nm ITO layers on Si substrates have two distinct layers with varying SLDs. These values are provided in Table 3 where, for each sample, the SLD listed first represents the SLD of the ITO layer closest to the air interface and the SLD listed second is the SLD of the ITO layer closest to the substrate. The theoretical x-ray SLDs are calculated in the same way as described previously for the 25 nm ITO samples. The SLD of the ITO layer near the substrate is only slightly different than the expected ITO SLD, while the SLD of the ITO top layer is consistent with a reduced density ITO. The variation in the pure 50 nm bulk ITO layer ITO (bottom) is consistent with a composition that has 1 less oxygen per unit ITO (3% oxygen depletion). This is only observed in the ITO sample on Si; the ITO layers closest to the

substrate in the two 50 nm ITO samples on Si exhibit the expected oxygen compositions. The thin air surface layer of ITO exhibits a reduction in density relative to both the expected ITO density and the ITO layer closest to the substrate. The ITO layer closest to the substrate contains the expected density of 7.11 g/cm^3 and the air surface layer ranges in density from 6.7-6.8 g/cm^3 dependent upon the thickness of W.

The model fits of the neutron reflectivity curves also show that the 50 nm ITO samples on PET substrates also contain two distinct ITO layers, where the air surface layer has the smaller SLD. However, when these samples are measured with x-ray reflectometry, only a single ITO layer is observed. To simultaneously analyze both experiments, the neutron SLD serves as a foundation for the calculation of theoretical x-ray SLDs with compositional or density changes of ITO. The experimental x-ray SLDs are compared to the theoretical x-ray SLDs to determine either compositional or density changes. Employing this analysis technique shows that the x-ray SLDs are consistent with an ITO compositional change. The compositions that correspond to the neutron SLDs for each layer are provided in the last column of Table 5.3. The orientation of SLDs in the table is the same as Table 5.2 where the first SLD listed represent the SLD of the ITO layer towards the air interface and the second SLD listed represents the SLD of the ITO layer closest to the substrate. ITO layers closest to the substrate retain the expected composition, but the ITO layers towards the air interface exhibit an oxygen deficiency up to 15%.

A similar analysis was completed to monitor the density or compositional changes of W for W films deposited onto ITO layers with different thicknesses. The experimental

Table 5.3 The experimental neutron and x-ray SLD values of the 50 nm ITO layers as well as the calculated x-ray SLD values based upon an ITO composition or density change. Asterisks denote expected density or composition.

Sample	Neutron ITO Layer(s) Thickness (Å)	Experimental Neutron ITO SLD (10^{-6} A^{-2})	X-ray ITO Layer(s) Thickness (Å)	Experimental X-Ray ITO SLD (10^{-6} A^{-2})	Calculated X-RAY ITO SLD Composition Change (10^{-6} A^{-2})	Calculated X-RAY ITO SLD Density Change (10^{-6} A^{-2})	Density (g/cm^3) or Composition
Si + 50 nm ITO	17.2	3.77	26.7	50.0	53.1	50.3	6.7
	382	3.90	373	52.0	53.1	52.0	7.0
Si + 50 nm ITO + 10 nm W	27.2	3.81	48.6	50.8	53.1	50.5	6.75
	390	3.96	353	53.5	53.2	53.2	$In_{18}O_{27}SnO_2$*
Si + 50 nm ITO + 20 nm W	30.9	3.73	12.6	51.5	52.9	49.4	6.8
	380	3.95	389	53.5	53.2	53.2	$In_{18}O_{27}SnO_2$*
PET + 50 nm ITO	23.2	3.47	392	53.6	52.9	46.4	$In_{18}O_{20}SnO_2$
	400	3.97			53.2	53.2	$In_{18}O_{27}SnO_2$*
PET + 50 nm ITO + 10 nm W	20.9	3.76	387	52.9	53.1	50.5	$In_{18}O_{24}SnO_2$
	395	3.92			53.2	52.0	$In_{18}O_{27}SnO_2$*
PET + 50 nm ITO + 20 nm W	22.7	3.54	382	53.1	52.9	46.4	$In_{18}O_{20}SnO_2$
	376	3.95			53.2	52.0	$In_{18}O_{27}SnO_2$*

and theoretical SLDs for W deposited on 25 nm ITO for both substrates are provided in Table 5.4. When W is deposited onto ITO that reside on Si substrates, the 20 nm W layer attains its expected density (19.3 g/cm^3) while the 10 nm W layer has a slightly larger density of 19.5 g/cm^3. When films of the same thickness of W are applied to the ITO that reside on PET substrates, the density never reaches the expected value of 19.3 g/cm^3. Regardless of the W layer thickness, the density is consistently 19.1 g/cm^3 and the experimental x-ray and neutron W SLDs are in good agreement of W density throughout.

The experimental and theoretical density SLD values of W deposited on 50 nm ITO for both substrates are provided in Table 5.5. When W is applied on to a 50 nm ITO that resides on Si substrates, the 10 nm W is slightly denser (19.5 g/cm^3) than the 20 nm W layer that is deposited on the same substrate (19.4 g/cm^3). Both of the W layer densities are slightly larger than the expected density of W (19.3 g/cm^3). When W is deposited on the 50 nm ITO layers that reside on PET substrates, the W layer maintains the same higher than expected density (19.6 g/cm^3) regardless of the W layer thickness.

Grazing Incidence X-ray Scattering

Grazing incidence x-ray scattering receives its name because the incident x-ray beam "grazes" the surface of the sample affording the ability to analyze structures at the surface. The penetration depth of the incident x-ray is dependent on the material composition, density, and x-ray incident angle. The penetration depth is only important when analyzing the in-plane structure, parallel to the substrate. Any scattering that is detected in-plane describes the surface structures within the penetration depth of the

Table 5.4 The experimental neutron and x-ray SLD values for W when deposited on a 25 nm ITO layer as well as the calculated x-ray SLD values based on a W density change. Asterisks denote expected density or composition.

Sample	Neutron W Layer Thickness (Å)	W layer Experi-mental Neutron SLD ($x10^{-6}$ A^{-2})	X-ray W Layer Thickness (Å)	W Layer Experi-mental X-Ray SLD ($x10^{-6}$ A^{-2})	Calcu-lated X-RAY SLD Density Change ($x10^{-6}$ A^{-2})	W Density (g/cm^3)
Si + 25 nm ITO	N/A	N/A	N/A	N/A	N/A	N/A
Si + 25 nm ITO + 10 nm W	105.0	3.04	76.2	124.4	124.2	19.5
Si + 25 nm ITO + 20 nm W	197.0	3.00	169.3	123.0	122.9	19.3*
PET +25 nm ITO	N/A	N/A	N/A	N/A	N/A	N/A
PET +25 nm ITO + 10 nm W	99.1	3.01	77.5	120.3	122.9	19.1
PET +25 nm ITO + 20 nm W	200.9	2.98	157.6	119.5	121.2	19.1

Table 5.5 The experimental neutron and x-ray SLD values for W when deposited on a 50 nm ITO layer as well as the calculated x-ray SLD values based upon a W density change. Asterisks denote expected density or composition.

Sample	Neutron W Layer(s) Thickness (Å)	Experi-mental Neutron SLD ($x10^{-6}$ A^{-2})	X-ray W Layer(s) Thickness (Å)	Experi-mental X-Ray SLD ($x10^{-6}$ A^{-2})	Calcu-lated X-RAY SLD Density Change ($x10^{-6}$ A^{-2})	W Density (g/cm^3)
Si + 50 nm ITO	N/A	N/A	N/A	N/A	N/A	N/A
Si + 50 nm ITO + 10 nm W	92.8	3.04	84.8	124.0	124.2	19.5
Si + 50 nm ITO + 20 nm W	185.6	3.00	170.8	123.5	122.9	19.4
PET + 50 nm ITO	N/A	N/A	N/A	N/A	N/A	N/A
PET + 50 nm ITO + 10 nm W	65.7	3.05	75.0	123.1	124.8	19.6
PET + 50 nm ITO + 20 nm W	188.2	3.06	170.8	123.5	124.8	19.6

incident x-ray. For the surface materials (ITO and W), the penetration depth has been calculated to be *ca*.1-3 nm. The penetration depth calculation is provided in the Appendix Figure 5.8.

To analyze the structures normal to the substrate, out-of-plane (α) line cuts were performed. The penetration depth is not relevant to the out-of-plane analysis as the out-of-plane analysis is performed similar to a reflectivity experiment, where the x-rays penetrate the entire thickness of the film. The line cut profiles show intensity of scattering as a function of the wave vector q. The intensity of the scattering is in arbitrary units, however the relative peak positions in q space provide information about the structures present normal to the substrate. The transformation from α to Q_z space is shown in Equation 5.3 where λ is the wavelength of the source.

$$Q_z = \frac{2\pi(\sin\left(\alpha*\left(\frac{\pi}{180}\right)\right)+\sin(\alpha_i))}{\lambda} \qquad \text{Equation (5.3)}$$

The line cuts for samples without W are provided in Figure 5.4. Qualitatively, the GISAXS curves of the ITO layers on Si substrates exhibit a single sharp peak and lack any additional structure throughout the q range, indicating no significant out-of-plane structure on these length scales. The ITO layers deposited onto the PET substrates both show a broad initial peak. The 25 nm ITO layer shows repetitive fringes throughout the q range while the 50 nm ITO layer lacks any structure at high q.

The Q_z line cuts for W layers deposited on 25 nm ITO and both substrates are provided in Figure 5.5. The 10 nm W layer deposited onto the 25 nm ITO that resides on Si exhibits multiple peaks throughout the q range: an initial sharp peak, a secondary sharp

peak in the middle of a broad fringe, and various broad fringes as the scan approaches higher q. The 10 nm W layer deposited onto 25 nm ITO that resides on PET exhibits a broad initial peak in addition to broad fringes at higher q with diverse spacing. The 20 nm W layers deposited on 25 nm ITO have similar Q_z scan profiles regardless of substrate. Both scans exhibit a sharp initial peak and a small broad peak covering similar q ranges.

Figure 5.6 shows the Q_z scan profiles of all W thicknesses on 25 nm ITO and 50 nm ITO layers for both substrates. The scans for both W thicknesses on Si substrates closely resemble one another where a sharp initial peak is observed proceeded closely by a broad peak. The differences in these two scans is observed around 1.5 nm^{-1} where the 10 nm W layer shows some broad structures and the 20 nm W layer does not show any structure formation at high q. The scans for W layers deposited on 50 nm ITO and PET substrates show similarity in the broad initial peaks, but the sample with a 10 nm W layer shows additional broad peak structure throughout the q range while the sample with a 20 nm W layer does not show any observable structure in the higher q range.

Repeats of the PET samples with 25 nm ITO were conducted to better understand the sharp peak in the 25 nm ITO plus 20 nm W sample. Figure 5.7 shows the PET Q_z scan profiles of all W thicknesses on 25 nm ITO and one set of repeats. The pure 25 nm ITO and the 25 nm ITO plus 10 nm W samples appear to be repeatable and show similar Q_z profiles. However, the original 25 nm ITO plus 20 nm ITO sample shows a sharp initial peak while the repeated sample shows a broad peak.

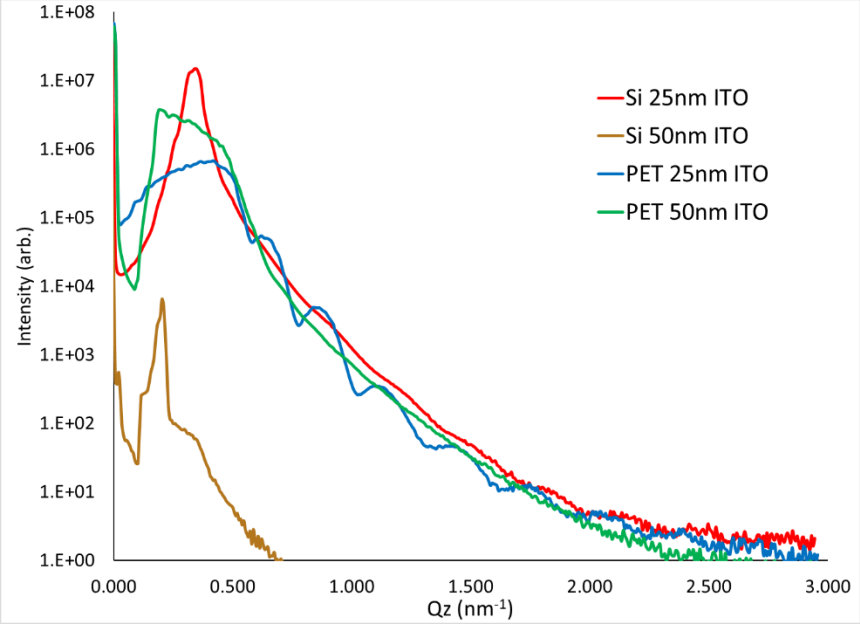


Figure 5.4 Qz line cuts of the GISAXS two-dimensional detector for Si + 25 nm ITO (red), Si + 50 nm ITO (gold), PET + 25 nm ITO (blue), PET + 50 nm ITO (green).

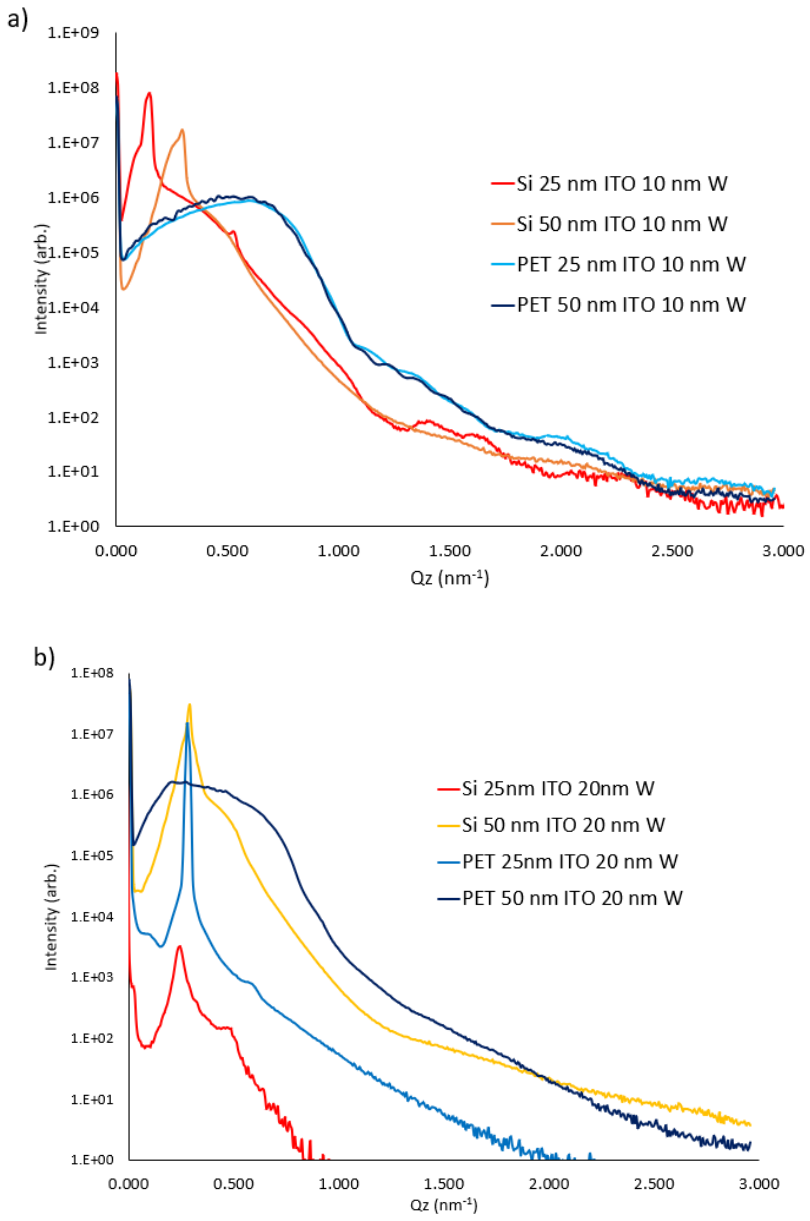


Figure 5.5 Qz line cuts of the two-dimensional detector images for 25 nm ITO + 10 nm W (Si/red, PET/light blue), 50 nm ITO +10 nm W (Si/orange, PET/purple) (a) and 25 nm ITO + 20 nm W (Si/red, PET/light blue), 50 nm ITO + 20 nm W (Si/orange, PET/purple) (b).

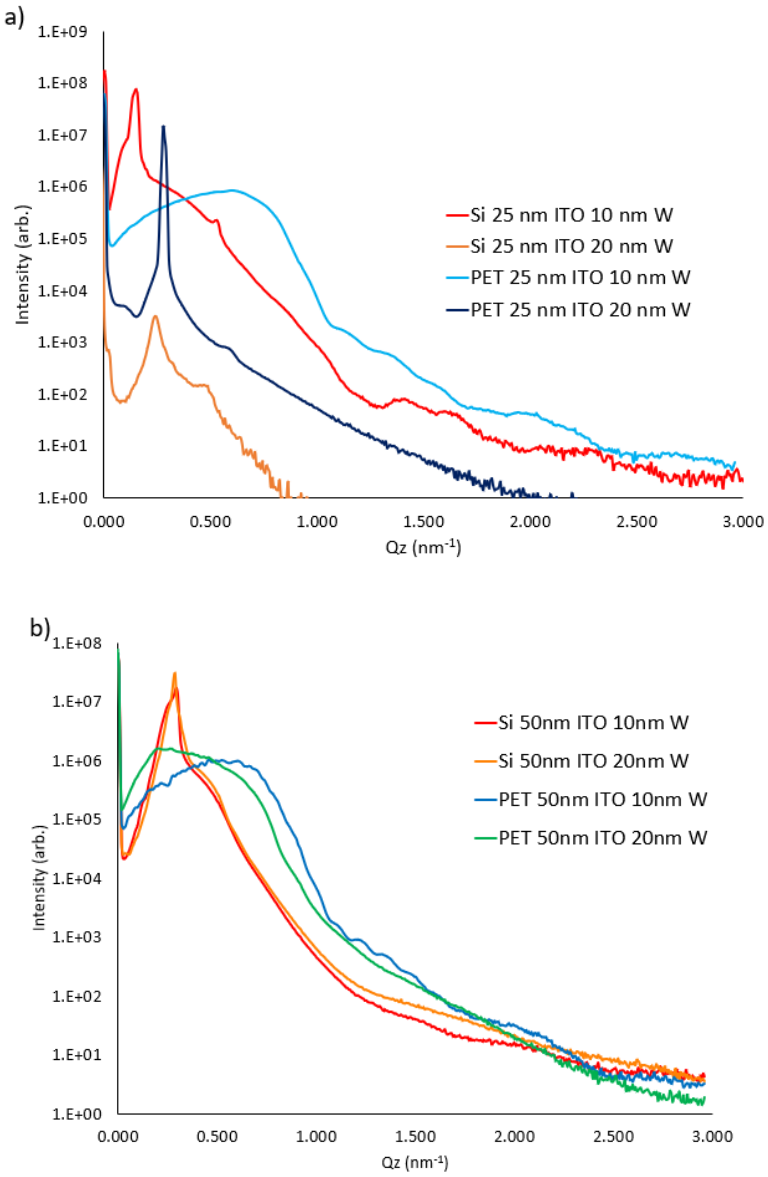


Figure 5.6 Qz line cuts of the two-dimensional detector images for 25 nm ITO + 10 nm W (Si/red, PET/light blue), 25 nm ITO + 20 nm W (Si/orange, PET/purple) (a) and 50 nm ITO + 10 nm W (Si/red, PET/blue), 50 nm ITO + 20 nm W (Si/gold, PET/green) (b).

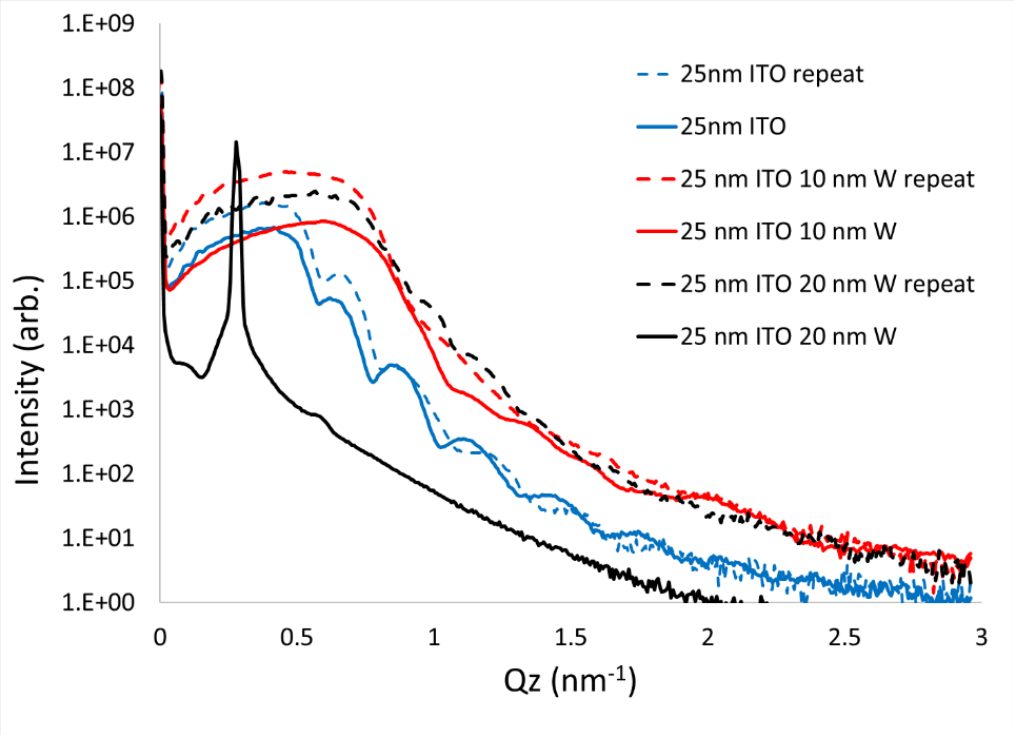


Figure 5.7 Qz line cuts of the two-dimensional detector images for PET + 25 nm ITO (blue), PET + 25 nm ITO + 10 nm W (red), PET + 25 nm ITO + 20 nm W (black) and their repeats (dashed lines).

Discussion

The data presented here documents the interfacial sharpness, layer composition, and density of sputtered bi-layer films of ITO and W onto Si and PET substrates. The parameter space investigated includes the substrate rigidity, the impact of sputtering W onto ITO on the density and composition of the ITO layer, and the importance of W or ITO layer thicknesses on these properties. The impact of these parameters on the structure of the fabricated films are important to the processing of sputtered thin films with targeted structure and properties as thin film technology expands from rigid, heavy substrates to flexible, light weight substrates. The ability to fabricate thin films onto flexible substrates expands the range of potential applications of the thin films. Additionally, understanding how the deposition of subsequent materials impact the integrity of previously deposited layers provides information on the limitations of the flexible substrates, layer thickness, or fabrication order. The results presented here show that the thin film properties, layer composition, density, and the interfacial sharpness all varied dependent on the precise processing conditions of each sample. It is clear the substrate plays a role in the ITO composition and density fluctuations that are present during the W layer deposition.

25 nm ITO Layers

Figure 5.2 shows the neutron and x-ray SLD profiles of 25 nm ITO samples that are deposited on Si substrates. As W was applied to the 25 nm ITO layer on silicon, the neutron and x-ray ITO SLDs increase. On the other hand, the neutron and x-ray SLDs of 25 nm ITO on the PET substrate do not change with the addition of the W layer.

Interpretation of this data indicates that the SLD increase of the 25 nm ITO layer on the Si substrates is due to an increase in ITO density as the 10 nm and 20 nm W layers are applied. This density increase is attributed to the ITO layer compacting under the sputtering power of W onto the surface.

The changes of ITO SLD, and more specifically the density, as a function of W layer application on Si substrates, but not PET substrates is attributed to the differences in hardness of the substrates. The indentation hardness, or the force over a specific area required to create a deformation, of silicon is approximately 10 GPa[169–171] while the indentation hardness of PET is reported in a range of 100 – 200 MPa.[172–176] Because silicon is orders of magnitude more robust than PET, it is much more difficult for the sputtered materials to deform the silicon substrate relative to the PET substrate. Thus, with silicon substrates, ITO becomes more compact (density increase) as the W is sputtered. On the other hand, when ITO is deposited onto PET and then a metal coating is applied, stress on the ITO layer can deform the PET layer, minimizing any impact on the density of the ITO layer. This conclusion is supported by the broad interfaces present in the samples that reside on the PET substrate. As well, the broader interfaces manifest because of the ability for ITO to deform and penetrate the substrate. Additionally, the interface between PET and ITO broadens as the W coating becomes thicker.

50 nm ITO Layers

When characterized with neutron reflectivity, the 50 nm ITO layers on PET and Si are best modeled with two distinct ITO layers with dissimilar SLDs. The ITO layer closer

to the substrate has a larger SLD than the ITO layer towards the air interface. The layer towards the air interface ranges in thickness but is no larger than 3 nm for either substrate.

50 nm ITO Layers on Silicon

When the 50 nm ITO layer on Si is characterized with x-ray reflectivity, a similar two-layer model is required where the ITO layer at the air interface is 2-3 nm and has a reduced ITO SLD than the bulk ITO layer at the silicon substrate. The SLD of the air interfacial ITO layer is smaller than the SLD of the ITO bulk when measured with both x-ray and neutron reflectivity. This indicates that the density of ITO in the air interfacial layer is less than the density of bulk ITO. The density of the air interfacial ITO layer is 6.7 g/cm^3 for the pure 50 nm ITO sample, increases to 6.75 g/cm^3 as 10 nm W is deposited, and is 6.8 g/cm^3 for the 50 nm ITO sample with 20 nm W. The air interfacial ITO layer becomes denser when the W layer is applied and the density increases with W thickness, but the density of this layer never reaches the density of the bulk ITO.

The density of the bulk ITO layer (closest to the silicon) also changes as the W layer is deposited. Before the W layer is deposited, the density of the supporting ITO layer is 7.0 g/cm^3, slightly reduced from the expected ITO density of 7.11 g/cm^3. With a 10 nm W layer, the density reaches the expected ITO density. The density increase of both the bulk and the air interfacial ITO layers is similar to the density increase observed for the 25 nm ITO layer samples as W was deposited. Again, the density increase of the supporting ITO layer is attributed to the indentation hardness of the substrate and the incapability for ITO to displace the silicon substrate inducing the compaction of ITO.

The formation of a less dense ITO layer at the air interface (for the 50 nm ITO samples) may be the result of voids present in the top layer. However, if voids were present at the air interface of the ITO layer, the sputtering of W could potentially fill the voids. The void filling would manifest in the reflectivity experiments as a broadening of the ITO:W interface and the thin ITO layer with a smaller SLD at the air interface would be undetectable after sputtering with W. The x-ray SLD depth profile (Figure 5.3b) shows that the thin ITO layer at the air interface is still detectable after sputtering with W. Hypothetically, this could mean a couple of different things: if the voids are present in the air surface-most ITO layer, that the voids are smaller than the sputtered W size, or that the reduction of ITO SLD at the air interface is not due to the presence of voids. It is important to note that the density of the ITO layer at the air interface increases as a function of sputtered W, but the thickness of the surface ITO layer does not change in the model fit. The increase in surface ITO layer density could represent the filling of voids leading to a reduction in the quantity of voids present, or a reduction of void size. Regardless of the mechanism leading to an ITO density increase, the thin ITO layer at the air interface does not disappear after a 20 nm W layer is sputtered onto the surface and further experiments are necessary to confirm they hypotheses.

50 nm ITO Layers on PET

When measured with neutron reflectivity, the samples with 50 nm ITO layers deposited on PET also are fit best with a two-layer ITO model, where the smaller ITO SLD is towards the air interface. However, when the 50 nm ITO layers are measured with x-ray

reflectivity, the profiles are best fit with a single-layer model. Neutron reflectivity is sensitive to both density and composition fluctuations, while x-ray reflectivity is most sensitive to density fluctuations. Since the x-ray reflectivity profiles only indicate a single ITO layer while the neutron reflectivity identifies two distinct layers, these layers (measured with neutron reflectivity) must contain different compositions of ITO. In fact, the composition of the smaller SLD layer at the air interface contains about 25 percent less oxygen than the expected ITO composition.

GISAXS Results

To gain more information on the double ITO layer formed in the samples with a 50 nm ITO layer, grazing incidence small angle scattering (GISAXS) was used. GISAXS simultaneously monitors the structure of the sample both in-plane and out of plane. To determine the in-plane structure of the films near the surface, an incidence angle less than the critical angle of the ITO and W coatings was selected. The penetration depth of the surface coatings, ITO and W, is 1-3 nm, thus the in-plane order obtained from the GISAXS experiments is at the air interface. The 2D GISAXS patterns for each sample are provided in the Appendix (Figures 5.9 and 5.10). None of the samples showed scattered intensities in the in-plane orientation (Q_y) indicating a homogenous distribution of material laterally. Additionally, none of the samples exhibited sharp scattering peaks on the detector, indicating no clear structuring or ordering on the surface of these films.

The characterization of the out-of-plane structure has some similarities to a reflectivity measurement however the angle of incidence is held constant throughout the

measurement. Because of the lack of correlation between the incident and scattered angles, the out-of-plane structure cannot be determined specifically by peak position, rather relative peak position provides information on layer thickness.[177,178] The out of plane structure is characterized by taking a Q_z line cut, where the distance between interfaces, or the thickness of each layer, is determined by the distance between the first peak maximum and other peak maximums present in the Q_z profile.

Many times, the first peak in a grazing-incidence profile is termed the Yoneda peak, and is described as the critical angle of the substrate.[179] The Yoneda peak is the most intense peak in the profile because at the substrate interface, the x-rays undergo total external reflection. The layer thickness measured with GISAXS follow the thicknesses of the layers measured with reflectivity and the values are provided in a table in the Appendix (Table 5.6). Although the Q_z line cut from GISAXS provides similar information as reflectivity, qualitative interpretations are very different. In reflectivity, a profile with many distinct fringes over the q range indicates well defined interfaces and the lack of fringes indicates broad interfaces. A GISAXS profile with many fringes or peaks indicates a presence of correlated roughness of a stratified sample.[180] The lack of fringes in any of the GISAXS profiles does not indicate roughness or lack of interfacial sharpness. Rather, it indicates a lack of correlated roughness between layers.

Another way to qualitatively examine the interfacial structure of the samples with GISAXS is to examine the breadth of the Yoneda peak. The breadth of the Yoneda peak correlates to the breadth of the substrate:layer 1 interface. A sharp Yoneda peak indicates

a sharp interface, while a broad peak indicates a broad interface. The presence of additional peaks throughout the Qz profile represents secondary layers and additional interfaces.

Single Layers of ITO

The Q_z scans of 50 and 25 nm ITO layers on both substrates are shown in Figure 5.4. The profiles for the films on silicon substrates show sharp Yoneda peaks relative to the scans of the samples on PET substrates. As expected, the interfaces between the substrate and ITO are much sharper for silicon substrates than the PET substrates. Also, regardless of substrate, the interfaces in the 50 nm ITO samples quantitatively sharpen relative to the 25 nm ITO layers on identical substrates, based on the sharpening of the Yoneda peak. The reduction of the Yoneda peak width indicates that the interface between the substrate and the ITO layer becomes increasingly distinct. It appears that the additional sputtering time required to fabricate an ITO film that is twice the thickness leads to a sharpening of the substrate:ITO interface.

Bi-Layers of ITO and 10 nm or 20 nm W

Figure 5.5a compares the GISAXS of the films samples that have 10 nm W layers on the initial ITO layer. The Q_z scans for these samples seem to be substrate specific where the samples with PET substrates resemble one another and the Si substrate Q_z scans resemble one another. However, the samples on PET substrates have broad Yoneda peaks, whereas the Si substrate samples have relatively sharp peaks. The 25 nm ITO sample on silicon contains multiple secondary peaks throughout high q that the 50 nm ITO sample on

silicon lacks. The appearance of secondary scattering peaks in the 25 nm sample indicates interfacial definition between the ITO and W layers. The lack of interfacial sharpness between the W and ITO layers in the 50 nm ITO sample with 10 nm W on silicon is consistent with the results obtained with neutron reflectivity where multiple density ITO layers were identified. The multiple ITO layers of varying densities measured with reflectivity manifests as the lack of secondary GISAXS peaks and is interpreted as a broad ITO:W interface.

Figure 5.5b shows the Q_z scans for the samples that have a 20 nm W layer as the top layer. Unlike the samples with 10 nm W, the thickness of the ITO layers appears to control the scattering curve, rather than the substrate. In these GISAXS Q_z scans, the scattering curves for the 25 nm ITO layers on Si and PET resemble one another, while the scattering curves for the 50 nm ITO layers with 20 nm W on Si and PET do not, however, the scattering curve for the Si substrate with 50 nm ITO and 20 nm W shows a much broader Yoneda peak than the scattering from the Si sample with 25 nm ITO and 20 nm W. The sharp PET peak is an interesting result because all of the Q_z scans for the PET substrates typically have broad Yoneda peaks and broad interfaces. The fact that the scattering curves for the 25 nm ITO 20 nm W sample has a sharp peak may indicate that the top W layer is thick enough that the PET substrate plays a reduced role in dictating the broad PET:ITO interface for this sample. Even with the inconsistencies of the sharpness of the substrate:ITO interface, the sputtering of 25 nm ITO and 20 nm W onto both Si and

PET all maintain the expected density and compositions of ITO and W calculated from the reflectivity SLD profiles.

Because of the inconsistencies of the appearance of the sharp ITO:PET interfaces, repeats were conducted of the PET samples with 25 nm ITO with all three W thicknesses to better understand the appearance of the sharp PET:ITO interface with 25 nm ITO and 20 nm W. The Q_z profiles for these samples are shown in Figure 5.7. The Q_z profiles for 25 nm ITO and 25 nm ITO and 10 nm W are similar across the entire q-range both maintaining broad peaks and broad interfaces. The original Q_z profile of the 25 nm ITO and 20 nm W and the repeat do not match at any point during the q range. The original profile shows a sharp interface while the repeat sample has broad interfaces, similar to all the other PET Q_z profiles. This result indicates that the sputtering processes of the ITO onto the PET are inconsistent and of limited repeatability. Further experiments are required to understand the impact of the sputtering process and the thickness of ITO and W on the PET:ITO interface.

The total thickness of the 25 nm ITO plus 20 nm W layers is ~45 nm. At this thickness, the PET:ITO interface is sharper than the other samples on PET substrates. It is interesting that the Q_z profiles of the samples with 50 nm ITO on PET do not also show increased order at the PET:ITO interface even though this 50 nm ITO sample has similar thickness to the sample with 25 nm ITO and 20 nm W layer coating. Applying the same thickness W layer (20 nm) onto a thicker ITO layer (50 nm) does not lead to a sharp PET:ITO interface. On the other hand, a thick ITO layer (50 nm) plus the same thickness

W layer (20 nm) on silicon exhibits a Yoneda peak that is broader than the all of the other silicon substrate samples, but not quite as broad as the PET substrate Yoneda peaks.

These results indicate that not only does a thicker supporting layer of ITO lead to the formation of second ITO layers at the air interface with different properties (composition and density) than the bulk, the thickness of the ITO layer modifies the influence of subsequent layer application. This generally leads to increased sharpness of the substrate:ITO interface when additional layers are deposited onto a thin ITO layer, but a broad substrate:ITO interface is retained for thick ITO layers. These conclusions are supported by the Q_z scans presented in Figure 5.6 where the peak breadths vary with the thickness of W onto 25 nm ITO layers regardless of substrate (6a), while the overall shape of the Q_z profile does not change with W thickness on 50 nm ITO layers regardless of substrate (6b).

Conclusion

Neutron and x-ray reflectivity experiments provide depth profiles of various ITO and W bi-layers on silicon and PET substrates. These results indicate that the inherent properties of the supporting substrate play a crucial role in the interfacial sharpness, composition, and density of ITO sputtered films. For the most part, the films deposited on silicon substrate exhibit sharp substrate:ITO interfaces while films deposited on PET formed broader substrate:ITO interfaces. The 25 nm ITO layers deposited onto silicon experienced a density increase as a function of the thickness of a W coating. These results

are attributed to the differences in substrate indentation hardness where the indentation hardness of silicon is orders of magnitude larger than PET.

The 50 nm ITO layers contained a thin layer of ITO at the air surface that consists of a slightly different ITO composition or density relative to the supporting ITO layer. To better understand this phenomenon, grazing incidence small angle x-ray scattering was conducted. The GISAXS results show that the samples, regardless of substrate, have homogenous amorphous in-plane lateral ordering and sample-specific out-of-plane ordering. In agreement with reflectivity results, the films deposited on PET substrates generally had broad interfaces relative to those formed on the silicon substrate. The 25 nm ITO and 20 nm W bilayer deposited on PET substrate did not show a broad interface, rather the interfacial sharpness of this sample resembled the interface of the 25 nm ITO 20 nm W sample on the silicon substrate.

The differences in composition, density, and interfacial quality are only observed with samples consisting of thick (50 nm) layers of ITO or bi-layers. With thicker coatings, the apparent influence of substrate on the coating properties is greatly reduced. These results therefore provide fundamental information that document the importance of supporting substrates and deposition order in the increasingly relevant field of multi-component coatings deposited onto flexible substrates.

Acknowledgements

The authors gratefully acknowledge the financial support from Eastman Chemical Company. We acknowledge the support of the National Institute of Standards and

Technology, U.S. Department of Commerce, in providing the neutron research facilities used in this work. We acknowledge the support of the NIST Center for Neutron Research for providing access to their x-ray diffractometer facility where a portion of the work was conducted. This work was performed in part at the Duke University Shared Materials Instrumentation Facility (SMIF), a member of the North Carolina Research Triangle Nanotechnology Network (RTNN), which is supported by the National Science Foundation (Grant ECCS-1542015) as part of the National Nanotechnology Coordinated Infrastructure (NNCI).

Appendix

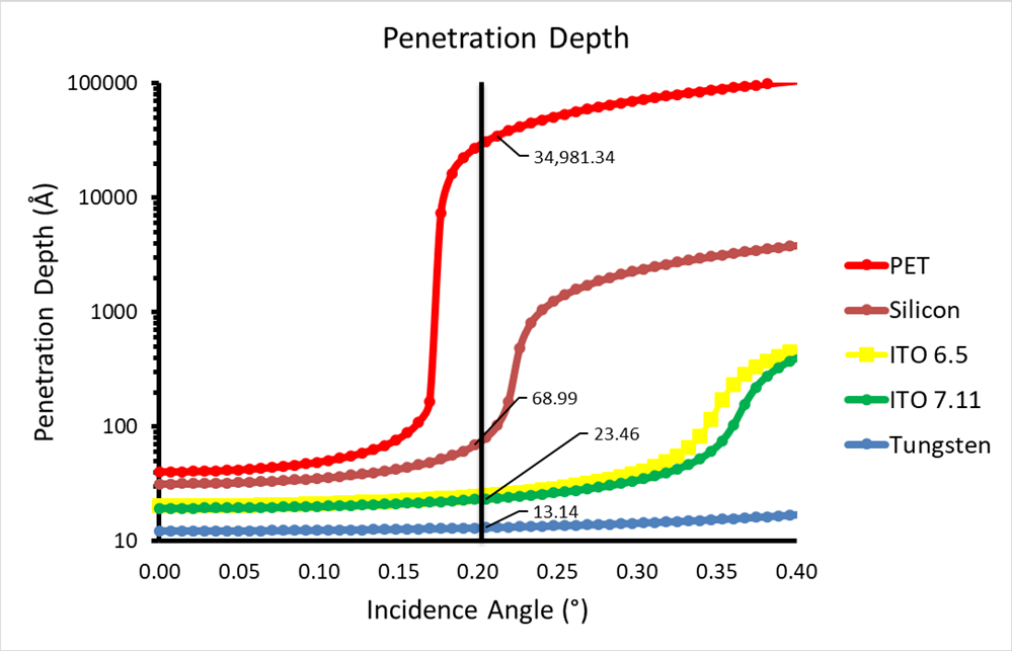


Figure 5.8 The penetration depth of the incident x-ray on each material. The number annotations denote the penetration depth (Å) with an incidence angle of 0.2°. The numbers for each ITO material are density values (g/cm3).

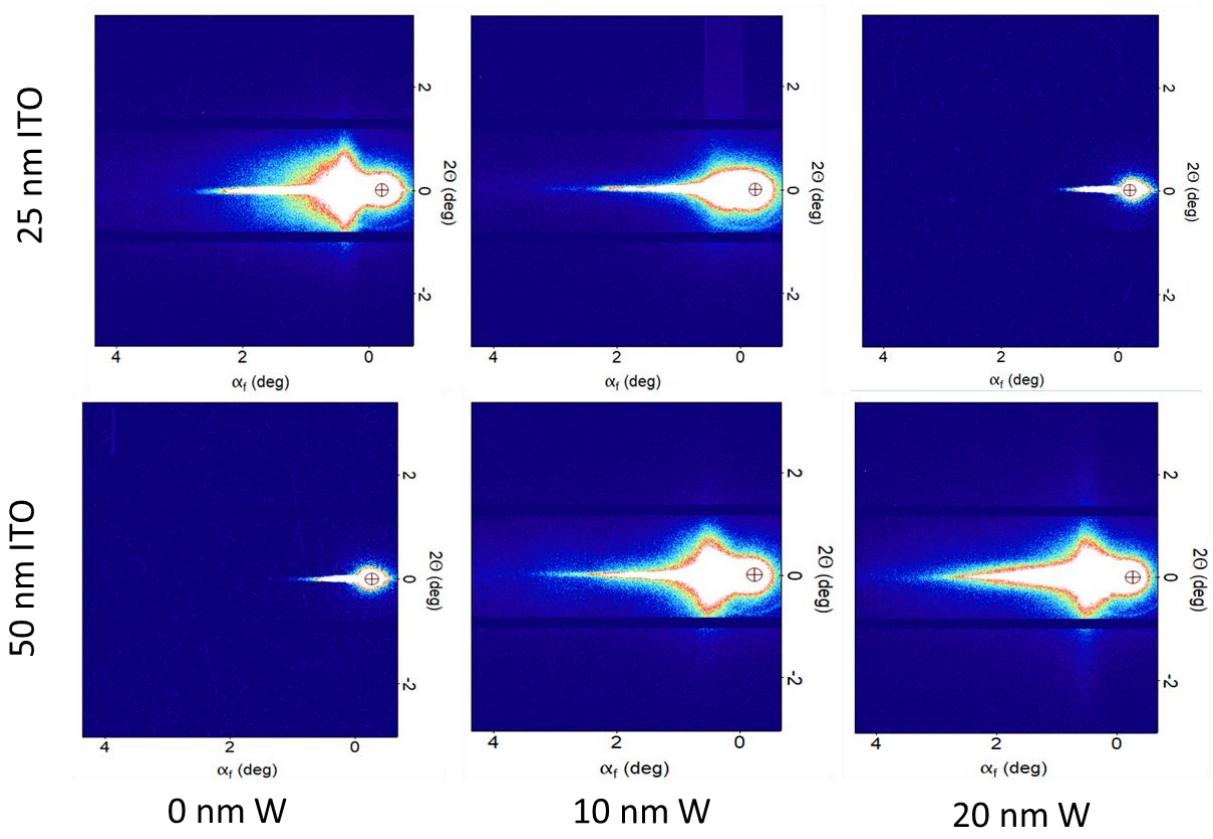


Figure 5.9 Two-dimensional detector images for the GISAXS measurements of ITO and W samples on silicon substrates.

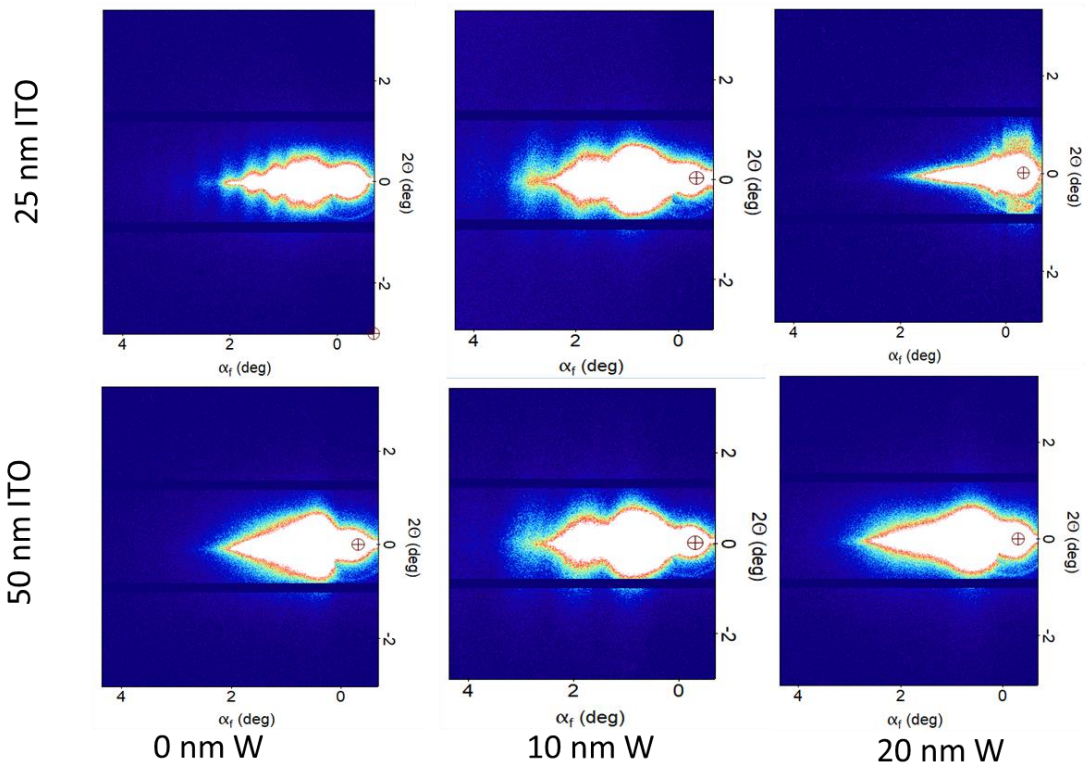


Figure 5.10 Two-dimensional detector images for the GISAXS measurements of ITO and W samples on PET substrates.

Table 5.6 The experimental layer thickness as measured with GISAXS for each sample.

Sample	Thickness of layer defined by spacing between peak 1 and peak 2 (nm)	Thickness of layer defined by spacing between peak 2 and peak 3 (nm)
PET + 25 nm ITO	23.0	24.3
PET + 25 nm ITO + 10 nm W	11.2	31.4
PET + 25 nm ITO + 20 nm W	18.1	-
PET + 50 nm ITO	-	-
PET + 50 nm ITO + 10 nm W	13.1	38.5
PET + 50 nm ITO + 20 nm W	-	-
Si + 25 nm ITO	-	-
Si + 25 nm ITO + 10 nm W	16.7	7.1
Si + 25 nm ITO + 20 nm W	23.6	-
Si + 50 nm ITO	40.5	-
Si + 50 nm ITO + 10 nm W	28.3	5.4
Si + 50 nm ITO + 20 nm W	28.3	4.3

CHAPTER SIX CONCLUSIONS AND FUTURE WORK

Conclusions

The overarching theme of this dissertation is to utilize neutron techniques to investigate the interfaces in multi-component and multi-layered polymeric materials for a wide range of applications. According to literature, certain thermodynamic properties are responsible for developing/maintaining the morphology of effective electronic devices and strong correlations between structure and device properties exist, but the extent that the processing conditions and polymer properties impact and control the final film structures and morphology is often overlooked. Thus, the focus of this dissertation work was to develop an understanding of these correlations to provide processing guidelines which produce specific thin film morphologies such as targeted interfacial widths and domain purities simply by altering the processing conditions.

A series of neutron reflectivity and scattering experiments were performed to study the structures present in final multi-component thin films fabricated by spin-casting and sputtering. Neutron reflectivity provides a compositional and density depth profile of thin films. Neutron scattering experiments paired with specific sample orientation in the beam and carefully chosen fitting models provide structural information perpendicular to the film surface to complement neutron reflectivity. The experiments outlined in this dissertation correlate specific chemical modifications and processing conditions to lateral and vertical structures in thin films. The results from the experiments indicate that substrate rigidity, blend composition, and polymer molecular weight play significant roles in the breadth of interfaces, layer composition, and layer thickness in multi-component self-stratified and sputtered thin films. Further, the structural properties paired with the thermodynamic of

the multi-component system and kinetic properties of the deposition process provide pathways to develop guidelines to tune both the lateral and vertical properties in thin films including domain purity, domain size, and interfacial breadth.

Kinetic and Thermodynamic Driving Forces in Polymer Blend Self-Stratification

The qualitative methods often used to analyze depth profiles of thin films inhibits direct assessment and comparison of two structurally different films. To improve the depth profile analysis and to assess the final films quantitatively, a novel method to systematically describe the final film morphology of a polymer blend thin film has been developed. According to this method, the degree of stratification is synonymous with the degree of vertical phase separation. This method allows for direct evaluation of the degree of phase separation produced as a result of the specific processing conditions utilized to fabricate the thin films.

Light reflectivity experiments show that slow casting speeds provide slow solvent evaporation and long film formation times relative to fast casting speeds and fast solvent evaporation. Increasing the film formation time, and more broadly, the kinetics of film fabrication alters the stratification because the polymers are allowed more time to rearrange in solution to approach an equilibrium. Generally, more stratified thin films emerge when slower casting speeds are utilized compared to faster casting speeds. However, the thermodynamic forces responsible for stratification are different for each casting speed. The results indicate a phenomenon where there appears to be a coupling of the thermodynamic and kinetic factors that influence film morphology.

At fast casting speeds, stratification occurs and P3HT is driven towards the air interface except when the molecular weight of both polymers is equivalent. In this case, a more homogenous thin film is obtained. At high spin rates and thus films that are formed very quickly, the degree of stratification is a function of P3HT:dPMMA blend composition indicating stratification is mostly driven by the immiscible polymer-polymer interactions and relative surface energies of the two polymers. Not only does the stratification increase but a sharpened interface between P3HT-rich and dPMMA-rich domains is obtained when the concentration of P3HT in the blend is increased. At the fastest casting speeds, the lack of stratification of equivalent molecular weights indicates entropy is a dominant driving force for stratification because stratification does not occur unless there is a difference in molecular weight. However, the degree of stratification does not change for specific blend compositions with varying dPMMA molecular weights. This result indicates that an entropic difference in molecular weight of the two polymers is strongly coupled to surface energy and polymer-polymer interactions to drive the stratification pattern.

As the casting speed decreases from the highest casting speed, the impact of the entropic driving force on the degree of stratification is clearer. At the intermediate casting speed, each sample exhibits stratification where P3HT is driven towards the air interface and increasing the dPMMA molecular weight and increasing the P3HT concentration encourages more stratification in a sample. The samples containing equivalent P3HT and dPMMA molecular weights exhibit stratification that differ from those prepared at the fastest casting speed.

An increase in extent of stratification as a function of decreasing casting speed is obtained for all the P3HT:131,500 g/mol dPMMA blend compositions, but this cannot be

said for any of the blends containing other dPMMA molecular weights. The trends for samples prepared at the slowest casting speeds are unclear and indicate that multiple driving forces are simultaneously dictating and controlling the final film structure. Moreover, at the longest film formation times, the entropy, relative surface energies, polymer-polymer interactions, and relative solubility limits of the two polymers in the pre-deposition solvent all play a role in the final film structure. In fact, at the slowest casting speed, P3HT rich regions are found not only at the air interface, but at the substrate interface as well. This is attributed to P3HT prematurely reaching its solubility limit prior to the final film drying.

These results ultimately provide guidelines to control and moderate the final film morphology and layering of deposited polymer blend thin films. Although these results isolate the relative importance of individual thermodynamic parameters, the results also provide insight into the kinetic factors that couple to the important thermodynamic properties (entropy, enthalpy, solubility, miscibility) and impact the stratification of a polymer blend. By intelligently altering the kinetics and balancing the thermodynamic properties controlled by the polymer blend composition and polymer molecular weight, the extent of stratification and depth profiles is tailored.

Lateral vs Vertical Phase Separation in Processing of Immiscible Polymer Blends

The information from neutron reflectivity experiments is complemented by small-angle neutron scattering (SANS) experiments which monitors the lateral phase separation in the same samples investigated with neutron reflectivity. A complete picture of phase separation has been developed by combining the results from these two orthogonal

characterization methods to probe the effects of spin casting speed and blend composition on lateral and vertical phase separation of P3HT:dPMMA blends.

The data suggests that an increase in the P3HT concentration leads to sharp horizontal interfaces and increased lateral phase sizes and contrast. Increasing the film formation time by decreasing the spinning speed leads to an increase in the size and concentration of the P3HT rich horizontal layer, and an increase in the size of the lateral phases while reducing the lateral phase contrast. This three-dimensional structural analysis holds promise to benefit device production as a method to better correlate nano and mesoscale structural changes to changes in electronic performance due to changes in processing where a single structure analysis may fall short.

Impact of Substrate Rigidity on the Composition and Density of Functional Multilayer Films

Metallic thin films comprised of varying thicknesses of ITO and W layers were sputtered onto flexible PET and rigid silicon substrates. Analysis of the films with neutron and x-ray reflectivity provides composition and density depth profiles of each sample. The films deposited on silicon substrates exhibit sharp substrate:ITO interfaces while films deposited on PET formed broader substrate:ITO interfaces. Striking differences among substrate specific composition and density depth profiles arise as the ITO thickness is increased. Thin ITO layers sputtered onto silicon substrates reveal increased density as W layers are sputtered as top coatings. Additionally, thicker ITO layers on both substrates leads to nanometer thick layers of varying composition (PET) and density (silicon) near

the air interface. Grazing incidence x-ray scattering is coupled with reflectivity measurements to better define surface and sub-surface structures in- and out-of-plane relative to the substrate. GISAXS results support the reflectivity results and reveal homogenous amorphous in-plane lateral ordering and substrate-specific out-of-plane ordering and interfacial breadth where the PET substrates have broader interfaces than silicon substrates. Consideration of the relative indentation hardness of both substrates provides an understanding of the varied ITO properties for each specific layer thickness. Ultimately, the data indicates that substrate rigidity influences interfacial breadth and increasing the thickness of the coating leads to a reduction of the apparent influence of substrate on the coating properties.

Summary

The net result from these experiments shows the importance of tracking and controlling processing conditions of spin casted and sputtered thin films. A subtle change in polymer blend composition, polymer molecular weight, casting speed, sputtering time, or substrate rigidity elicits changes in the final film structures such as domain purity, domain size, and interfacial breadth properties known to impact thin film performance and stability. Understanding the driving forces for stratification allows for direct modification of the processing conditions to obtain targeted lateral and vertical thin film morphologies. Furthermore, these guidelines are primarily foundational, however, paired with the methodology used throughout this research, one-step processing protocols of a multitude of polymer blends may be developed.

Future Work

This research ultimately outlines a methodology to determine the correlation between processing conditions and thin film structure in multi-component polymer thin films. Since P3HT and PMMA are widely used for organic field effect transistors and ITO is employed as a transparent conductive material, the results of these experiments expand the ability to controllably tailor the final film structure for efficient electronic devices simply by altering the processing conditions. The conclusions from these experiments formulate thermodynamic and kinetic guidelines for thin film fabrication that may be applied to other polymer blend systems where the desired application-specific structures are known. However, the previous experiments solely focus on the stratification of a polymer blend where the lowest molecular weight polymer also has the smallest surface energy. Polymer blends that do not maintain these properties may follow different guidelines. Thus, further experiments are required to elaborate on the foundational understanding developed in these experiments.

Stratification of Polymer Blends

A broader survey of blend composition and polymer molecular weight will allow a more thorough investigation of the thermodynamic hierarchy driving stratification. Blend compositions comprised of equal parts P3HT:dPMMA or P3HT rich blends will provide further information on the role of the physical polymer-polymer interaction in phase separation and completes the composition phase diagram for phase separation. Surveying a range of P3HT molecular weights including smaller and larger than the dPMMA molecular weight would decouple the entropic and surface energy driving forces allowing

for the identification of the dominant driving force for stratification. An ambitious method to decouple entropic and enthalpic driving forces for stratification is to synthesize a myriad of P3HT architectures with the focus on altering the degree of branching. This experiment specifically changes the entropy of the system without changing the molecular weight.

Investigating the effect of solvent quality not only introduces different solvent-polymer interactions that may influence film stratification, it will most likely change film formation time as well. This experiment can be conducted by changing the casting solvent and by introducing solvent-annealing chamber to the spin casting fabrication method. These experiments may make deciphering the dominant driving force more difficult because of the simultaneous changes in thermodynamic driving forces and kinetic drying, yet each experiment introduces additional processing conditions to further tailor the final film structures. Neutron reflectivity experiments monitoring the impact of casting solvent on depth profile paired with small angle neutron scattering experiments of dilute solutions will ultimately describe the influence the of the solvated polymer morphology on the final film structure. Introducing solvent annealing during fabrication influences the surface energy environment by selectively controlling the surface energy at the air interface of the film. The surface energy can also be changed by silane treatment of the silicon wafers prior to film fabrication. The silane pretreatment could be designed to mimic the surface energy of a flexible substrate such as PET. This experiment would decouple the influence of surface energy from substrate flexibility when utilizing flexible substrates for self-stratification.

Although post-modification procedures are undesirable for scaling up self-stratification to an industrial scale, thermal and solvent annealing may aid in understanding

the required conditions for desired film morphologies. In-situ neutron reflectivity is made possible by introducing an on-line solvent and/or thermal annealing chamber. This chamber allows for direct assessment of the depth profile and the dynamics of phase separation as it approaches and reaches a solvated state, information only extrapolated from the structures obtained by changing the casting speed.

Sputtering onto Flexible Substrates

A great deal of potential exists to further investigate the effects of replacing traditional rigid substrates with flexible counterparts. Elaborate neutron and x-ray reflectivity studies investigating the impact of sputtering processing conditions such as the pressure, sputtering power, and gas flow and their impact on depth profiles, and more specifically, the ITO film thickness, density, and composition on PET substrates in comparison to the same studies on silicon substrates can provide the fundamental information necessary to develop conclusive evidence of the implications of utilizing flexible substrates. Comprehensive grazing incidence x-ray scattering experiments including several angles of incidence can provide structural information focusing on the lateral ordering at specific depths throughout the thickness of the films.

Rather than only investigating two ends of the substrate flexibility spectrum, surveying other substrates can give further insight on the influence of the substrate in sputtered thin films. The list of possible film components, quantity of components/layers, and layer thicknesses is endless. Yet a broad study of these parameters paired with the compositional and density depth profiles and device relevant properties such as

conductivity, transparency, and mechanical strength will provide preliminary information regarding processing parameters and structures necessary for effective device performance.

.

LIST OF REFERENCES

(1) Voevodin, A. A.; Walck, S. D.; Zabinski, J. S. Architecture of Multilayer Nanocomposite Coatings with Super-Hard Diamond-like Carbon Layers for Wear Protection at High Contact Loads. *Wear* **1997**, *203–204*, 516–527. https://doi.org/10.1177/1097184X13516961.
(2) Mülhaupt, R. Hermann Staudinger and the Origin of Macromolecular Chemistry. *Angew. Chemie - Int. Ed.* **2004**, *43* (9), 1054–1063. https://doi.org/10.1002/anie.200330070.
(3) Roedel, M. J. The Molecular Structure of Polyethylene. I. Chain Branching in Polyethylene during Polymerization. *J. Am. Chem. Soc.* **1953**, *75* (24), 6110–6112. https://doi.org/10.1021/ja01120a005.
(4) Willbourn, A. H. Polymethylene and the Structure of Polyethylene: Study of Short-Chain Branching, Its Nature and Effects. *J. Polym. Sci.* **1959**, *34* (127), 569–597. https://doi.org/10.1002/pol.1959.1203412740.
(5) Passador, F. R.; Ruvolo-Filho, A.; Pessan, L. A. Nanocomposites of Polymer Matrices and Lamellar Clays. *Nanostructures* **2017**, 187–207. https://doi.org/10.1016/B978-0-323-49782-4.00007-3.
(6) Kuzumaki, B. T.; Ujiie, O.; Ichinose, H. Mechanical Characteristics and Preparation of Carbon Nanotube Fiber-Reinforced Ti Composite. **2000**, *8575* (7), 416–418.
(7) Rosa, I. M. De; Sarasini, F.; Sarto, M. S.; Member, S. EMC Impact of Advanced Carbon Fiber / Carbon Nanotube Reinforced Composites for Next-Generation Aerospace Applications. **2008**, *50* (3), 556–563.
(8) Li, Y.-C.; Mannen, S.; Morgan, A. B.; Chang, S.; Yang, Y.-H.; Condon, B.; Grunlan, J. C. Intumescent All-Polymer Multilayer Nanocoating Capable of Extinguishing Flame on Fabric. *Adv. Mater.* **2011**, *23* (34), 3926–3931. https://doi.org/10.1002/adma.201101871.
(9) Ghidoni, D.; Bencini, E.; Nocci, R. Compatibilizing PPE and PA6 with Nitro-Phthalimide Derivatives. *J. Mater. Sci.* **1996**, *31* (1), 95–101. https://doi.org/10.1007/BF00355132.
(10) Ma, N.; Li, Y.; Xu, H.; Wang, Z.; Zhang, X. Dual Redox Responsive Assemblies Formed from Diselenide Block Copolymers. *J. Am. Chem. Soc.* **2010**, *132* (2), 442–443. https://doi.org/10.1021/ja908124g.
(11) Morimoto, N.; Watanabe, A.; Iwasaki, Y.; Akiyoshi, K.; Ishihara, K. Nano-Scale Surface Modification of a Segmented Polyurethane with a Phospholipid Polymer. *Biomaterials* **2004**, *25* (23), 5353–5361. https://doi.org/10.1016/j.biomaterials.2003.12.047.
(12) Peinemann, K. V.; Abetz, V.; Simon, P. F. W. Asymmetric Superstructure Formed in a Block Copolymer via Phase Separation. *Nat. Mater.* **2007**, *6* (12), 992–996. https://doi.org/10.1038/nmat2038.
(13) Lee, J. H.; Kopecek, J.; Andradet, J. D. Protein-Resistant Surfaces Prepared by PEO-Containing Block Copolymer Surfactants. **1989**, *23*, 351–368.
(14) Norton, K. A.; Popel, A. S.; Pandey, N. B. Heterogeneity of Chemokine Cell-Surface Receptor Expression in Triple-Negative Breast Cancer. *Am. J. Cancer Res.*

2015, *5* (4), 1295–1307. https://doi.org/10.1002/app.
(15) Jellinek, H. H. G.; Kachi, H.; Kittaka, S.; Lee, M.; Yokota, R. Ice Releasing Block-Copolymer Coatings. *Colloid Polym. Sci. Kolloid-Zeitschrift Zeitschrift für Polym.* **1978**, *256* (6), 544–551. https://doi.org/10.1007/BF01639199.
(16) Huang, E.; Rockford, L.; Russell, T. P.; Hawker, C. J. Nanodomain Control in Copolymer Thin Films. *Nature* **1998**, *395* (6704), 757–758. https://doi.org/10.1038/27358.
(17) Drzal, P. L.; Shull, K. R. Origins of Mechanical Strength and Elasticity in Thermally Reversible, Acrylic Triblock Copolymer Gels. *Macromolecules* **2003**, *36* (6), 2000–2008. https://doi.org/10.1021/ma021255v.
(18) Ye, G.; Lee, J.; Perreault, F.; Elimelech, M. Controlled Architecture of Dual-Functional Block Copolymer Brushes on Thin-Film Composite Membranes for Integrated "Defending" and "Attacking" Strategies against Biofouling. *ACS Appl. Mater. Interfaces* **2015**, *7* (41), 23069–23079. https://doi.org/10.1021/acsami.5b06647.
(19) Shibayama, M.; Mizutani, S.; Nomura, S. Thermal Properties of Copolymer Gels Containing *N* -Isopropylacrylamide. *Macromolecules* **1996**, *29* (6), 2019–2024. https://doi.org/10.1021/ma951390q.
(20) Chen, S.; Li, L.; Zhao, C.; Zheng, J. Surface Hydration: Principles and Applications toward Low-Fouling/Nonfouling Biomaterials. *Polymer (Guildf).* **2010**, *51* (23), 5283–5293. https://doi.org/10.1016/j.polymer.2010.08.022.
(21) Kang, G.; Yu, H.; Liu, Z.; Cao, Y. Surface Modification of a Commercial Thin Film Composite Polyamide Reverse Osmosis Membrane by Carbodiimide-Induced Grafting with Poly(Ethylene Glycol) Derivatives. *Desalination* **2011**, *275* (1–3), 252–259. https://doi.org/10.1016/j.desal.2011.03.007.
(22) Louie, J. S.; Pinnau, I.; Ciobanu, I.; Ishida, K. P.; Ng, A.; Reinhard, M. Effects of Polyether-Polyamide Block Copolymer Coating on Performance and Fouling of Reverse Osmosis Membranes. *J. Memb. Sci.* **2006**, *280* (1–2), 762–770. https://doi.org/10.1016/j.memsci.2006.02.041.
(23) Delauney, L.; Compère, C.; Lehaitre, M. Biofouling Protection for Marine Environmental Sensors. *Ocean Sci* **2010**, *6*, 503–511. https://doi.org/10.5194/os-6-503-2010.
(24) Rice, K. C.; Bayles, K. W. Molecular Control of Bacterial Death and Lysis. *Microbiol. Mol. Biol. Rev.* **2008**, *72* (1), 85–109. https://doi.org/10.1128/MMBR.00030-07.
(25) Lewis, K. Programmed Death in Bacteria. *Microbiol. Mol. Biol. Rev.* **2000**, *64* (3), 503–514. https://doi.org/10.1128/MMBR.64.3.503-514.2000.
(26) Ba, C.; Economy, J. Preparation and Characterization of a Neutrally Charged Antifouling Nanofiltration Membrane by Coating a Layer of Sulfonated Poly(Ether Ether Ketone) on a Positively Charged Nanofiltration Membrane. *J. Memb. Sci.* **2010**, *362* (1–2), 192–201. https://doi.org/10.1016/j.memsci.2010.06.032.
(27) Kang, G.; Cao, Y. Development of Antifouling Reverse Osmosis Membranes for

Water Treatment: A Review. *Water Res.* **2012**, *46* (3), 584–600. https://doi.org/10.1016/j.watres.2011.11.041.
(28) Matyjaszewski, K.; Xia, J. Atom Transfer Radical Polymerization. *Chem. Rev.* **2001**, *101* (9), 2921–2990. https://doi.org/10.1021/cr940534g.
(29) Zoppe, J. O.; Ataman, C.; Mocny, P.; Wang, J.; Moraes, J.; Klok, A. Surface-Initiated Controlled Radical Polymerization: State-of-the-Art, Opportunities, and Challenges in Surface and Interface Engineering with Polymer Brushes. **2017**. https://doi.org/10.1021/acs.chemrev.6b00314.
(30) Krishnamoorthy, M.; Hakobyan, S.; Ramstedt, M.; Gautrot, J. E. Surface-Initiated Polymer Brushes in the Biomedical Field: Applications in Membrane Science, Biosensing, Cell Culture, Regenerative Medicine and Antibacterial Coatings. *Chem. Rev.* **2014**, *114* (21), 10976–11026. https://doi.org/10.1021/cr500252u.
(31) Krausch, G. Surface Induced Self Assembly in Thin Polymer Films. *Mater. Sci. Eng. R Reports* **1995**, *14* (1–2), v–vi. https://doi.org/10.1016/0927-796X(94)00173-1.
(32) Reich, S.; Cohen, Y. Phase Separation of Polymer Blends in Thin Films. *J. Polym. Sci. Polym. Phys. Ed.* **1981**, *19* (8), 1255–1267. https://doi.org/10.1002/pol.1981.180190809.
(33) Barlow, J. W.; Paul, D. R. *Molecular Weight Effects on Phase Behavior of Blends of Poly(Phenylene Oxide) with Styrenic Triblock Copolymers*; 1988; Vol. 21.
(34) Kim, J.; Mok, M. M.; Sandoval, R. W.; Woo, D. J.; Torkelson, J. M. Uniquely Broad Glass Transition Temperatures of Gradient Copolymers Relative to Random and Block Copolymers Containing Repulsive Comonomers. *Macromolecules* **2006**, *39* (18), 6152–6160. https://doi.org/10.1021/ma061241f.
(35) Matyjaszewski, K.; Ziegler, M. J.; Arehart, S. V.; Greszta, D.; Pakula, T. Gradient Copolymers by Atom Transfer Radical Copolymerization. *J. Phys. Org. Chem.* **2000**, *13* (12), 775–786. https://doi.org/10.1002/1099-1395(200012)13:12<775::AID-POC314>3.0.CO;2-D.
(36) Gray, M. K.; Zhou, H.; Nguyen, S. B. T.; Torkelson, J. M. Synthesis and Glass Transition Behavior of High Molecular Weight Styrene/4-Acetoxystyene and Styrene/4-Hydroxystyrene Gradient Copolymers Made via Nitroxide-Mediated Controlled Radical Polymerization. *Macromolecules* **2004**, *37* (15), 5586–5595. https://doi.org/10.1021/ma0496652.
(37) Buzin, A. I.; Pyda, M.; Costanzo, P.; Matyjaszewski, K.; Wunderlich, B. Calorimetric Study of Block-Copolymers of Poly (n -Butyl Acrylate) and Gradient Poly (n -Butyl Acrylate- Co -Methyl Methacrylate).
(38) Beaugendre, A.; Degoutin, S.; Bellayer, S.; Pierlot, C.; Duquesne, S.; Casetta, M.; Jimenez, M. Progress in Organic Coatings Self-Stratifying Coatings : A Review. *Prog. Org. Coatings* **2017**, *110*, 210–241. https://doi.org/10.1016/j.porgcoat.2017.03.011.
(39) Lee, H.; Lee, Y.; Statz, A. R.; Rho, J.; Messersmith, P. B. *Substrate-Independent Layer-by-Layer Assembly by Using Mussel-Adhesive-Inspired Polymers* **; 2008.
(40) Nie, X.; Leyland, A.; Song, H. W.; Yerokhin, A. L.; Dowey, S. J.; Matthews, A.

Thickness Effects on the Mechanical Properties of Micro-Arc Discharge Oxide Coatings on Aluminium Alloys. *Surf. Coatings Technol.* **1999**, *116–119*, 1055–1060. https://doi.org/10.1016/S0257-8972(99)00089-4.

(41) Leterrier, Y.; Médico, L.; Demarco, F.; Månson, J. A. E.; Betz, U.; Escolà, M. F.; Olsson, M. K.; Atamny, F. Mechanical Integrity of Transparent Conductive Oxide Films for Flexible Polymer-Based Displays. *Thin Solid Films* **2004**, *460* (1–2), 156–166. https://doi.org/10.1016/j.tsf.2004.01.052.

(42) Dominko, R.; Bele, M.; Gaberscek, M.; Remskar, M.; Hanzel, D.; Pejovnik, S.; Jamnik, J. Impact of the Carbon Coating Thickness on the Electrochemical Performance of LiFePO[Sub 4]/C Composites. *J. Electrochem. Soc.* **2005**, *152* (3), A607. https://doi.org/10.1149/1.1860492.

(43) Vink, P.; Bots, T. L. IN ORGANIC Formulation Parameters Influencing Self-Stratification of Coatings. **1996**, *28*, 173–181. https://doi.org/10.1016/0300-9440(95)00595-1.

(44) Ulaeto, S. B.; Rajan, R.; Pancrecious, J. K.; Rajan, T. P. D.; Pai, B. C. Developments in Smart Anticorrosive Coatings with Multifunctional Characteristics. *Prog. Org. Coatings* **2017**, *111* (December 2016), 294–314. https://doi.org/10.1016/j.porgcoat.2017.06.013.

(45) Such, G. K.; Quinn, J. F.; Quinn, A.; Tjipto, E.; Caruso, F. Assembly of Ultrathin Polymer Multilayer Films by Click Chemistry. *J. Am. Chem. Soc.* **2006**, *128* (29), 9318–9319. https://doi.org/10.1021/ja063043+.

(46) Serizawa, T.; Nanameki, K.; Yamamoto, K.; Akashi, M. Thermoresponsive Ultrathin Hydrogels Prepared by Sequential Chemical Reactions. *Macromolecules* **2002**, *35* (6), 2184–2189. https://doi.org/10.1021/ma011465s.

(47) Gruner, G. Carbon Nanotube Films for Transparent and Plastic Electronics. *J. Mater. Chem.* **2006**, *16* (35), 3533. https://doi.org/10.1039/b603821m.

(48) Funke, W. Preparation and Properties of Paint Films with Special Morphological Structure. *J. Oil Colour Chem. Assoc.* **1976**, No. 59, 398–403.

(49) Verkholantsev, V. Heterophase and Self-Stratifying Polymer Coatings. *Prog. Org. Coatings* **1995**, *26* (1), 31–52. https://doi.org/10.1016/0300-9440(95)00552-8.

(50) Bertrand, P.; Jonas, A.; Laschewsky, A.; Legras, R. Ultrathin Polymer Coatings by Complexation of Polyelectrolytes at Interfaces: Suitable Materials, Structure and Properties. *Macromol. Rapid Commun.* **2000**, *21* (7), 319–348. https://doi.org/10.1002/(SICI)1521-3927(20000401)21:7<319::AID-MARC319>3.0.CO;2-7.

(51) Verkholantsev, V. V. Self-Stratifying Coatings for Industrial Applications. *Pigment Resin Technol.* **2003**, *32* (5), 300–306. https://doi.org/10.1108/03699420310497445.

(52) Han, S.; Yu, X.; Shi, W.; Zhuang, X.; Yu, J. Solvent-Dependent Electrical Properties Improvement of Organic Field-Effect Transistor Based on Disordered Conjugated Polymer/Insulator Blends. *Org. Electron. physics, Mater. Appl.* **2015**, *27*, 160–186. https://doi.org/10.1016/j.orgel.2015.09.003.

(53) Carr, C. Theoretical Aspects of Self-Stratification. *Prog. Org. coatings* **1996**, *28*, 161–171. https://doi.org/10.1016/0300-9440(95)00594-3.
(54) Hejda, F.; Solar, P.; Kousal, J.; Sola˘, P.; Kousal, J. Surface Free Energy Determination by Contact Angle Measurements – A Comparison of Various Approaches. *WDS'10 Proc. Contrib. Pap.* **1969**, No. 3, 25–30.
(55) Schaefer, C.; Michels, J. J.; Van Der Schoot, P. Dynamic Surface Enrichment in Drying Thin-Film Binary Polymer Solutions. *Macromolecules* **2017**, *50* (15), 5914–5919. https://doi.org/10.1021/acs.macromol.7b01224.
(56) Chen, L. M.; Hong, Z.; Li, G.; Yang, Y. Recent Progress in Polymer Solar Cells: Manipulation of Polymer: Fullerene Morphology and the Formation of Efficient Inverted Polymer Solar Cells. *Adv. Mater.* **2009**, *21* (14–15), 1434–1449. https://doi.org/10.1002/adma.200802854.
(57) Mokarian-Tabari, P.; Geoghegan, M.; Howse, J. R.; Heriot, S. Y.; Thompson, R. L.; Jones, R. a L. Quantitative Evaluation of Evaporation Rate during Spin-Coating of Polymer Blend Films: Control of Film Structure through Defined-Atmosphere Solvent-Casting. *Eur. Phys. J. E* **2010**, *33* (4), 283–289. https://doi.org/10.1140/epje/i2010-10670-7.
(58) Heriot, S. Y.; Jones, R. a L. Supporting Material: An Interfacial Instability in a Transient Wetting Layer Leads to Lateral Phase Separation in Thin Spin-Cast Polymer-Blend Films. *Nat. Mater.* **2005**, *4* (10), 782–786. https://doi.org/10.1038/nmat1476.
(59) Brigham, N.; Nardi, C.; Carandang, A.; Allen, K.; Van Horn, R. M. Manipulation of Crystallization Sequence in PEO-b-PCL Films Using Solvent Interactions. *Macromolecules* **2017**, *50* (22), 8996–9007. https://doi.org/10.1021/acs.macromol.7b02004.
(60) Akutsu, F.; Inoki, M.; Daicho, N.; Kasashima, Y.; Shiraishi, N.; Marushima, K. Curing Behavior and Properties of Epoxy Resins Cured with the Diamine Having the Quinoxaline or Triazine Structure.Pdf. *J. Polym. Sci.* **1998**, *69*, 1737–1741. https://doi.org/10.1097/PPO.0b013e3181a27018.
(61) Jin, F.-L.; Li, X.; Park, S.-J. Synthesis and Application of Epoxy Resins: A Review. *J. Ind. Eng. Chem.* **2015**, *29*, 1–11.
(62) Baghdachi, J.; Perez, H.; Talapatcharoenkit, P.; Wang, B. Design and Development of Self-Stratifying Systems as Sustainable Coatings. *Prog. Org. Coatings* **2015**, *78*, 464–473. https://doi.org/10.1016/j.porgcoat.2014.06.017.
(63) Higgins, A. M.; Martin, S. J.; Thompson, R. L.; Chappell, J.; Voigt, M.; Lidzey, D. G.; Jones, R. A. L.; Geoghegan, M. Surface Segregation and Self-Stratification in Blends of Spin-Cast Polyfluorene Derivatives. *J. Phys. Condens. Matter* **2005**, *17* (8), 1319–1328. https://doi.org/10.1088/0953-8984/17/8/010.
(64) Scaccabarozzi, A. D.; Stingelin, N. Semiconducting:Insulating Polymer Blends for Optoelectronic Applications-a Review of Recent Advances. *J. Name* **2013**, *00*, 1–3. https://doi.org/10.1039/x0xx00000x.
(65) Wang, X. X.; Lee, W. H.; Zhang, G.; Wang, X. X.; Kang, B.; Lu, H.; Qiu, L.; Cho,

K. Self-Stratified Semiconductor/Dielectric Polymer Blends: Vertical Phase Separation for Facile Fabrication of Organic Transistors. *J. Mater. Chem. C* **2013**, *1* (25), 3989. https://doi.org/10.1039/c3tc30257a.

(66) Yan, Y.; Liu, X.; Wang, T. Conjugated-Polymer Blends for Organic Photovoltaics: Rational Control of Vertical Stratification for High Performance. *Adv. Mater.* **2017**, No. February. https://doi.org/10.1002/adma.201601674.

(67) Dunne, L. Smart Clothing in Practice: Key Design Barriers to Commercialization. *Fash. Pract. J. Des. Creat. Process Fash. Ind.* **2010**, *2* (1), 41–66. https://doi.org/10.2752/175693810X12640026716393.

(68) Budkowski, a.; Bernasik, a.; Cyganik, P.; Raczkowska, J.; Penc, B.; Bergues, B.; Kowalski, K.; Rysz, J.; Janik, J. Substrate-Determined Shape of Free Surface Profiles in Spin-Cast Polymer Blend Films. *Macromolecules* **2003**, *36* (11), 4060–4067. https://doi.org/10.1021/ma0208943.

(69) Im, M.; Im, H.; Lee, J. H.; Yoon, J. B.; Choi, Y. K. A Robust Superhydrophobic and Superoleophobic Surface with Inverse-Trapezoidal Microstructures on a Large Transparent Flexible Substrate. *Soft Matter* **2010**, *6* (7), 1401–1404. https://doi.org/10.1002/jbm.b.31934.

(70) Chang, J.; Zhang, X.; Ge, T.; Zhou, J. Fully Printed Electronics on Flexible Substrates: High Gain Amplifiers and DAC. *Org. Electron. physics, Mater. Appl.* **2014**, *15* (3), 701–710. https://doi.org/10.1016/j.orgel.2013.12.027.

(71) Carta, R.; Jourand, P.; Hermans, B.; Thoné, J.; Brosteaux, D.; Vervust, T.; Bossuyt, F.; Axisa, F.; Vanfleteren, J.; Puers, R. Design and Implementation of Advanced Systems in a Flexible-Stretchable Technology for Biomedical Applications. *Sensors Actuators, A Phys.* **2009**, *156* (1), 79–87. https://doi.org/10.1016/j.sna.2009.03.012.

(72) Xue, B.; Vaughan, B.; Poh, C. H.; Burke, K. B.; Thomsen, L.; Stapleton, A.; Zhou, X.; Bryant, G. W.; Belcher, W.; Dastoor, P. C. Vertical Stratification and Interfacial Structure in P3HT:PCBM Organic Solar Cells. *J. Phys. Chem. C* **2010**, *114* (37), 15797–15805. https://doi.org/10.1021/jp104695j.

(73) Wang, T.; Scarratt, N. W.; Yi, H.; Coleman, I. F.; Zhang, Y.; Grant, R. T.; Yao, J.; Skoda, M. W. A.; Dunbar, A. D. F.; Jones, R. A. L.; et al. Vertical Stratification and Its Impact on Device Performance in a Polycarbazole Based Copolymer Solar Cells. *J. Mater. Chem. C* **2015**, *3* (16), 4007–4015. https://doi.org/10.1039/C4TC02884H.

(74) Qiu, L.; Lim, J. A.; Wang, X.; Lee, W. H.; Hwang, M.; Cho, K. Versatile Use of Vertical-Phase-Separation-Induced Bilayer Structures in Organic Thin-Film Transistors. *Adv. Mater.* **2008**, *20* (6), 1141–1145. https://doi.org/10.1002/adma.200702505.

(75) Cumpson, P. J. *Angle-Resolved XPS and AES: Depth-Resolution Limits and a General Comparison of Properties of Depth-Profile Reconstruction Methods*; 1994.

(76) Liu, C.; Li, Y.; Lee, M. V; Kumatani, A.; Tsukagoshi, K. Self-Assembly of Semiconductor/Insulator Interfaces in One-Step Spin-Coating: A Versatile Approach for Organic Field-Effect Transistors. *Phys. Chem. Chem. Phys.* **2013**, *15* (21), 7917–7933. https://doi.org/10.1039/c3cp44715d.

(77) Grunwald, E.; Nuster, R.; Hammer, R.; Abmann, H.; Paltauf, G.; Brunner, R. Characterization of Polyimid-Multi-Layer Thin Films Combining Laser Ultrasonic Measurements and Numerical Evaluations. *2016 17th Int. Conf. Therm. Mech. Multi-Physics Simul. Exp. Microelectron. Microsystems, EuroSimE 2016* **2016**, No. Mcl, 1–5. https://doi.org/10.1109/EuroSimE.2016.7463353.

(78) Ahmadi Lakalayeh, G.; Rahvar, M.; Haririan, E.; Karimi, R.; Ghanbari, H. Comparative Study of Different Polymeric Coatings for the Next-Generation Magnesium-Based Biodegradable Stents. *Artif. Cells, Nanomedicine Biotechnol.* **2017**, *46*, 1–10. https://doi.org/10.1080/21691401.2017.1369424.

(79) Cristea, M. V.; Riedl, B.; Blanchet, P. Effect of Addition of Nanosized UV Absorbers on the Physico-Mechanical and Thermal Properties of an Exterior Waterborne Stain for Wood. *Prog. Org. Coatings* **2011**, *72* (4), 755–762. https://doi.org/10.1016/j.porgcoat.2011.08.007.

(80) Hennessy, M. G.; Burlakov, V. M.; Münch, A.; Wagner, B.; Goriely, A. Propagating Topological Transformations in Thin Immiscible Bilayer Films. *Epl* **2014**, *105* (6). https://doi.org/10.1209/0295-5075/105/66001.

(81) Kline, R. J.; McGehee, M. D.; Kadnikova, E. N.; Liu, J.; Fréchet, J. M. J.; Toney, M. F. Dependence of Regioregular Poly(3-Hexylthiophene) Film Morphology and Field-Effect Mobility on Molecular Weight. *Macromolecules* **2005**, *38* (8), 3312–3319. https://doi.org/10.1021/ma047415f.

(82) Paterson, A. F.; Lin, Y.-H.; Mottram, A. D.; Fei, Z.; Niazi, M. R.; Kirmani, A. R.; Amassian, A.; Solomeshch, O.; Tessler, N.; Heeney, M.; et al. The Impact of Molecular P-Doping on Charge Transport in High-Mobility Small-Molecule/Polymer Blend Organic Transistors. *Adv. Electron. Mater.* **2017**, *1700464*, 1700464. https://doi.org/10.1002/aelm.201700464.

(83) Guo, P.; Luo, G.; Su, Q.; Li, J.; Zhang, P.; Tong, J.; Yang, C.; Xia, Y.; Wu, H. Boosting Up Performance of Inverted Photovoltaic Cells from Bis(Alkylthien-2-Yl)Dithieno[2,3-d:2′,3′-D′]Benzo[1,2-b:4′,5′-B′]Di Thiophene-Based Copolymers by Advantageous Vertical Phase Separation. *ACS Appl. Mater. Interfaces* **2017**, *9* (12), 10937–10945. https://doi.org/10.1021/acsami.6b15436.

(84) Alcazar, D.; Wang, F.; Swager, T. M.; Thomas, E. L. Gel Processing for Highly Oriented Conjugated Polymer Films Gel Processing for Highly Oriented Conjugated Polymer Films. **2008**, 9863–9868. https://doi.org/10.1021/ma8020739.

(85) Barbero, D. R.; Steiner, U. Nonequilibrium Polymer Rheology in Spin-Cast Films. *Phys. Rev. Lett.* **2009**, *102* (24), 1–4. https://doi.org/10.1103/PhysRevLett.102.248303.

(86) Heriot, S. Y.; Jones, R. a L. An Interfacial Instability in a Transient Wetting Layer Leads to Lateral Phase Separation in Thin Spin-Cast Polymer-Blend Films. *Nat. Mater.* **2005**, *4* (10), 782–786. https://doi.org/10.1038/nmat1476.

(87) Xu, Z.; Chen, L. M.; Yang, G.; Huang, C. H.; Hou, J.; Wu, Y.; Li, G.; Hsu, C. S.; Yang, Y. Vertical Phase Separation in Poly(3-Hexylthiophene): Fullerene Derivative Blends and Its Advantage for Inverted Structure Solar Cells. *Adv. Funct.*

Mater. **2009**, *19* (8), 1227–1234. https://doi.org/10.1002/adfm.200801286.
(88) Ge, F.; Liu, Z.; Lee, S. B.; Wang, X.; Zhang, G.; Lu, H.; Cho, K.; Qiu, L. Bar-Coated Ultrathin Semiconductor from Polymer Blend for One-Step Organic Field-Effect Transistors. *ACS Appl. Mater. Interfaces* **2018**, *10*, 21510–21517. https://doi.org/10.1021/acsami.8b07118.
(89) Zhang, L.; Yang, D.; Wang, Y.; Wang, H.; Song, T.; Fu, C.; Yang, S.; Wei, J.; Liu, R.; Zou, B. Performance Enhancement of FET-Based Photodetector by Blending P3HT With PMMA. *IEEE Photonics Technol. Lett.* **2015**, *27* (14), 1535–1538. https://doi.org/10.1109/LPT.2015.2427796.
(90) Wu, M. C.; Liao, H. C.; Chou, Y.; Hsu, C. P.; Yen, W. C.; Chuang, C. M.; Lin, Y. Y.; Chen, C. W.; Chen, Y. F.; Su, W. F. Manipulation of Nanoscale Phase Separation and Optical Properties of P3HT/PMMA Polymer Blends for Photoluminescent Electron Beam Resist. *J. Phys. Chem. B* **2010**, *114* (32), 10277–10284. https://doi.org/10.1021/jp1009059.
(91) Gburek, B.; Wagner, V. Influence of the Semiconductor Thickness on the Charge Carrier Mobility in P3HT Organic Field-Effect Transistors in Top-Gate Architecture on Flexible Substrates. *Org. Electron. physics, Mater. Appl.* **2010**, *11* (5), 814–819. https://doi.org/10.1016/j.orgel.2010.01.023.
(92) Sirringhaus, H. Device Physics of Solution-Processed Organic Field-Effect Transistors. *Adv. Mater.* **2005**, *17* (20), 2411–2425. https://doi.org/10.1002/adma.200501152.
(93) Herlogsson, L.; Noh, Y. Y.; Zhao, N.; Crispin, X.; Sirringhaus, H.; Berggren, M. Downscaling of Organic Field-Effect Transistors with a Polyelectrolyte Gate Insulator. *Adv. Mater.* **2008**, *20* (24), 4708–4713. https://doi.org/10.1002/adma.200801756.
(94) Kergoat, L.; Battaglini, N.; Miozzo, L.; Piro, B.; Pham, M. C.; Yassar, A.; Horowitz, G. Use of Poly(3-Hexylthiophene)/Poly(Methyl Methacrylate) (P3HT/PMMA) Blends to Improve the Performance of Water-Gated Organic Field-Effect Transistors. *Org. Electron. physics, Mater. Appl.* **2011**, *12* (7), 1253–1257. https://doi.org/10.1016/j.orgel.2011.04.006.
(95) Toolan, D. T. W.; Isakova, A.; Hodgkinson, R.; Reeves-Mclaren, N.; Hammond, O. S.; Edler, K. J.; Briscoe, W. H.; Arnold, T.; Gough, T.; Topham, P. D.; et al. Insights into the Influence of Solvent Polarity on the Crystallization of Poly(Ethylene Oxide) Spin-Coated Thin Films via in Situ Grazing Incidence Wide-Angle X-Ray Scattering. *Macromolecules* **2016**, *49* (12), 4579–4586. https://doi.org/10.1021/acs.macromol.6b00312.
(96) Ohmori, M.; Nakatani, M.; Kajii, H.; Miyamoto, A.; Yoneya, M.; Fujii, A.; Ozaki, M. Fabrication of Field-Effect Transistor Utilizing Oriented Thin Film of Octahexyl-Substituted Phthalocyanine and Its Electrical Anisotropy Based on Columnar Structure. *Jpn. J. Appl. Phys.* **2018**, *57* (3). https://doi.org/10.7567/JJAP.57.03EH10.
(97) Zhao, K.; Wodo, O.; Ren, D.; Khan, H. U.; Niazi, M. R.; Hu, H.; Abdelsamie, M.;

Li, R.; Li, E. Q.; Yu, L.; et al. Vertical Phase Separation in Small Molecule:Polymer Blend Organic Thin Film Transistors Can Be Dynamically Controlled. *Adv. Funct. Mater.* **2016**, *26* (11), 1737–1746. https://doi.org/10.1002/adfm.201503943.

(98) Emerson, J. A.; Garabedian, N. T.; Moore, A. C.; Burris, D. L.; Furst, E. M.; Epps, T. H. Unexpected Tribological Synergy in Polymer Blend Coatings: Leveraging Phase Separation to Isolate Domain Size Effects and Reduce Friction. *ACS Appl. Mater. Interfaces* **2017**, *9* (39), 34480–34488. https://doi.org/10.1021/acsami.7b10170.

(99) Kienzle, P. A.; O'Donovan, K. V.; Ankner, J. F.; Berk, N. F.; Majkrzak, C. F. http://www.ncnr.nist.gov/reflpak http://www.ncnr.nist.gov/reflpak.

(100) Nelson, A. Co-Refinement of Multiple-Contrast Neutron/X-Ray Reflectivity Data Using MOTOFIT. *J. Appl. Crystallogr.* **2006**, *39* (2), 273–276. https://doi.org/10.1107/S0021889806005073.

(101) Balzarotti, R.; Cristiani, C.; Francis, L. F. Spin Coating Deposition on Complex Geometry Substrates: Influence of Operative Parameters. *Surf. Coatings Technol.* **2017**, *330* (August), 1–9. https://doi.org/10.1016/j.surfcoat.2017.09.077.

(102) Owens, D. K.; Wendt, R. C. Estimation of the Surface Free Energy of Polymers. *J. Appl. Polym. Sci.* **1969**, *13* (8), 1741–1747. https://doi.org/10.1002/app.1969.070130815.

(103) Campoy-Quiles, M.; Ferenczi, T.; Agostinelli, T.; Etchegoin, P. G.; Kim, Y.; Anthopoulos, T. D.; Stavrinou, P. N.; Bradley, D. D. C.; Nelson, J. Morphology Evolution via Self-Organization and Lateral and Vertical Diffusion in Polymer:Fullerene Solar Cell Blends. *Nat. Mater.* **2008**, *7* (2), 158–164. https://doi.org/10.1038/nmat2102.

(104) Rubinstein, M.; Colby, R. H. *Polymer Physics*; Oxford University Press, 2003.

(105) Hiemenz, P. C.; Lodge, T. P. *Polymer Chemistry*, Second Edi.; Taylor & Francis Group, LLC: Boca Raton, FL, 2007.

(106) Emerson, J. A.; Toolan, D. T. W.; Howse, J. R.; Furst, E. M.; Epps, T. H. Determination of Solvent − Polymer and Polymer − Polymer Flory − Huggins Interaction Parameters for Poly(3-Hexylthiophene) via Solvent Vapor Swelling. *Macrolecules* **2013**.

(107) Lindvig, T.; Michelsen, M. L.; Kontogeorgis, G. M. A Flory-Huggins Model Based on the Hansen Solubility Parameters. *Fluid Phase Equilib.* **2002**, *203* (1–2), 247–260. https://doi.org/10.1016/S0378-3812(02)00184-X.

(108) Zhang, R.; Lee, B.; Stafford, C. M.; Douglas, J. F.; Dobrynin, A. V.; Bockstaller, M. R.; Karim, A. Entropy-Driven Segregation of Polymer-Grafted Nanoparticles under Confinement. *Proc. Natl. Acad. Sci.* **2017**, *114* (10), 2462–2467. https://doi.org/10.1073/pnas.1613828114.

(109) Zhu, G.; Huang, Z.; Xu, Z.; Yan, L. T. Tailoring Interfacial Nanoparticle Organization through Entropy. *Acc. Chem. Res.* **2018**, *51* (4), 900–909. https://doi.org/10.1021/acs.accounts.8b00001.

(110) Hall, D. B.; Underhill, P.; Torkelson, J. M. Spin Coating of Thin and Ultrathin

Polymer Films. *Polym. Eng. Sci.* **1998**, *38* (12), 2039–2045. https://doi.org/10.1002/pen.10373.
(111) Meyerhofer, D. Characteristics of Resist Films Produced by Spinning. *J. Appl. Phys.* **1978**, *49* (7), 3993–3997. https://doi.org/10.1063/1.325357.
(112) Lai, J. H. An Investigation of Spin Coating of Electron Resists. *Polym. Eng. Sci.* **1979**, *19* (15), 1117–1121. https://doi.org/10.1002/pen.760191509.
(113) Dunbar, A. D. F.; Mokarian-Tabari, P.; Parnell, A. J.; Martin, S. J.; Skoda, M. W. A.; Jones, R. A. L. A Solution Concentration Dependent Transition from Self-Stratification to Lateral Phase Separation in Spin-Cast PS:D-PMMA Thin Films. *Eur. Phys. J. E* **2010**, *31* (4), 369–375. https://doi.org/10.1140/epje/i2010-10592-4.
(114) Chiarelli, P. A.; Johal, M. S.; Holmes, D. J.; Casson, J. L.; Robinson, J. M.; Wang, H. L. Polyelectrolyte Spin-Assembly. *Langmuir* **2002**, *18* (1), 168–173. https://doi.org/10.1021/la011333s.
(115) A., C. P.; S., J. M.; L., C. J.; B., R. J.; M., R. J.; H.-L., W. Controlled Fabrication of Polyelectrolyte Multilayer Thin Films Using Spin-Assembly. *Adv. Mater.* **2001**, *13* (15), 1167–1171. https://doi.org/10.1002/1521-4095(200108)13:15<1167::AID-ADMA1167>3.0.CO;2-A.
(116) Stange, T. G.; Mathew, R.; Evans, D. F.; Hendrickson, W. A. Scanning Tunneling Microscopy and Atomic Force Microscopy Characterization of Polystyrene Spin-Coated onto Silicon Surfaces. *Langmuir* **1992**, *8* (3), 920–926. https://doi.org/10.1021/la00039a030.
(117) Shi, Y.; Liu, J.; Yang, Y.; Shi, Y.; Liu, J.; Yang, Y. Device Performance and Polymer Morphology in Polymer Light Emitting Diodes : The Control of Thin Film Morphology and Device Quantum Efficiency Device Performance and Polymer Morphology in Polymer Light Emitting Diodes : The Control of Thin Film Morphology. *J. Appl. Phys.* **2000**, *87* (9), 4254–4263. https://doi.org/10.1063/1.373062.
(118) Morgan, B.; Dadmun, M. D. Illumination of Conjugated Polymer in Solution Alters Its Conformation and Thermodynamics. *Macromolecules* **2016**, *49* (9), 3490–3496. https://doi.org/10.1021/acs.macromol.6b00527.
(119) Morgan, B.; Dadmun, M. D. Illumination Alters the Structure of Gels Formed from the Model Optoelectronic Material P3HT. *Polymer (Guildf).* **2017**, *108*, 313–321. https://doi.org/10.1016/j.polymer.2016.11.056.
(120) Morgan, B.; Dadmun, M. D. The Importance of Solvent Quality on the Modification of Conjugated Polymer Conformation and Thermodynamics with Illumination. *Soft Matter* **2017**, *13* (15), 2773–2780. https://doi.org/10.1039/C6SM02631A.
(121) Han, S.; Zhuang, X.; Wei, S.; Yang, X.; Li, L.; Yu, J. Poly (3-Hexylthiophene)/ Polystyrene (P3HT / PS) Blends Based Organic Field-Effect Transistor Ammonia Gas ... *Sensors Actuators B* **2015**, *225* (November). https://doi.org/10.1016/j.snb.2015.11.005.
(122) Cho, S.; Coates, N.; Moon, J. S.; Park, S. H.; Roy, A.; Beaupre, S.; Moses, D.; Leclerc, M.; Lee, K.; Heeger, A. J. Bulk Heterojunction Solar Cells with Internal

Quantum Efficiency Approaching 100. *Nat. Photonics* **2009**, *3* (5), 297–302. https://doi.org/10.1038/nphoton.2009.69.
(123) Björström, C. M.; Bernasik, A.; Rysz, J.; Budkowski, A.; Nilsson, S.; Svensson, M.; Andersson, M. R.; Magnusson, K. O.; Moons, E. Multilayer Formation in Spin-Coated Thin Films of Low-Bandgap Polyfluorene:PCBM Blends. *J. Phys. Condens. Matter* **2005**, *17* (50), L529–L534. https://doi.org/10.1088/0953-8984/17/50/L01.
(124) Morgan, B.; Dadmun, M. D. The Effect of Illumination on the Depth Profile of Thermally Annealed MEH-PPV / DPS Blends. **2017**, 1142–1149. https://doi.org/10.1002/polb.24354.
(125) Wodo, O. How Do Evaporating Thin Films Evolve ? Unravelling Phase-Separation Mechanisms during Solvent-Based Fabrication of Polymer Blends. **2014**.
(126) Kline, R. J.; Mcgehee, M. D.; Toney, M. F.; Synchrotron, S.; Park, M. Highly Oriented Crystals at the Buried Interface in Polythiophene Thin-Film Transistors. *Nat. Mater.* **2006**, *5* (March). https://doi.org/10.1038/nmat1590.
(127) Rinehart, S. J.; Yuan, G.; Dadmun, M. D. Elucidating the Kinetic and Thermodynamic Driving Forces in Polymer Blend Film Self-Strati Fi Cation. **2018**. https://doi.org/10.1021/acs.macromol.8b01397.
(128) Braun, S.; Salaneck, W. R.; Fahlman, M. Energy-Level Alignment at Organic/Metal and Organic/Organic Interfaces. *Adv. Mater.* **2009**, *21* (14–15), 1450–1472. https://doi.org/10.1002/adma.200802893.
(129) Kwak, D.; Choi, H. H.; Kang, B.; Kim, D. H.; Lee, W. H. Tailoring Morphology and Structure of Inkjet-Printed Liquid-Crystalline Semiconductor / Insulating Polymer Blends for High-Stability Organic Transistors. **2016**, 3003–3011. https://doi.org/10.1002/adfm.201504786.
(130) Nicho, M. E.; García-escobar, C. H.; Arenas, M. C.; Altuzar-coello, P.; Cruz-silva, R. Influence of P3HT Concentration on Morphological , Optical and Electrical Properties of P3HT / PS and P3HT / PMMA Binary Blends. *Mater. Sci. Eng. B* **2011**, *176* (17), 1393–1400. https://doi.org/10.1016/j.mseb.2011.05.008.
(131) Lu, G.; Blakesley, J.; Himmelberger, S.; Pingel, P.; Frisch, J.; Lieberwirth, I.; Salzmann, I.; Oehzelt, M.; Di Pietro, R.; Salleo, A.; et al. Moderate Doping Leads to High Performance of Semiconductor/Insulator Polymer Blend Transistors. *Nat. Commun.* **2013**, *4*, 1588. https://doi.org/10.1038/ncomms2587.
(132) Jukes, P. C.; Heriot, S. Y.; Sharp, J. S.; Jones, R. a. L. Time-Resolved Light Scattering Studies of Phase Separation in Thin Film Semiconducting Polymer Blends during Spin-Coating. *Macromolecules* **2005**, *38* (6), 2030–2032. https://doi.org/10.1021/ma0477145.
(133) Chou, K. W.; Yan, B.; Li, R.; Li, E. Q.; Zhao, K.; Anjum, D. H.; Alvarez, S.; Gassaway, R.; Biocca, A.; Thoroddsen, S. T. Solar Cells : Spin-Cast Bulk Heterojunction Solar Cells : A Dynamical Investigation (Adv. Spin-Cast Bulk Heterojunction Solar Cells : A Dynamical Investigation. **2017**, No. April 2013. https://doi.org/10.1002/adma.201203440.
(134) Zhou, N.; Lin, H.; Lou, S. J.; Yu, X.; Guo, P.; Manley, E. F.; Loser, S.; Hartnett, P.;

Huang, H.; Wasielewski, M. R.; et al. Morphology-Performance Relationships in High-Effi Ciency All-Polymer Solar Cells. **2014**. https://doi.org/10.1002/aenm.201300785.

(135) Yoon, M. H.; Kim, C.; Facchetti, A.; Marks, T. J. Gate Dielectric Chemical Structure-Organic Field-Effect Transistor Performance Correlations for Electron, Hole, and Ambipolar Organic Semiconductors. *J. Am. Chem. Soc.* **2006**, *128* (39), 12851–12869. https://doi.org/10.1021/ja063290d.

(136) Fabiano, S.; Himmelberger, S.; Drees, M.; Chen, Z.; Altamimi, R. M.; Salleo, A.; Loi, M. A.; Facchetti, A. Charge Transport Orthogonality in All-Polymer Blend Transistors, Diodes, and Solar Cells. *Adv. Energy Mater.* **2014**, *4* (6), 1–7. https://doi.org/10.1002/aenm.201301409.

(137) MacHui, F.; Langner, S.; Zhu, X.; Abbott, S.; Brabec, C. J. Determination of the P3HT:PCBM Solubility Parameters via a Binary Solvent Gradient Method: Impact of Solubility on the Photovoltaic Performance. *Sol. Energy Mater. Sol. Cells* **2012**, *100*, 138–146. https://doi.org/10.1016/j.solmat.2012.01.005.

(138) Bi, C.; Wang, Q.; Shao, Y.; Yuan, Y.; Xiao, Z.; Huang, J. Non-Wetting Surface-Driven High-Aspect-Ratio Crystalline Grain Growth for Efficient Hybrid Perovskite Solar Cells. *Nat. Commun.* **2015**, *6*, 1–7. https://doi.org/10.1038/ncomms8747.

(139) Liu, J.; Guo, T.-F.; Yang, Y. Effects of Thermal Annealing on the Performance of Polymer Light Emitting Diodes. *J. Appl. Phys.* **2002**, *91* (3), 1595–1600. https://doi.org/10.1063/1.1427435.

(140) Zhang, R.; Li, B.; Iovu, M. C.; Jeffries-el, M.; Sauve, G.; Cooper, J.; Jia, S.; Tristram-Nagle, S.; Smilgies, D. M.; Lambeth, D. N.; et al. Nanostructure Dependence of Field-Effect Mobility in Regioregular Poly (3-Hexylthiophene) Thin Film Field Effect Transistors Nanostructure Dependence of Field-Effect Mobility in Regioregular. *J. Am. Chem. Soc.* **2006**, *128* (11), 3480–3481. https://doi.org/10.1021/ja055192i.

(141) Cao, Y.; Treacy, G. M.; Smith, P.; Heeger, A. J. Solution-Cast Films of Polyaniline: Optical-Quality Transparent Electrodes. *Appl. Phys. Lett.* **1992**, *60* (22), 2711–2713. https://doi.org/10.1063/1.106852.

(142) Debye, P.; Anderson, H. R.; Brumberger, H. Scattering by an Inhomogeneous Solid. II. the Correlation Function and Its Application. *J. Appl. Phys.* **1957**, *28* (6), 679–683. https://doi.org/10.1063/1.1722830.

(143) Kline, S. R. Reduction and Analysis of SANS and USANS Data Using IGOR Pro. *J. Appl. Crystallogr.* **2006**, *39* (6), 895–900. https://doi.org/10.1107/S0021889806035059.

(144) Lee, C. S.; Yin, W.; Holt, A. P.; Sangoro, J. R.; Sokolov, A. P.; Dadmun, M. D. Rapid and Facile Formation of P3HT Organogels via Spin Coating: Tuning Functional Properties of Organic Electronic Thin Films. *Adv. Funct. Mater.* **2015**, *25* (36), 5848–5857. https://doi.org/10.1002/adfm.201501707.

(145) Bao, Z.; Dodabalapur, A.; Lovinger, A. J. Soluble and Processable Regioregular Poly(3-Hexylthiophene) for Thin Film Field-Effect Transistor Applications with

High Mobility. *Appl. Phys. Lett.* **1996**, *69* (26), 4108–4110. https://doi.org/10.1063/1.117834.
(146) Chang, J. F.; Sun, B.; Breiby, D. W.; Nielsen, M. M.; Sölling, T. I.; Giles, M.; McCulloch, I.; Sirringhaus, H. Enhanced Mobility of Poly(3-Hexylthiophene) Transistors by Spin-Coating from High-Boiling-Point Solvents. *Chem. Mater.* **2004**, *16* (23), 4772–4776. https://doi.org/10.1021/cm049617w.
(147) Wu, C. J.; Huang, C. J.; Jiang, S.; Sheng, Y. J.; Tsao, H. K. Superhydrophilicity and Spontaneous Spreading on Zwitterionic Surfaces: Carboxybetaine and Sulfobetaine. *RSC Adv.* **2016**, *6* (30), 24827–24834. https://doi.org/10.1039/c6ra01825d.
(148) Pan, Y.; Liu, X.; Hao, X.; Starý, Z.; Schubert, D. W. Enhancing the Electrical Conductivity of Carbon Black-Filled Immiscible Polymer Blends by Tuning the Morphology. *Eur. Polym. J.* **2016**, *78*, 106–115. https://doi.org/10.1016/j.eurpolymj.2016.03.019.
(149) Choi, J.; Rubner, M. F. Influence of the Degree of Ionization on Weak Polyelectrolyte Multilayer Assembly. *Macromolecules* **2005**, *38* (1), 116–124. https://doi.org/10.1021/ma048596o.
(150) Wang, J.; Liang, M.; Fang, Y.; Qiu, T.; Zhang, J.; Zhi, L. Rod-Coating: Towards Large-Area Fabrication of Uniform Reduced Graphene Oxide Films for Flexible Touch Screens. *Adv. Mater.* **2012**, *24* (21), 2874–2878. https://doi.org/10.1002/adma.201200055.
(151) Miller, M. J.; Wang, J. Multilayer ITO/VO2/TiO2 Thin Films for Control of Solar and Thermal Spectra. *Sol. Energy Mater. Sol. Cells* **2016**, *154*, 88–93. https://doi.org/10.1016/j.solmat.2016.04.044.
(152) Granqvist, C. G.; Hultaker, A. Transparent and Conducting ITO Films: New Developments and Applications. *Thin Solid Films* **2002**, *411* (1), 1–5. https://doi.org/10.1016/S0040-6090(02)00163-3.
(153) Lin, Y. C.; Li, J. Y.; Yen, W. T. Low Temperature ITO Thin Film Deposition on PES Substrate Using Pulse Magnetron Sputtering. *Appl. Surf. Sci.* **2008**, *254* (11), 3262–3268. https://doi.org/10.1016/j.apsusc.2007.11.006.
(154) Lee, B. H.; Kim, I. G.; Cho, S. W.; Lee, S.-H. Effect of Process Parameters on the Characteristics of Indium Tin Oxide Thin Film for Flat Panel Display Application. *Thin Solid Films* **1997**, *302*, 25–30. https://doi.org/DOI: 10.1016/S0040-6090(96)09581-8.
(155) Ishii K Ito, E Seki, K, H. S. Energy Level Alignment and Interfacial Electronic Structures at Organic Metal and Organic Organic Interfaces. *Adv. Mater.* **1999**, *11* (8), +. https://doi.org/10.1002/(SICI)1521-4095(199906)11:8<605::AID-ADMA605>3.0.CO;2-Q.
(156) Jeong, S.; Ha, Y. G.; Moon, J.; Facchetti, A.; Marks, T. J. Role of Gallium Doping in Dramatically Lowering Amorphous-Oxide Processing Temperatures for Solution-Derived Indium Zinc Oxide Thin-Film Transistors. *Adv. Mater.* **2010**, *22* (12), 1346–1350. https://doi.org/10.1002/adma.200902450.
(157) Nomura, K.; Ohta, H.; Takagi, A.; Kamiya, T.; Hirano, M.; Hosono, H. Room-

Temperature Fabrication of Transparent Flexible Thin-Film Transistors Using Amorphous Oxide Semiconductors. *Nature* **2004**, *432* (7016), 488–492. https://doi.org/10.1038/nature03090.

(158) Chen, H.; Hsiao, Y.-C.; Hu, B.; Dadmun, M. D. Control of Morphology and Function of Low Band Gap Polymer – Bis-Fullerene Mixed Heterojunctions Vapor Annealing. *J. Mater. Chem. A* **2014**, 9883–9890. https://doi.org/10.1039/c4ta01436g.

(159) Kim, H.; Gilmore, C. M.; Piqué, A.; Horwitz, J. S.; Mattoussi, H.; Murata, H.; Kafafi, Z. H.; Chrisey, D. B. Electrical, Optical, and Structural Properties of Indium-Tin-Oxide Thin Films for Organic Light-Emitting Devices. *J. Appl. Phys.* **1999**, *86* (11), 6451–6461. https://doi.org/10.1063/1.371708.

(160) Tseng, K.-S.; Lo, Y.-L. Effects of Cumulative Ion Bombardment on ITO Films Deposited on PET and Si Substrates by DC Magnetron Sputtering. *Opt. Mater. Express* **2014**, *4* (4), 764. https://doi.org/10.1364/OME.4.000764.

(161) Ahn, M. H.; Cho, E. S.; Kwon, S. J. Characteristics of ITO-Resistive Touch Film Deposited on a PET Substrate by in-Line DC Magnetron Sputtering. *Vacuum* **2014**, *101*, 221–227. https://doi.org/10.1016/j.vacuum.2013.08.018.

(162) Kim, M.; Kim, H. S.; Ha, Y.; He, J.; Kanatzidis, M. G.; Facchetti, A.; Marks, T. J. High-Performance Solution-Processed Amorphous Zinc - Indium - Tin Oxide Thin-Film Transistors. **2010**, No. 4, 10352–10364.

(163) Kaneko, S.; Torii, H.; Soga, M.; Akiyama, K.; Iwaya, M.; Yoshimoto, M.; Amazawa, T. Epitaxial Indium Tin Oxide Film Deposited on Sapphire Substrate by Solid-Source Electron Cyclotron Resonance Plasma. *Jpn. J. Appl. Phys.* **2012**, *51* (1 PART 2). https://doi.org/10.1143/JJAP.51.01AC02.

(164) O'Dwyer, C.; Sotomayor Torres, C. M. Epitaxial Growth of an Antireflective, Conductive, Graded Index ITO Nanowire Layer. *Front. Phys.* **2013**, *1* (October), 1–8. https://doi.org/10.3389/fphy.2013.00018.

(165) Cui, H. N.; Teixeira, V.; Meng, L. J.; Martins, R.; Fortunato, E. Influence of Oxygen/Argon Pressure Ratio on the Morphology, Optical and Electrical Properties of ITO Thin Films Deposited at Room Temperature. *Vacuum* **2008**, *82* (12), 1507–1511. https://doi.org/10.1016/j.vacuum.2008.03.061.

(166) Sierros, K. A.; Morris, N. J.; Kukureka, S. N.; Cairns, D. R. Dry and Wet Sliding Wear of ITO-Coated PET Components Used in Flexible Optoelectronic Applications. *Wear* **2009**, *267* (1–4), 625–631. https://doi.org/10.1016/j.wear.2008.12.042.

(167) Hill, I. G.; Milliron, D.; Schwartz, J.; Kahn, A. Organic Semiconductor Interfaces: Electronic Structure and Transport Properties. *Appl. Surf. Sci.* **2000**, *166* (1–4), 354–362. https://doi.org/10.1016/S0169-4332(00)00449-9.

(168) Daillant, J.; Gibaud, A. *X-Ray and Neutron Reflectivity*; 2009. https://doi.org/10.1007/978-3-540-88588-7.

(169) Gilman, J. J. Relationship between Impact Yield Stress and Indentation Hardness. *J. Appl. Phys.* **1975**, *46* (4), 1435–1436. https://doi.org/10.1063/1.321790.

(170) Belger, A.; Reibold, M.; Paufler, P. Modulus and Hardness Change of Silicon and Sapphire Substrates by TiC / VC Multilayer Coatings. **2012**, *2012* (April), 185–194.
(171) Domnich, V.; Aratyn, Y.; Kriven, W. M.; Gogotsi, Y. Temperature Dependence of Silicon Hardness: Experimental Evidence of Phase Transformations. *Rev. Adv. Mater. Sci.* **2008**, *17* (1–2), 33–41.
(172) Haubruge, H. G.; Jonas, A. M.; Legras, R. Morphological Study of Melt-Crystallized Poly(Ethylene Terephthalate). A. Comparison of Transmission Electron Microscopy and Small-Angle X-Ray Scattering of Bulk Samples. *Macromolecules* **2004**, *37* (1), 126–134. https://doi.org/10.1021/ma0352678.
(173) Flores, A.; Pieruccini, M.; Stribeck, N.; Funari, S. S.; Bosch, E.; Baltá-Calleja, F. J. Structure Formation in Poly(Ethylene Terephthalate) upon Annealing as Revealed by Microindentation Hardness and X-Ray Scattering. *Polymer (Guildf).* **2005**, *46* (22), 9404–9410. https://doi.org/10.1016/j.polymer.2005.07.033.
(174) Abou-Kandil, A. I.; Flores, A.; Balta Calleja, F. J.; Windle, A. H. Microindentation Technique as a Tool for Investigating the Development of Order in PET under Uniaxial Stress. *J. Polym. Res.* **2008**, *15* (5), 373–379. https://doi.org/10.1007/s10965-008-9181-7.
(175) Cruz, C. S.; Calleja, F. J. B.; Zachmann, H. G.; Stribeck, N.; Asano, T. Relating Microhardness of Poly(Ethylene Terephthalate) to Microstructure. *J. Polym. Sci. Part B Polym. Phys.* **1991**, *29* (7), 819–824. https://doi.org/10.1002/polb.1991.090290706.
(176) Flores, A.; Ania, F.; Baltá-Calleja, F. J. From the Glassy State to Ordered Polymer Structures: A Microhardness Study. *Polymer (Guildf).* **2009**, *50* (3), 729–746. https://doi.org/10.1016/j.polymer.2008.11.037.
(177) Singh, M. A.; Groves, M. N. Depth Profiling of Polymer Films with Grazing-Incidence Small-Angle X-Ray Scattering. *Acta Crystallogr. Sect. A Found. Crystallogr.* **2009**, *65* (3), 190–201. https://doi.org/10.1107/S0108767309007508.
(178) Renaud, G.; Lazzari, R.; Leroy, F. Probing Surface and Interface Morphology with Grazing Incidence Small Angle X-Ray Scattering. *Surf. Sci. Rep.* **2009**, *64* (8), 255–380. https://doi.org/10.1016/j.surfrep.2009.07.002.
(179) Soltwisch, V.; Haase, A.; Wernecke, J.; Probst, J.; Schoengen, M.; Burger, S.; Krumrey, M.; Scholze, F. Correlated Diffuse X-Ray Scattering from Periodically Nanostructured Surfaces. *Phys. Rev. B* **2016**, *94* (3), 1–6. https://doi.org/10.1103/PhysRevB.94.035419.
(180) Babonneau, D.; Camelio, S.; Lantiat, D.; Simonot, L.; Michel, A. Waveguiding and Correlated Roughness Effects in Layered Nanocomposite Thin Films Studied by Grazing-Incidence Small-Angle x-Ray Scattering. *Phys. Rev. B - Condens. Matter Mater. Phys.* **2009**, *80* (15), 1–12. https://doi.org/10.1103/PhysRevB.80.155446.

VITA

Samantha Jae Rinehart was born May 17, 1991 in Ames, Iowa. She was raised in Marion, Iowa where she graduated from Marion High School in May 2009. Samantha attended Lewis University (Romeoville, IL) where she played collegiate basketball for the Flyers. Additionally, she conducted research in material chemistry for Dr. Jason J. Keleher and graduated with a Bachelor of Science in Chemistry and Biology in May 2014. The following August, Samantha began her graduate school career at the University of Tennessee-Knoxville specializing in Polymer Chemistry under advisement of Professor Mark D. Dadmun, Ph.D.